Chapter 5

Numerical Simulations of Volcanic Eruptions

Chapter Contents

Abstract

This chapter presents some simulations concerning the dynamics of crustal magma reservoirs during the course of volcanic eruptions. Despite its simplifications, the physical model proposed allows to simulate "any kind" of eruptive process. The chapter is organised as follows. Firstly, some previous considerations such as geometries or boundary and initial conditions for the different problems considered are discussed. Section 5.2 presents some simulations of withdrawal from closed magma chambers (eruptions driven by oversaturation of volatiles) considering both a constant and a variable volatile content. Section 5.3 shows examples concerning the withdrawal from open magma chambers (eruptions driven by injection of fresh magma) in both the chemically homogeneous and the chemically heterogeneous cases. Finally, section 5.4 presents a couple of examples of caldera-forming eruptions. The simulations of such eruptions involve fluid-structure coupling. The results obtained generalise all the previous analytical and numerical approaches and, in general, have an "acceptable" qualitative agreement with field observations.

5.1 Previous Considerations

5.1.1 Objectives

A major objective of this thesis is to develop an algorithm to study numerically the dynamics of magma withdrawal from crustal reservoirs. A classification of the possible numerical simulations which can be carried out is show in figure 5.1.1. Some particular frameworks –mainly central vent eruptions triggered by inflow of fresh magma into the chamber- have been already considered by other authors (see section 2.4.1.2 for major explanation). The rest of (numerical) possibilities are original contributions of this work. It can be observed form the figure how any imaginable situation can, at least theoretically, be contemplated by the model.

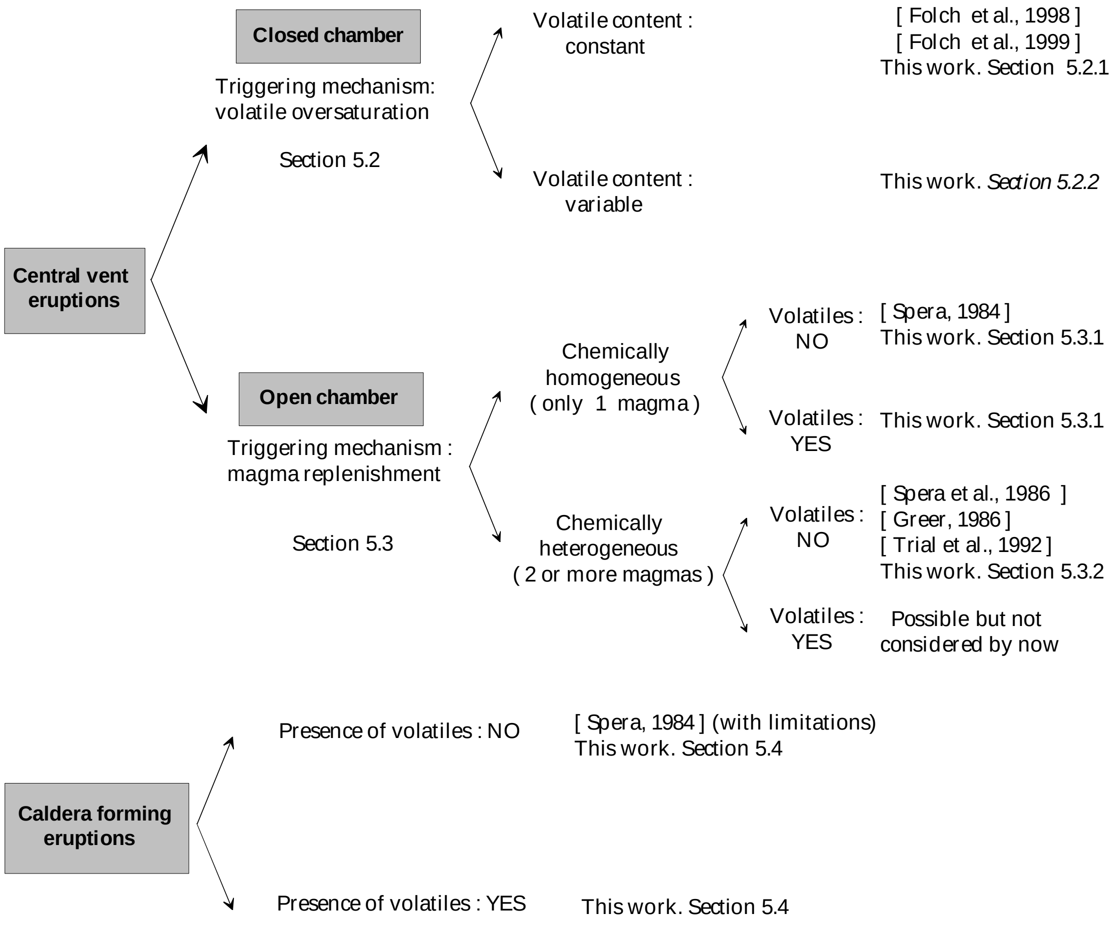

Figure 5.1.1. Classification of different possible simulations . Previous studies concerning to numerical modelling within the magma chamber as well as original contributions of this work are also shown.

Many simulations have been performed considering several geometries, different values for the parameters involved and multiple physical frameworks. Rather than an exhaustive compilation, the objective of this chapter is to present some examples of each particular case. Despite the model is not applied here to any specific real case, the examples stress general behaviours and, generally speaking, asses qualitative dependencies of the parameters involved. Simulations include both central vent eruptions (section 5.2 for the case of eruptions from closed chambers, section 5.3 for open chambers) and caldera forming eruptions (section 5.4). In the former case, the emphasis is mainly focussed to closed magma chambers because it constitutes an important contribution of this work[1]. In this case, the aim is to characterise some quantities of interest[2] such as pressure evolution, position of the exsolution level, mass discharge rate or amount of extruded material. These relevant quantities are computed over time as the simulation of the eruption proceeds. The eruption rate Q (erupted mass per unit of time) and the total erupted mass M_e are obtained, respectively, by computing the integrals

$$Q = \int_{S_c} r \; \mathbf{u} \cdot d\mathbf{s} \tag{5.1.1}$$

$$M_e = \int_0^t \mathrm{Q}(t) \, dt \tag{5.1.2}$$

where S_c is the section of the volcanic conduit. The position of the exsolution level is determined equalling the pressure to the critical pressure p_c which, for a given volatile content, is given by the equation (3.2.8).

5.1.2 Geometry and Boundary Conditions

The geometries contemplated are those sketched in figure 5.1.2. Whichever the simulation considered, the computational domain is always axisymmetric[3] and comprises a chamber (an ellipsoid or a cylinder) with radial extension $2a$, vertical extension $2b$ and a

---

[1] Eruptions from open chambers where the resident magma is volatile undersaturated are, probably, more common in nature. However, from a numerical point of view, its simulation is easier and has been already treated in previous works.

[2] The interesting variables are those which can be related, either by direct or by indirect measurements, to field observables performing geological or geochemical studies.

[3] In addition to its reasonability, the assumption of symmetry is very interesting from a computational point of view because allows to solve a three-dimensional problem like a two-dimensional one by using cylindrical coordinates.

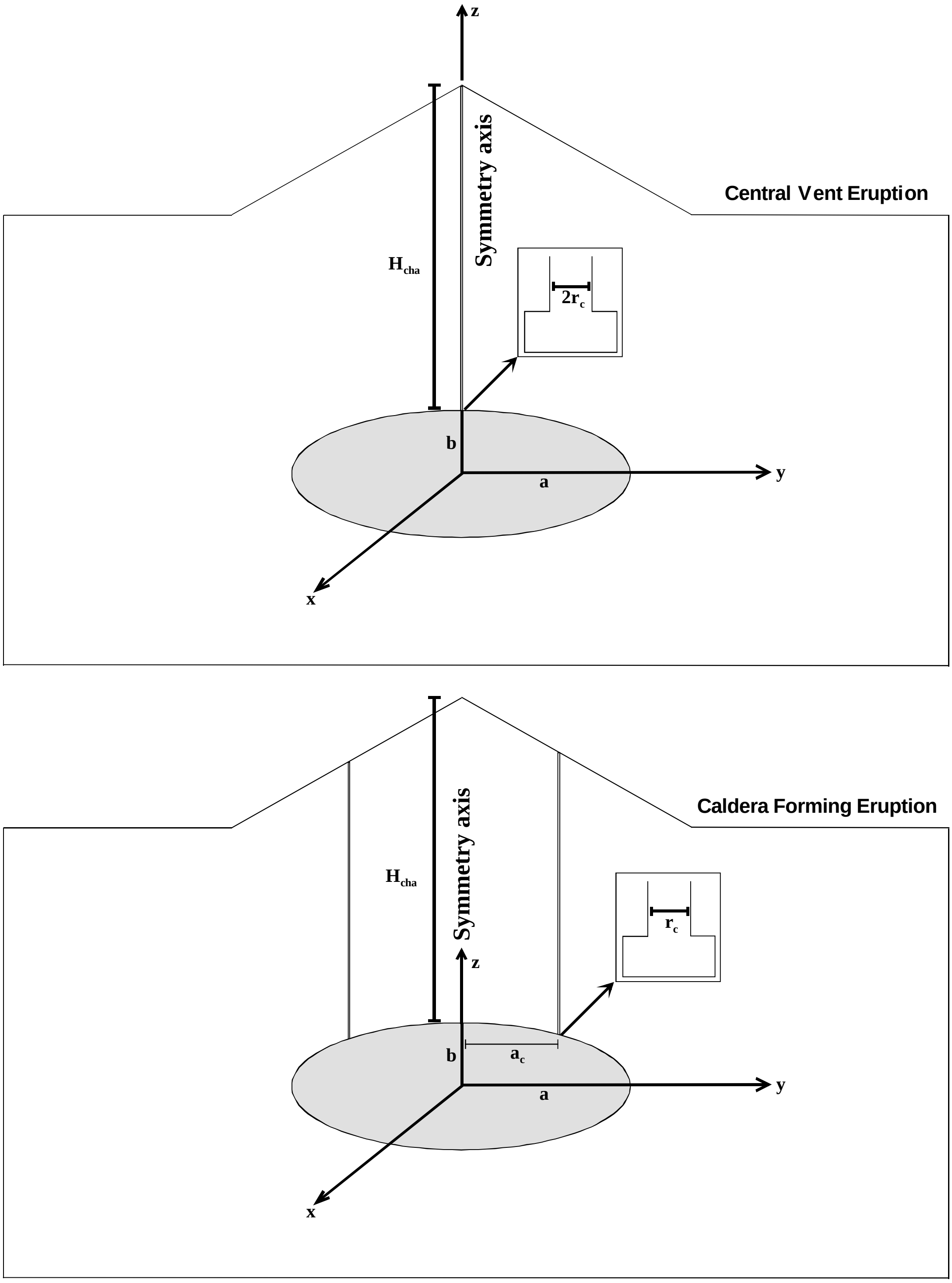

Figure 5.1.2. Top: sketch of the geometry for a generic central vent eruption with axial symmetry. An elliptical magma chamber with horizontal extension $2a$ and vertical extension $2b$ is located at depth H_{cha} below the Earth's surface. Magma flows through a conduit of radius r_c that coincides with the symmetry axis z. Computational domain is cut at a distance H_c from the top of the chamber. Cylindrical magma chambers (not shown in the figure) are also considered. Bottom: same for caldera forming eruptions. In this case, magma flows through a ring fault located at distance a_c from the symmetry axis.

vertical conduit with radius r_c. In central vent eruptions the conduit runs along the symmetry axis ($r=0$), while in caldera forming eruptions it is located at a distance a_c from the axis in order to simulate the flow of magma through a ring fault[1]. The conduit is deliberately cut at a distance H_c from the top of the chamber and, therefore, the computational outlet does not coincide with the physical one (the vent). Apparently, it might seem more reasonable to extend the conduit to the Earth's surface, i.e. consider the magma chamber and the conduit processes simultaneously, because the processes that occur in any of these domains affect the dynamics of the other. However, this would present three main numerical inconveniences:

- The state law (3.2.13) has been deduced assuming the hypothesis of homogeneity between liquid and gas phases. This hypothesis is justified as long as the bubbly flow regime can be sustained and, in consequence, becomes unacceptable at the uppermost parts of the conduit (near and above the fragmentation level). An adequate physical treatment in this region would require the solution of a non-homogeneous problem, for which governing equations for liquid and gas phases should be considered separately.
- As discussed in section 2.2.2, chemically evolved magmas show a smooth dependence of the viscosity on the amount of dissolved volatiles at high to moderate volatile content (greater than 1-2 wt.%) but, in contrast, the dependence becomes strongly non-linear at low volatile content. For practical purposes, it implies that magma viscosity can be approximated to a constant within the chamber and at the lowermost parts of the conduit but not at shallower levels, where the continuos exsolution of volatiles related to magma decompression produce a sudden increase of the viscosity by several orders of magnitude. The numerical inconveniences associated with the treatment of flows with such huge spectrum of variations in the viscosity are evident.
- The dependence of the state law on temperature becomes appreciable at low pressures, i.e. at the uppermost parts of the conduit (see figure 3.2.5). It implies that the coupling between thermal and mechanical problems should be considered at shallower levels.

All these drawbacks can be avoided limiting the computational domain. Unfortunately, one has to pay for this simplification because the boundary condition at the computational outlet becomes now an unknown of the problem. Boundary and initial conditions for both types of problems (central vent and caldera collapse) are schematically illustrated in figure 5.1.3. For central vent eruptions, the no-slip condition ($\mathbf{u}=\mathbf{0}$) is imposed at the chamber walls while only the horizontal component of the velocity is set to zero at the symmetry axis ($u_r=0$ at $r=0$).

---

[1] Note that only circular calderas can be simulated under the assumption of axial symmetry. However, this geometrical simplification should not affect the conclusions drawn here substantially.

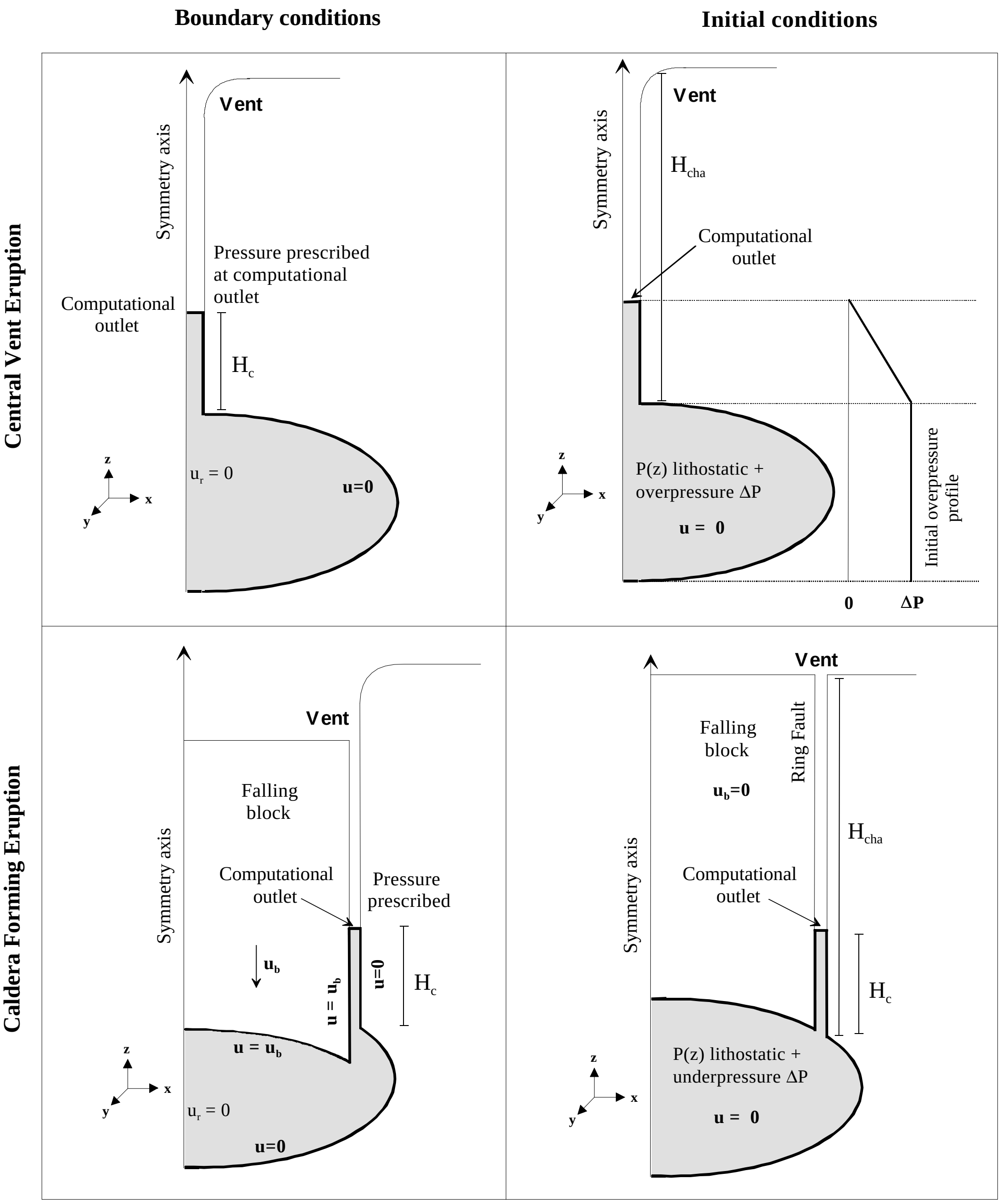

Figure 5.1.3. Schematic cartoon showing boundary and initial conditions for central vent eruptions (top) and caldera forming eruptions (bottom).

Magma inside the chamber is always in a subsonic regime [*Spera*, 1984]. Under these circumstances, either pressure or density must be prescribed as a boundary condition at the computational outlet [*Hirsch*, 1991]. As discussed previously, this outlet is set at a distance H_c above the top of chamber, where pressure is prescribed to a constant value. As a first approach, this value can be assimilated to the lithostatic despite the fact that some of the existing conduit models predict a pressure drop within the conduit below the lithostatic value [*Papale and Dobran*, 1993; *Papale and Dobran*, 1994]. This assumption can be justified *a grosso modo* because the average stress field within the conduit can not be too far from lithostatic in order to keep it open against compression of the country rocks[1]. Initial values are assigned to velocity and pressure. Magma is assumed to be at rest before the eruption. The initial pressure distribution is assumed to be hydrostatic (magmastatic) with an overpressure ΔP inside the chamber equal to the tensile strength of the host rock. The conduit has an initial overpressure that decreases linearly from a value equal to the tensile strength of the rock, at the inlet, to zero at the outlet. It should be pointed out that the flow is induced by a pressure gradient inside the conduit and, therefore, is not a departure from a state of equilibrium unstable as would, for example, be the case of thermal convection. The magnitude of the pressure gradient at the beginning of the conduit depends on how the overpressure in the chamber is dissipated along the conduit. It has been assumed that this overpressure is dissipated across H_c meters. It might be thought that the initial pressure gradient is balanced by a porosity-like force with a small porosity coefficient and a negligible initial velocity. It is in this state that the sudden (instantaneous) opening of the conduit takes place. A constant overpressure within the conduit with a sudden drop to zero at the computational outlet has been also contemplated. However, in this case, the high-pressure gradient at $t = 0$ gives rise to numerical instabilities. Concerning to caldera forming eruptions, boundary conditions are like those of central vent eruptions but having also into account the velocity of the falling block $\mathbf{u_b}$. Obviously, the non-slip condition at the walls of the block is, in this case, $\mathbf{u} = \mathbf{u_b}$.

A final remark. To avoid the coupling with the mechanical problem, the chamber and the conduit walls are assumed to be rigid and, in consequence, effects such as conduit erosion or possible contractions/expansions of the chamber/conduit walls during the eruptive process are not contemplated by the model. This hypothesis is not so restrictive as might apparently seem. Despite the rheological behaviour of the crust in areas of volcanic activity is not well established yet, it seems reasonable to assume that the only "instantaneous" deformation could come from an elastic response (viscous, plastic and other more than plausible deformations are given in a time scale much longer than the duration of an eruption), for which indirect evidences suggest constrains to its magnitude.

---

[1] If the whole conduit were considered there would not be any "problem" concerning to this outflow condition: pressure should be set to atmospheric. However, when the conduit is cut this condition becomes, in fact, time-dependent and unknown. In consequence, some approximated value must be used. Note that this approximation is very common when different parts of the domain (chamber or conduit) are considered separately. Thus, for instance, most of the conduit models available in literature assume also a constant pressure at the entrance when, in fact, it is a time dependent value which depends on the dynamics of the chamber withdrawal.

5.1.3 A Relation between W and ΔP

In eruptions from closed magma chambers the volatile mass fraction W cannot be arbitrary because one must ensure that the chamber is, at least partially, oversaturated in volatiles in order to produce the overpressure ΔP required to trigger the eruption. On the other hand, once magma is oversaturated, there must be some relationship between the amount of volatiles and the overpressure within the chamber exerted by them. In other words, once one parameter (W or ΔP) is fixed the other is, at least theoretically, automatically determined. This relationship is, in general, complex. However, and as a first approach, a simple relation can be determined assuming some simplifications. Consider an initial situation in which a chamber of volume V_c at pressure P_0 is filled with undersaturated magma with a volatile content W_i (i.e. $V_c = V_{si}$). Gradients on pressure and volatile content are neglected for simplicity. On further fractional crystallisation this chamber evolves into a stage in which the volatile mass fraction rises to W_f and, eventually, gas bubbles are exsolved at the top of the chamber, where the ambient pressure is lower. In order to fit into the available space, these bubbles compress the pre-existing magma and rise the pressure of the chamber to $P_0 + \Delta P$. The chamber is now occupied by the volume of the gas V_g plus the volume of the remainder magma V_{sf} (i.e. $V_c = V_{sf} + V_g$). This situation is illustrated in figure 5.1.4.

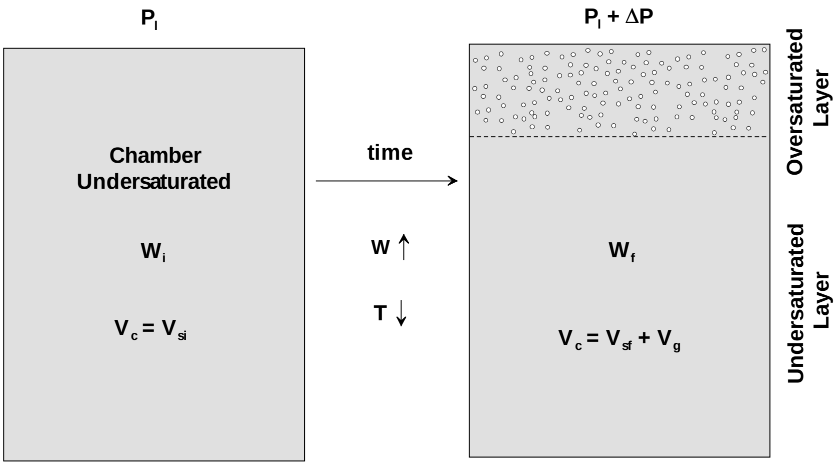

Figure 5.1.4.Schemmatic illustration of the fractional crystallisation process. Initially, a chamber at lithostatic pressure P_0 is filled with magma undersaturated in volatiles. The whole chamber volume V_c is occupied by liquid magma with a volatile mass fraction W_i ($W_i < sP_0^m$). After some period of time the chamber cools, some crystalline components are removed form the melt and the volatile mass fraction increases to W_f. Eventually, the uppermost parts of the chamber (where pressure is lower) become oversaturated in volatiles and gas bubbles are exsolved. These bubbles compress the pre-existing magma and rise the chamber pressure to $P_0 + \Delta P$.

If one assumes that the chamber has rigid walls then

$$V_c = V_{si} = V_{sf} + V_g \tag{5.1.3}$$

The compression of the melt can be related to pressure variations considering

$$V_{sf} = V_{si}\, e^{-\frac{\Delta P}{b}} \tag{5.1.4}$$

so that

$$V_{sf} - V_{si} = V_{si}(e^{-\frac{\Delta P}{b}} - 1) \cong V_{si}(-\frac{\Delta P}{b}) \quad \Rightarrow \quad V_g \cong V_{si}\frac{\Delta P}{b} \tag{5.1.5}$$

where b is the compressibility modulus. On the other hand, mass conservation implies

$$m_{si} = m_{sf}\frac{1}{1-n_g} \tag{5.1.6}$$

$$m_{si} = m_{sf} + m_g = m_{sf} + \frac{V_g}{r_g} \tag{5.1.7}$$

where m_s is the mass of the melt (liquid plus dissolved volatiles within), m_g is the mass of the gas and n_g is the mass fraction of gas (see 3.2.5). Equalling the above expressions, using (5.1.5) and assuming a perfect gas behaviour for the bubbles one has

$$m_{sf}\frac{n_g}{1-n_g} = V_{si}\frac{\Delta P}{b}\frac{(P_0 + \Delta P)}{QT} \tag{5.1.8}$$

and, finally, considering that $r_l = m_{si}/V_{si} \cong m_{sf}/V_{si}$ and using (3.2.6) and (3.2.7) one obtains

$$\frac{W - s(P_0 + \Delta P)^m}{1-W} = \frac{\Delta P}{r_l\, b}\frac{(P_0 + \Delta P)}{QT} \tag{5.1.9}$$

or, equivalently

$$W = \frac{\Delta P\,(P_0 + \Delta P) + r_l\; b\; QT\; s(P_0 + \Delta P)^m}{\Delta P\,(P_0 + \Delta P) + r_l\; b\; QT} \tag{5.1.10}$$

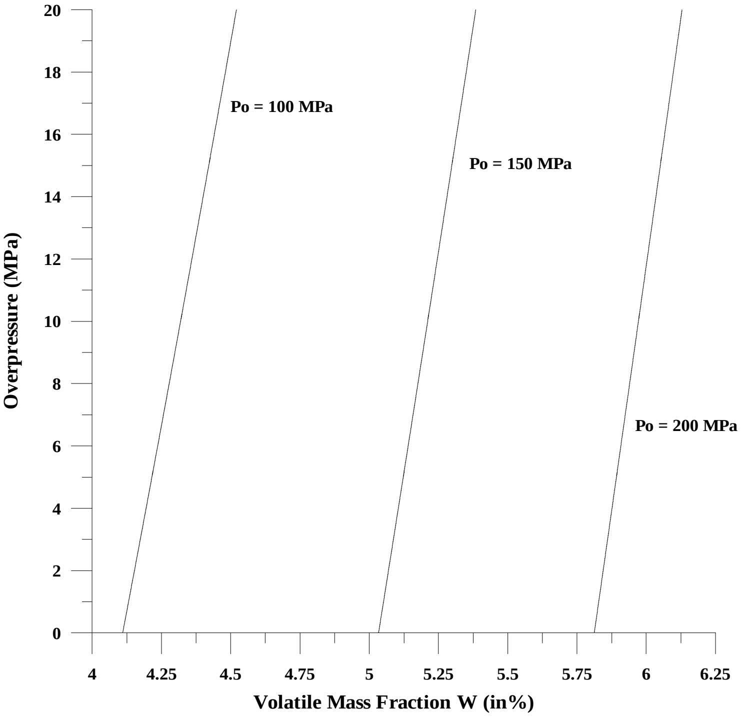

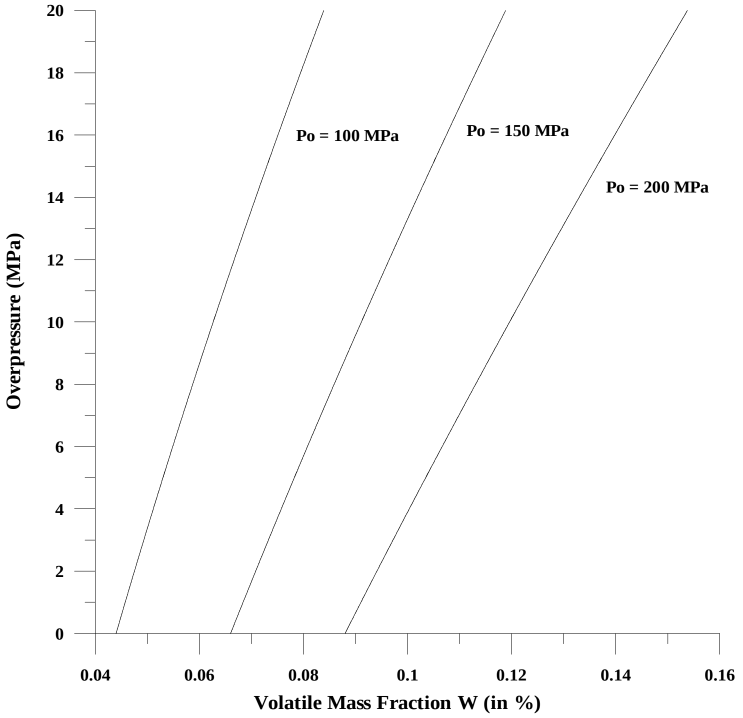

Figure 5.1.5. Chamber overpressure (in MPa) as a function of volatile mass fraction W (in weight %) according to equation 5.1.10. Results for rhyolite-water (top) and basalt-carbon dioxide (bottom) for different lithostatic pressures P_0 of 100, 150 and 200 MPa respectively and assuming standard values for the rest of parameters.

Equation (5.1.10) proportionates an approximate relation between W and ΔP (≥ 0). Note that, in particular, when $\Delta P = 0$ (i.e. when the overpressure starts) the condition of melt saturation $W = sP_0^m$ is recovered. The values of W and ΔP in any numerical simulation of closed systems should be consistent with this expression[1]. Obviously, this condition is not a necessary requirement in the case of open systems, where part (if not all) of the critical overpressure is induced by injection of fresh magma into the chamber. Figure 5.1.5 shows the results predicted by (5.1.10) for a rhyolite (assuming H_2O as the only volatile) and for a basalt (assuming CO_2 as the only volatile) assuming standard values for the rest of parameters involved. Note how, in general, once the chamber is oversaturated, a relative small increase in the volatile mass fraction is able to induce a high overpressure due to the low compressibility of the undersaturated magma.

5.1.4 Time Step

It should be mentioned that a serious numerical limitation due to the critical time step has been found, in general, when using the magma state law (3.2.13). This limitation comes from the fact that one must use a very small critical time step to simulate a process which typically lasts several hours[2]. As exposed in section 4.1.7, the critical time step for the Navier-Stokes equations is[3]

$$\Delta t \leq \frac{F_s}{\frac{4m}{r\,h^2} + \frac{2|\mathbf{u}|}{h}} \leq \frac{F_s\; r\,h^2}{4\,m} \qquad (5.1.11)$$

where m is viscosity, r is density, h is the element size and F_s is a safety factor. In general, if one is interested only on the steady solution, a common procedure to accelerate the convergence of the solution is to use local time steps. It allows to use different time steps for each node of the mesh and, in consequence, accelerates convergence and reduces notably the computational cost required to reach the steady state. This strategy can not be applied here

---

[1] This expression is approximated due to the mumerous oversimplifications. It means that, given an overpressure, the value of W proportionated by (5.1.10) should be considered only as a rough guide. Hence, "small" variations of this W do not necessary imply loose of physical meaning.

[2] Note that, although this problem can be reduced improving the efficiency of the source code, it exists independently of it.

[3] Strictly, this value is for the momentum equation and considering linear elements. For higher-degree elements the value of Δt is much lower.

because the interest focuses on the description of a transient evolution. It implies that one must consider a global time step equal to the minimum elemental time step of the mesh. The problem in the case of the simulations shown along this chapter can be illustrated considering typical magma values: $m = 10^5$ Pa.s and $r = 2500\,\mathrm{Kg/m^3}$. Assuming $F_s = 1$ and using these values one has $\Delta t \le 6\times10^{-3}\, h_{min}^2$. Obviously the Δt value depends on the elemental size which, for the geometries considered, is constrained by the radius of the conduit $r_c = 25-50\,\mathrm{m}$. Taking $h_{min} = 10\,\mathrm{m}$ as an upper value, one has $\Delta t \le 0.6\,\mathrm{s}$ ($F_s = 1$). The problem is that, using time steps of the order or lower than 0.5s, on has to deal with a transient process which starts far away from the steady state and that typically takes several hours to reach it (i.e. tens/hundreds of thousands of iterations are necessary for each specific simulation). In principle, one has two main strategies to face this inconvenience. The first would be to use the fully explicit version of the algorithm with lumped matrixes. Obviously, this choice it the one with less computational cost (CPU time) for iteration but, in contrast, stability criteria demands for safety factors lower than one. The second option would be to use the fully implicit version which, despite having the higher computational cost per iteration, seems a better choice because, *a priori*, the safety factor can be notably increased. Unfortunately, it has been found that the characteristics of the state law do not permit, for most of the simulations performed, safety factors greater than 0.1-0.5 in the fully explicit version and than 2-5 in the fully implicit[1]. All in all, the final result is that both strategies require similar CPU times but, in general, the fully implicit version of the algorithm is preferable because is a bit faster and more stable. All the strategies considered to increase stability (to use higher safety factors) such, for instance, the pressure gradient projection or different treatments of the state law in the continuity equation (see table 4.1.2), have failed. It implies that, lamentably, the only remainder possibility to have "reasonable" CPU times seems to be a constriction on the size of the mesh[2]. Meshes with sizes greater than 10.000-15.000 elements have been rejected. Using these relatively coarse meshes, a simulation takes typically about 24h of CPU (100.000 iterations)[3].

---

[1] This fact is a characteristic of the state law. When other types of flow (incompressible, barotropic, perfect gas, etc.) are considered the safety factor can be considerably higher. Thus, for instance, a driven cavity flow with the fully implicit option can perfectly hold safety factors higher than 1000.

[2] The program runs under a SGI Origin 2000 (8 CPU R10000). CPU times greater than 48h are considered unacceptable.

[3] Obviously this value depends on the critical time step which, in turn, is also dependent on magma density and viscosity.

5.2 Withdrawal from Closed Magma Chambers

This section presents some numerical examples of withdrawal from closed magma chambers (volatile oversaturation driven eruptions). Generally speaking, the simulations allow to characterise the temporal evolution of some relevant parameters such as the evolution of pressure and exsolution level, the mass discharge rate or the amount of extruded material during the course of explosive volcanic eruptions. Simulations are not applied to any specific case. However, some relevant conclusions concerning qualitative behaviours and parametrical dependencies can be envisaged.

5.2.1 Constant Volatile Content

Several simulations have been performed considering different geometries, different magma properties and different values of the physical parameters involved. Obviously, the quantitative results depend on each specific case but, nevertheless, the qualitative tendencies are common to all the simulations.

5.2.1.1 General Overview

As an example, consider the case of the withdrawal from an imaginary cylindrical chamber filled with chemically evolved magma (rhyolite). Despite a cylindrical geometry may not be very realistic from a physical point of view, the shape of the chamber is not a relevant aspect if one aims only to stress those qualitative characteristics which have been found in all the simulations. This imaginary chamber has an horizontal extension of 2Km ($a = 1\text{Km}$) and a vertical extension of 1Km (i.e. 3.14 Km^3 of volume). The radius of the conduit is $r_c = 50\text{m}$ and the computational outlet has been cut 250m above the chamber top. At the outlet, pressure is fixed to an arbitrary lithostatic value of 100MPa. Note that this value does not imply any particular depth for the chamber because the relation between depth and lithostatic pressure depends on the host rock mean density. The initial overpressure is $\Delta P = 10\,\text{MPa}$, a typical value for the tensile strength of the host rocks [*Touloukian et al.*, 1981]. Figure 5.2.1 shows the spatial discretisation, for which a relatively coarse (but sufficient) mesh made up with 6036 triangular elements and 3149 nodal points has been employed. The chamber is filled with a rhyolitic magma having density $r_l = 2400\,\text{Kg/m}^3$, temperature $T = 850^\circ\text{C}$, viscosity $m = 10^5\,\text{Pa.s}$ and a (constant) water content of $W = 0.045$ (4.5% in weight)[1]. Note that, in this case, it is assumed

---

[1] This water content is "relatively consistent" with the relationship between W and ΔP deduced in section 5.1.3.

that the overpressure which allows to trigger the eruption is achieved by oversaturation of volatiles and, in consequence, the amount of volatiles (water) can not be arbitrary: one must have a value of W for which magma vesiculates at pressures greater than $100+\Delta P$ MPa. Under these conditions, the volume of the chamber initially vesiculated is 6.6%, i.e. the exsolution level is located 66m below the top of the chamber.

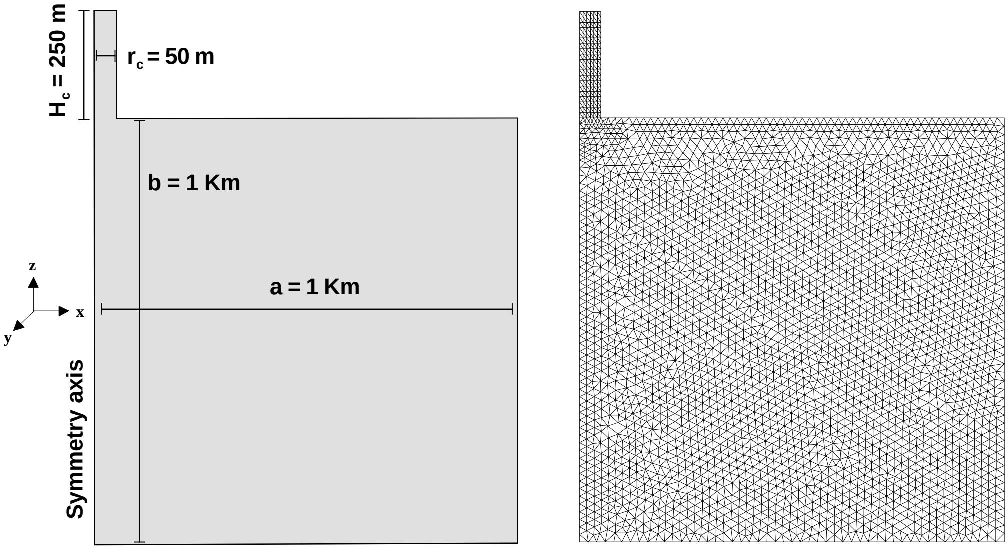

Figure 5.2.1. Geometry and space discretisation.

Numerical results show that the initial overpressure decreases exponentially as the eruption proceeds until it becomes zero and the eruption ceases. In other words, eruption ends once the lithostatic (magmastatic) pressure profile is achieved, i.e. when the initial overpressure has been dissipated. Since the model assumes that solubility depends only on pressure (Henry law) this decrease on pressure produces a drop in the exsolution level so that deeper parts of the chamber become progressively oversaturated in volatiles as the eruption proceeds. The upper oversaturated magma layer becomes thus progressively thicker and less dense. Figure 5.2.2 shows the temporal evolution of the exsolution level as well as the pressure at the entrance of the conduit for this particular simulation. The duration of the eruption is, in this case, less than 1h and the exsolution level presents a total shift of about 550m. Figure 5.2.3 shows the initial and final density and pressure profiles inside the chamber. Figure 5.2.4 shows the temporal evolution of the eruption rate at the computational outlet[1] and the velocity at the entrance of the conduit. The eruption rate reaches a peak immediately after the onset of the eruption and then decreases also exponentially.

---

[1] As noted previously, the computational domain is not extended to the surface. In consequence, and due to the compressibility of the magma at the uppermost parts of the conduit, the eruptive rate at the conduit entrance must not necessarily coincide with that observed at the Earth's surface. However, both intensities should not differ substantially.

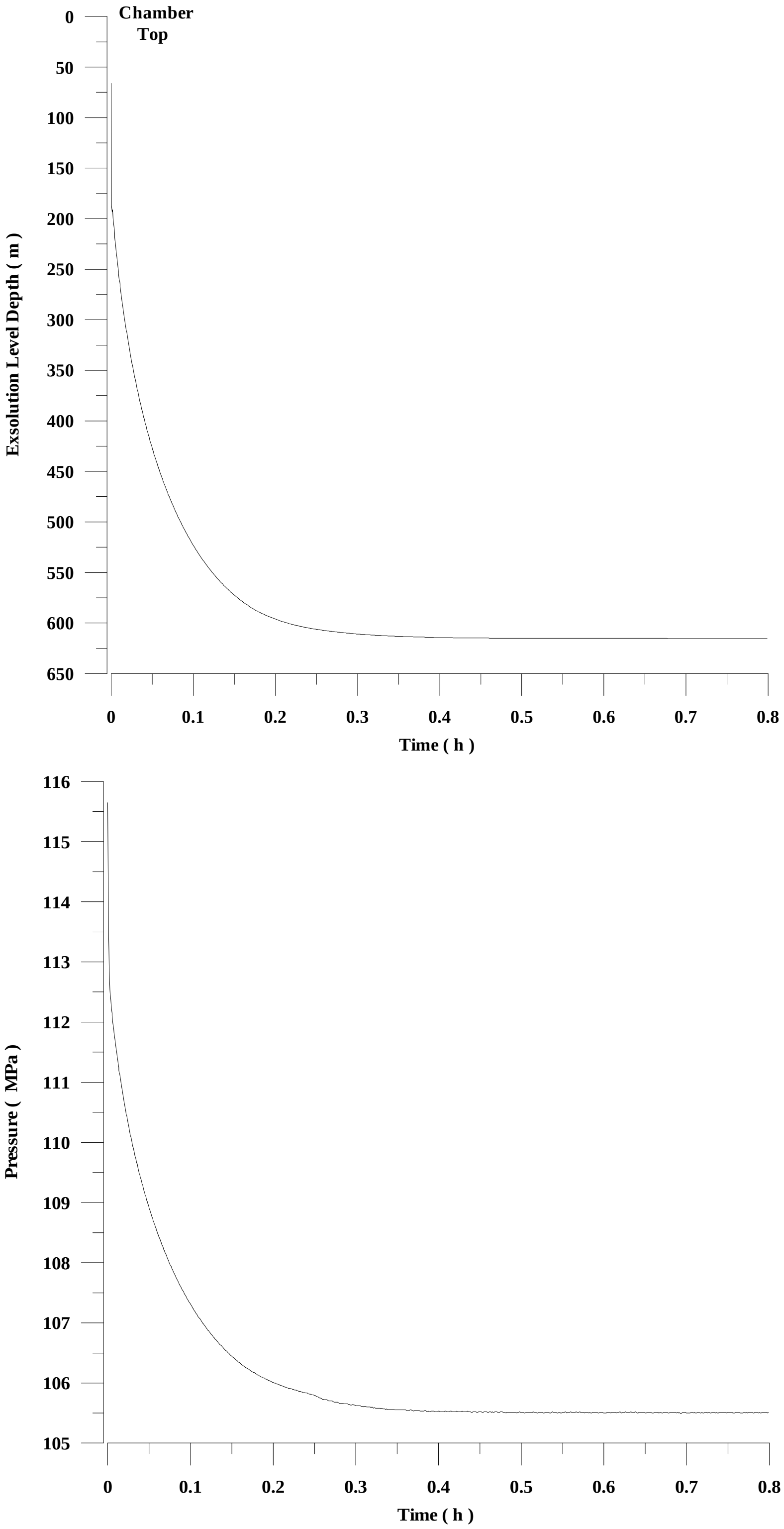

Figure 5.2.2. Top: position of the exsolution level (in m) plotted versus time (in hours). In this graphic, the vertical axis has its origin at the top of the chamber and is positive downwards. Bottom: pressure (in MPa) at the conduit entrance plotted versus time (in hours). Eruption ends when the lithostatic pressure profile is recovered, i.e. when the initial overpressure (10MPa) is dissipated.

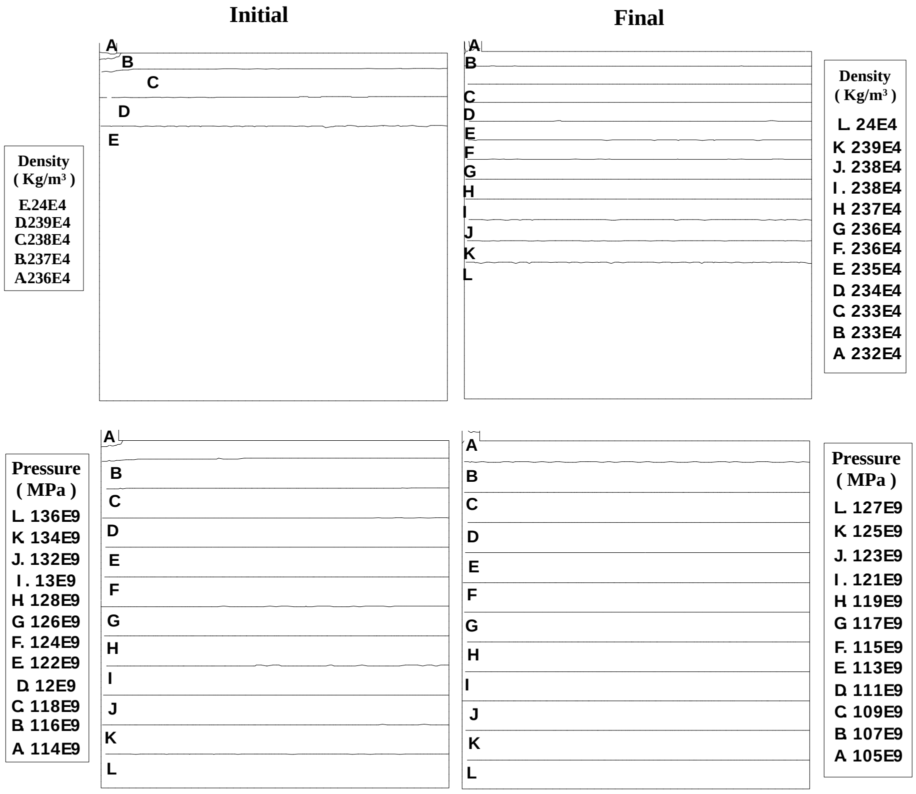

Figure 5.2.3. Density (kg/m^3) and pressure (MPa) profiles inside the chamber. Left: results at the onset of the eruption when only the uppermost part of the chamber is vesiculated. Right: results at the end of the eruption (t = 1h). Note the drop in the exsolution level due to the decrease in pressure.

This behaviour seems not to be very realistic because many Plinian eruptions present phases in which the eruption rate decreases progressively and then reaches a new peak of intensity. This apparent discrepancy could be explained by two main reasons. Firstly because the hypothesis of closed system and, secondly, due to the assumption of homogeneity (these Plinian phases are commonly associated with tapping effects [*Dobran*, 1992], where the magma that reach the conduit changes its properties -viscosity, volatile content, etc.- as a consequence of pre-eruptive heterogeneities). Finally, figure 5.2.5 shows the total erupted mass and the erupted mass fraction (erupted mass divided by the initial mass) as a function of time. It can be observed how the total erupted mass is only about 0.9% of the original mass. This result is in good agreement with the analytical time-independent results of [*Bower and Woods*, 1997], who found that in close volatile-saturated magma chambers only a mass fraction in the range of 0.1%-1% of the initial mass is erupted. In addition, numerical simulations allow to predict not only the total mass erupted but also its temporal variation for any given chamber geometry and set of magma properties. Obviously, these values are particular of this simulation (other chamber and conduit geometries, volatile content, magma viscosity, etc. produce quantitative results substantially different) but the qualitative behaviour does not.

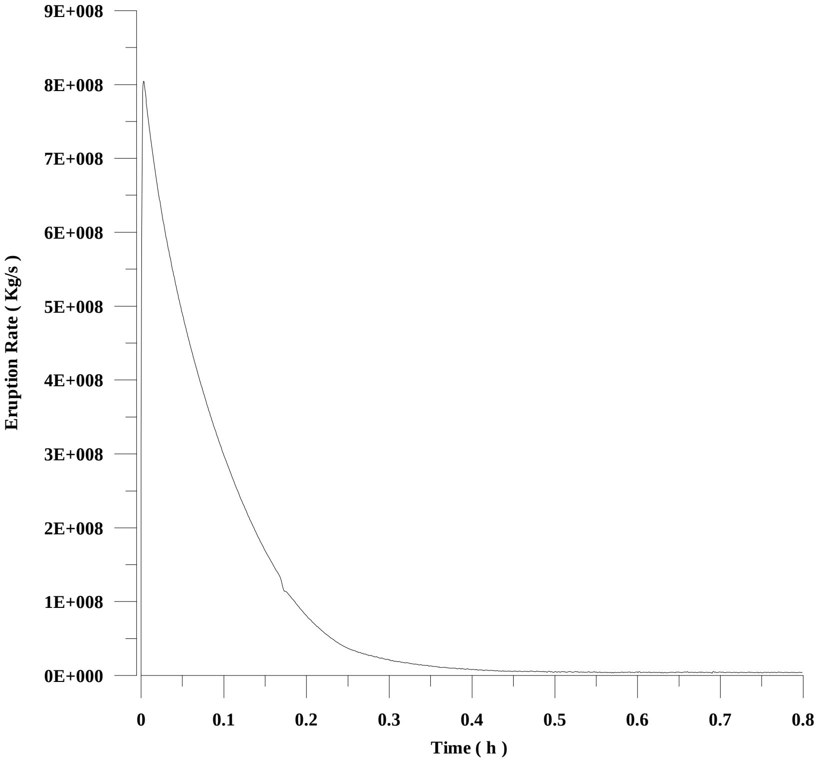

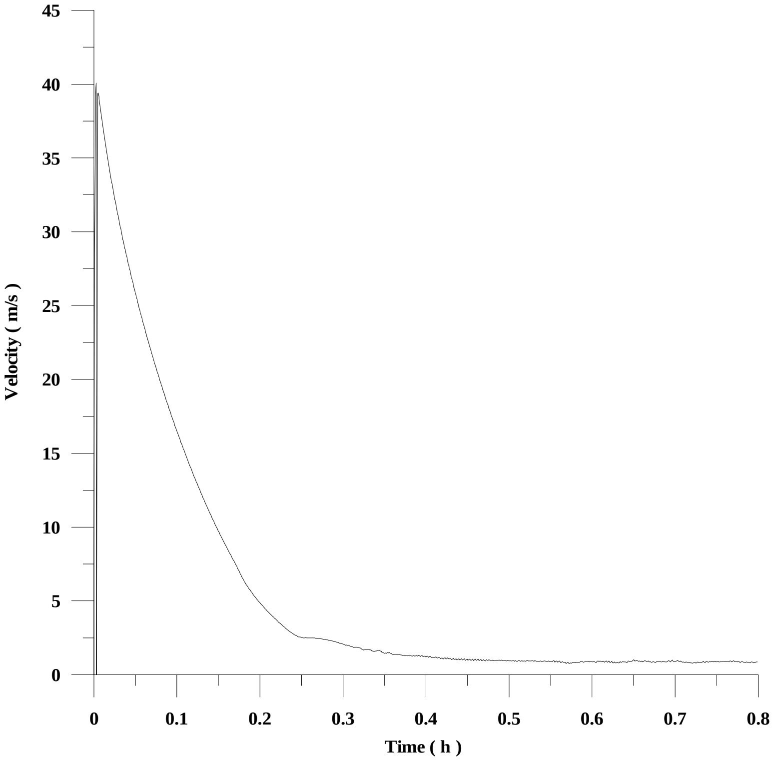

Figure 5.2.4. Top: eruption rate (Kg/s) at the computational outlet versus time (in hours). Bottom: velocity (m/s) at the conduit entrance versus time.

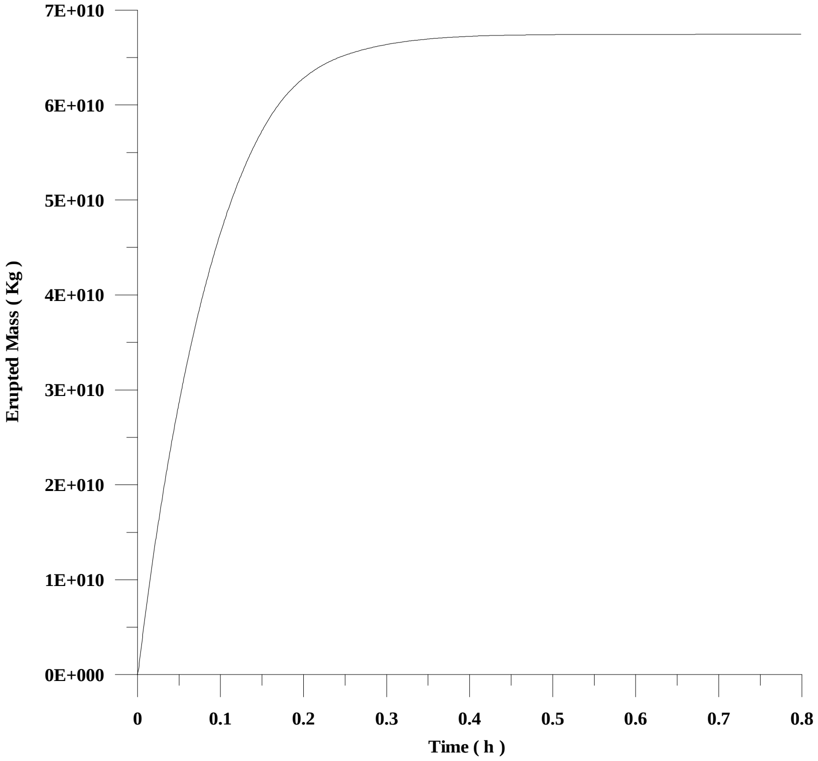

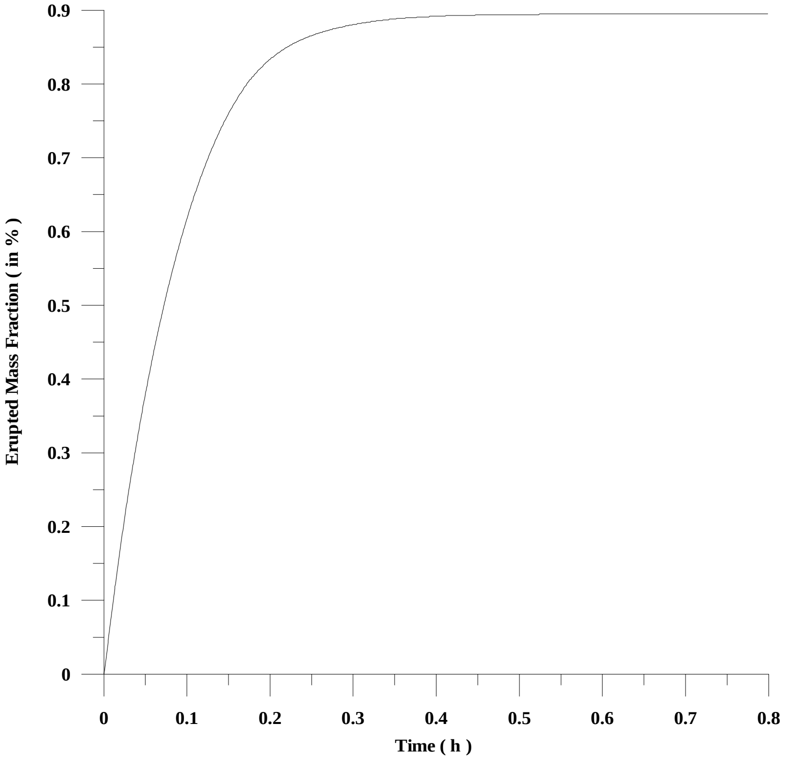

Figure 5.2.5. Erupted mass and erupted mass fraction plotted versus time. Note that only a small mass fraction (around 1%) is erupted.

5.2.1.2 A Parametrical Study

Many parameters such viscosity, gas content, magma chamber geometry or initial overpressure appear in the model and their influence on the solution is not always clear. Among them, the most relevant is probably the geometry of the chamber. In order to assess its importance, three different magma chambers with a similar volume of ≅ 14 km^3 have been considered. Chamber 1 is oblate (sill-like), chamber 2 is spherical and chamber 3 is prolate (dike-like). The dimensions of these chambers are of the same order of magnitude as natural shallow magma chambers but do not represent any particular volcanic system. Figure 5.2.6 shows its geometries as well as the spatial discretisations performed. In all cases, the FEM meshes are non-structured and made up with linear triangular elements (4482, 7732 and 9724 elements for sill-like, sphere and dike-like, respectively). The conduit has a radius of $r_c = 25\,\mathrm{m}$ and is terminated at $H_c = 250\,\mathrm{m}$ above the chamber. Again, the chamber is filled with rhyolitic magma with density $r_l = 2400\,\mathrm{Kg/m^3}$, temperature $T = 850^\circ\mathrm{C}$, viscosity $m = 10^5\,\mathrm{Pa.s}$ and water content $W = 0.045$ (4.5% in weight). Lithostatic pressure and initial overpressure are, respectively, 100 and 10 MPa.

Figure 5.2.7 shows the temporal evolution of pressure and eruption rate at the entrance of the conduit. The position of the exsolution level as well as the erupted mass fraction are depicted in figure 5.2.8. It can be observed from these figures how, for chambers of equal volume and magma properties, the qualitative behaviour is insensitive to the chamber geometry. However, from a quantitative point of view, the flatter the chamber the slower the decompression process. This implies that the exsolution level evolves faster in dike-like chambers than in sill-like reservoirs. Obviously, its final position is the same for all the cases since the amount of volatiles is identical (4.5% in weight) in all the simulations. Another important result is that, although shapes of the curves are similar in all three cases, the total mass erupted (i.e. also the erupted mass fraction) increases as the chamber becomes flatter. This is explained by the fact that magma is nearly incompressible below the exsolution level (fully incompressible in our model) but above this level the mixture, containing exsolved gas, becomes much more compressible. Thus, the total mass erupted corresponds only to the volume change in the upper compressible layer as a response to the pressure variation. In consequence, those chambers containing more magma in the upper oversaturated layer (i.e. horizontally flattened chambers) will erupt a greater amount of material for a given pressure decrease. In this particular example, the erupted mass fractions found are about 0.8%, 0.1% and 0.04% for sill-like, spherical and dike-like chambers respectively. This is in excellent agreement with the predictions of analytical models available in literature (e.g. [*Bower and Woods*, 1997; *Martí et al.*, 2000]).

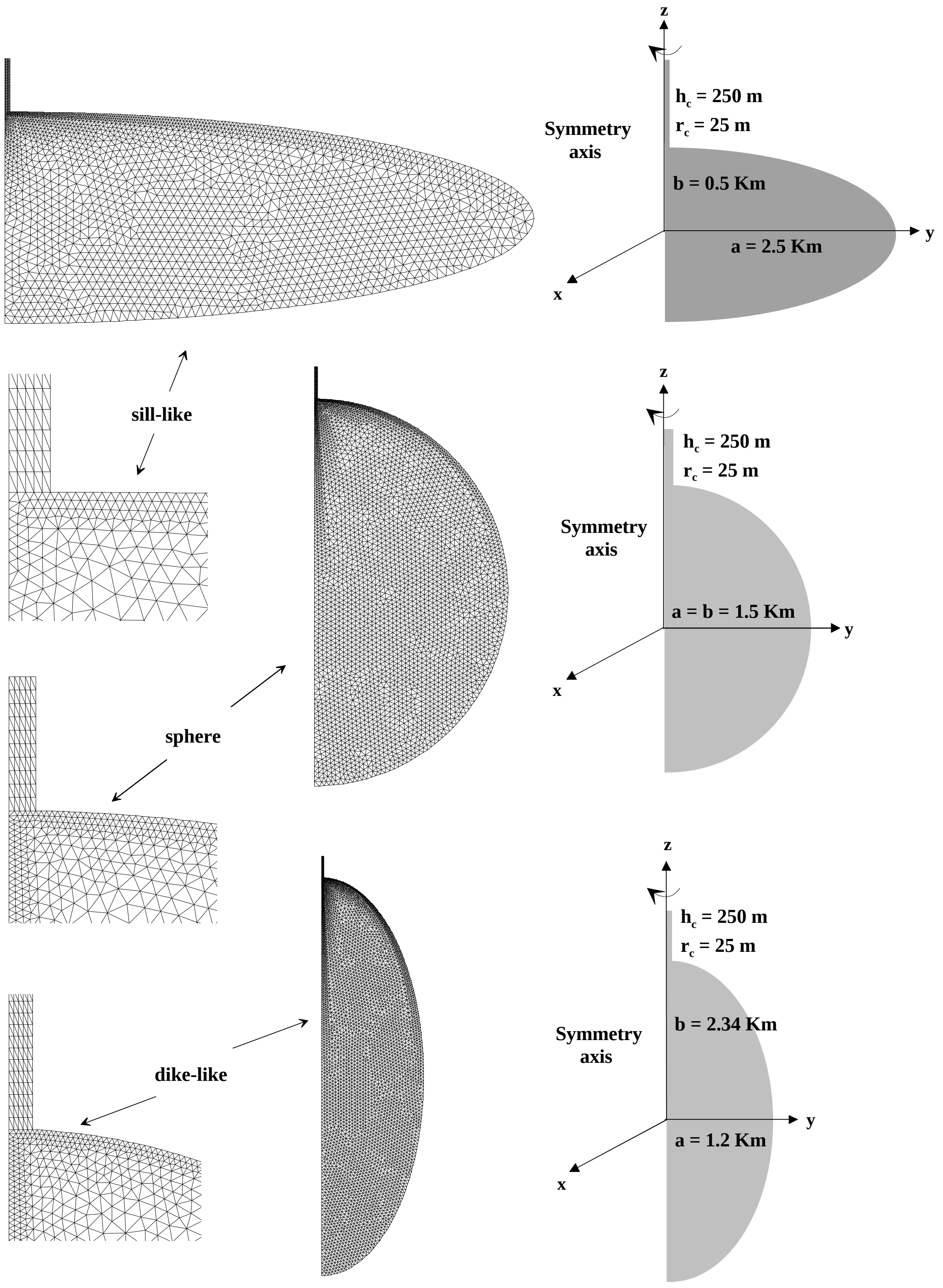

Figure 5.2.6. Geometries and space discretisations (at different scales). Close up views around the entrance of the conduit are also shown.

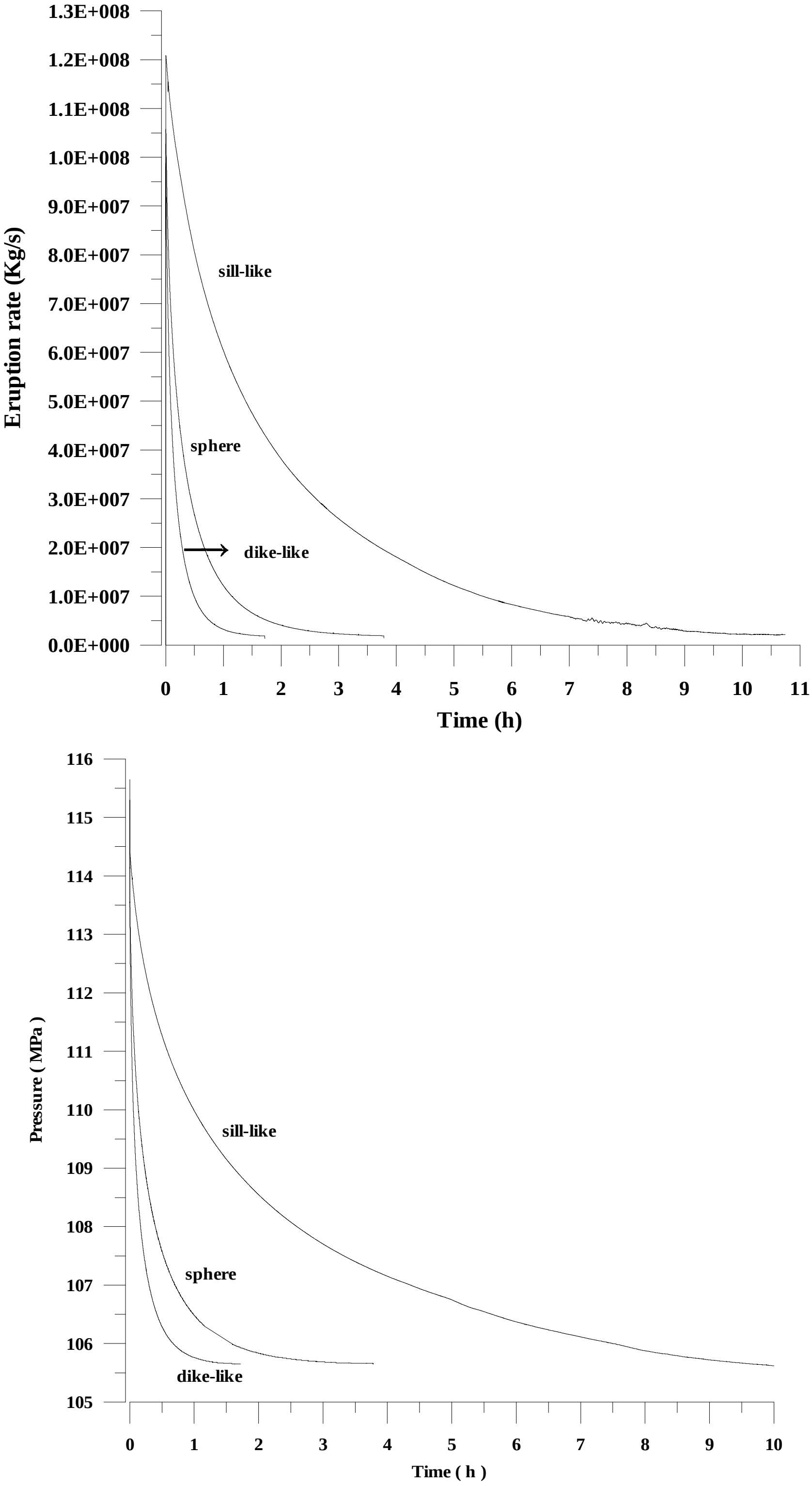

Figure 5.2.7. Eruption rate (top) and pressure at the entrance of the conduit (bottom) plotted versus time for three different geometries of the chamber.

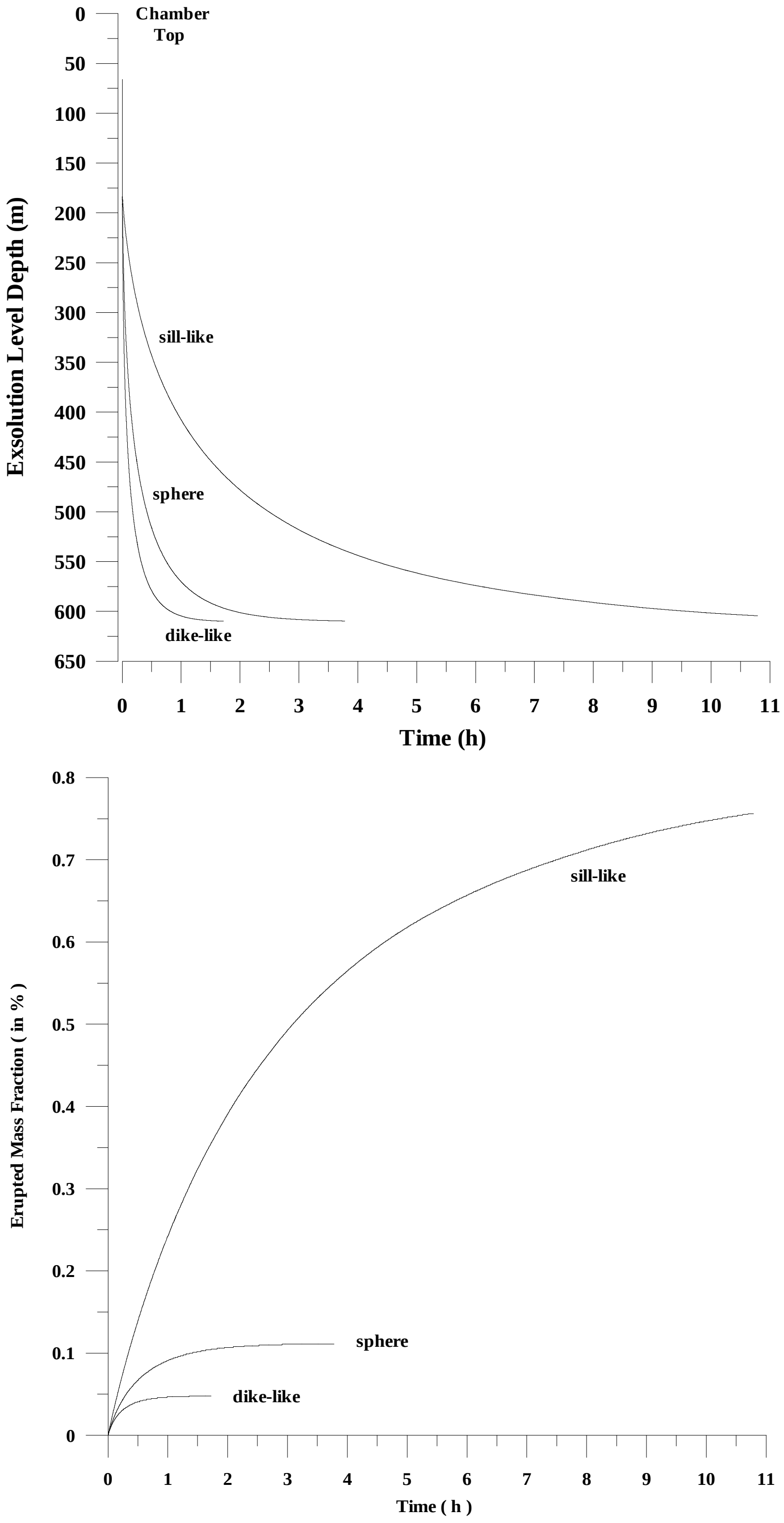

Figure 5.2.8. Position of the exsolution level (top) and erupted mass fraction (bottom) plotted versus time for three different geometries.

The influence of other parameters different from geometry has been also envisaged. To simplify, only some examples restricted to the sill-like chamber are presented here. Figures 5.2.9 and 5.2.10 illustrate the effect of varying viscosity on several quantities of interest. It can be seen how, the less viscous the magma, the faster the chamber becomes depressurised. In consequence, the position of the exsolution level changes faster in chambers filled with less viscous magmas despite the fact that its initial and final positions are, for a given pressure decrease ($\Delta P = 10\ \mathrm{MPa}$ in this case), independent of the magma viscosity. Although the total erupted mass is also independent on viscosity, this parameter plays a major role in controlling the duration of the eruption. As expected, the more viscous the magma, the longer the duration of the eruption and the lower the peak of the eruption rate. That is, chambers containing a less viscous magma are more rapidly withdrawn and have a higher intensity peak.

The influence of volatile content on the eruption rate and on pressure variations is now considered. Again, the examples are obtained using magma chamber 1 (oblate ellipsoid or sill-like chamber), an initial overpressure of $\Delta P = 10\ \mathrm{MPa}$, a viscosity of $m = 10^5$ Pa s, and a density of $r_l = 2400$ kg/m^3. The effect of varying volatile content is illustrated in figures 5.2.11 and 5.2.12. As observed from these figures, a small change on volatile content has an important effect on the position of the exsolution level. Its total displacement is not much sensitive to the amount of volatiles (for a given pressure decrease), but its initial and final positions vary notably : a small increase in volatile content produces a substantial deepening of the exsolution level (thus, in this particular example, if the amount of volatiles –water- is 4.7% in weight the whole chamber vesiculates before the end of the eruption). As a consequence, the duration of the eruption and the amount of extruded material also increases because there is more magma in the compressible layer (above the exsolution level). Table 5.2.1 summarises some qualitative results of the parametrical study

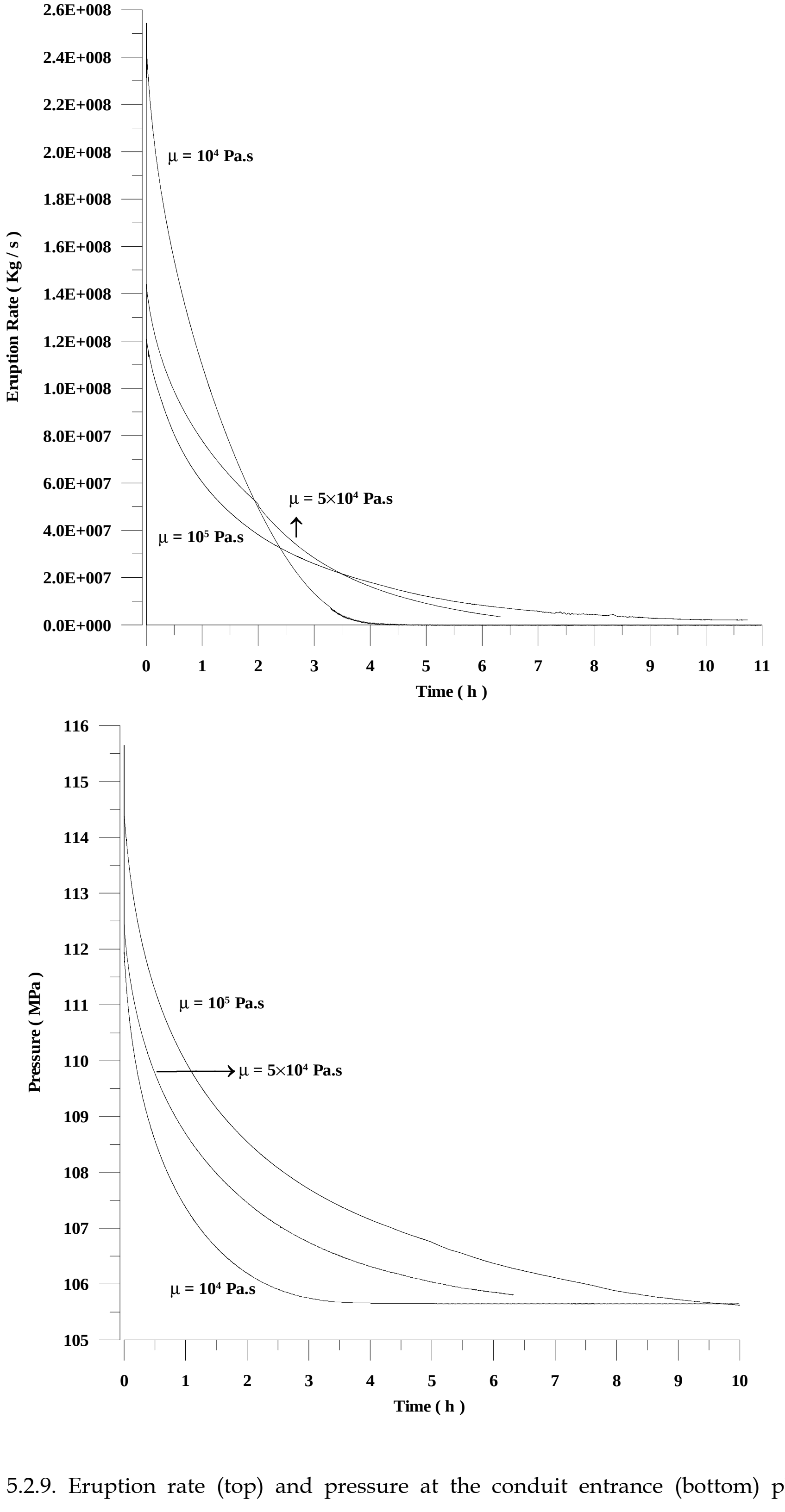

Figure 5.2.9. Eruption rate (top) and pressure at the conduit entrance (bottom) plotted versus time for the sill-like chamber with a volatile content of 4.5% in weight and considering three different viscosities of 10^4, 5×10^4 and 10^5 Pa.s respectively.

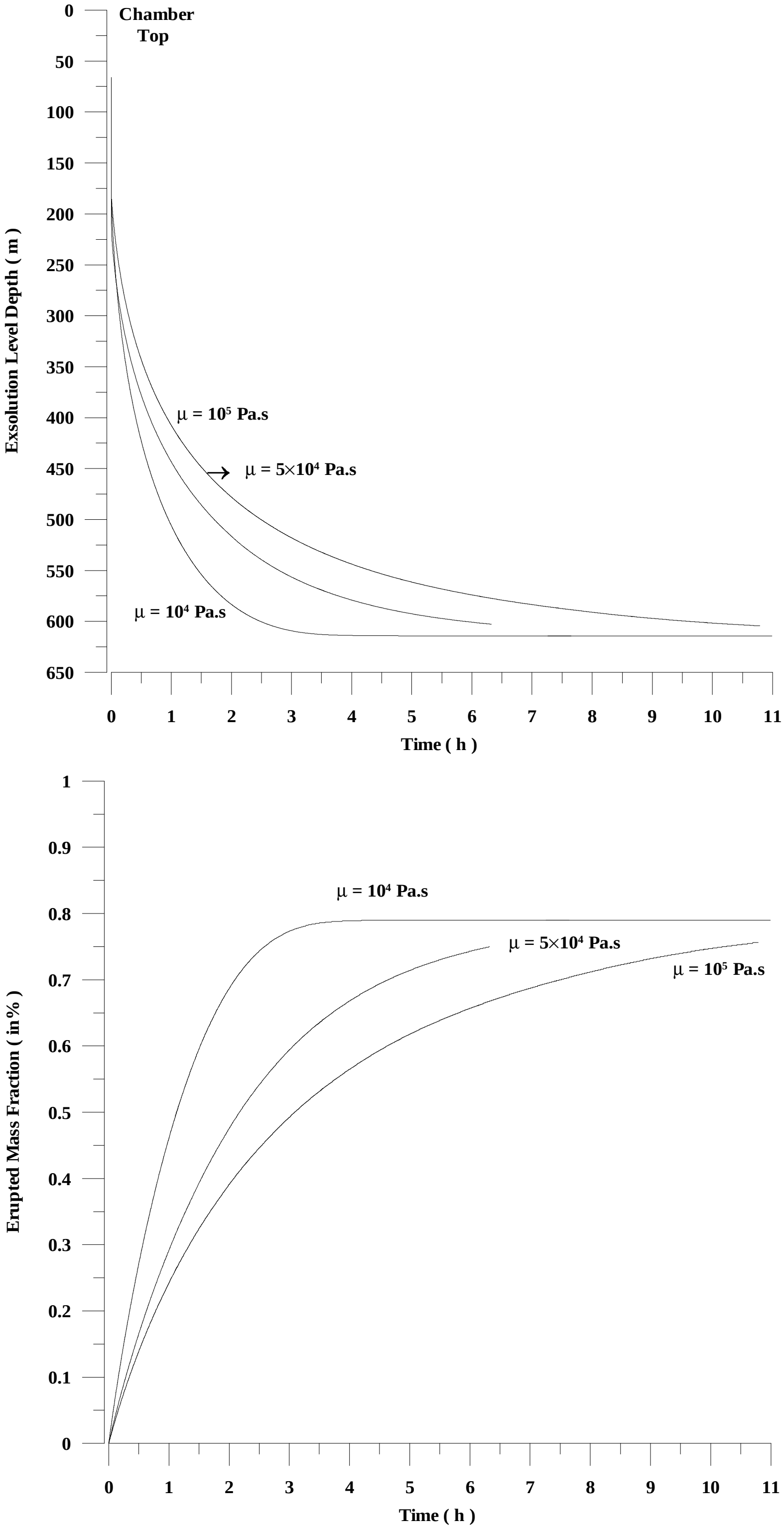

Figure 5.2.10. Position of the exsolution level (top) and erupted mass fraction (bottom) plotted versus time for the sill-like chamber with a volatile content of 4.5% in weight and considering three different viscosities of 10^4, 5×10^4 and 10^5 Pa.s respectively.

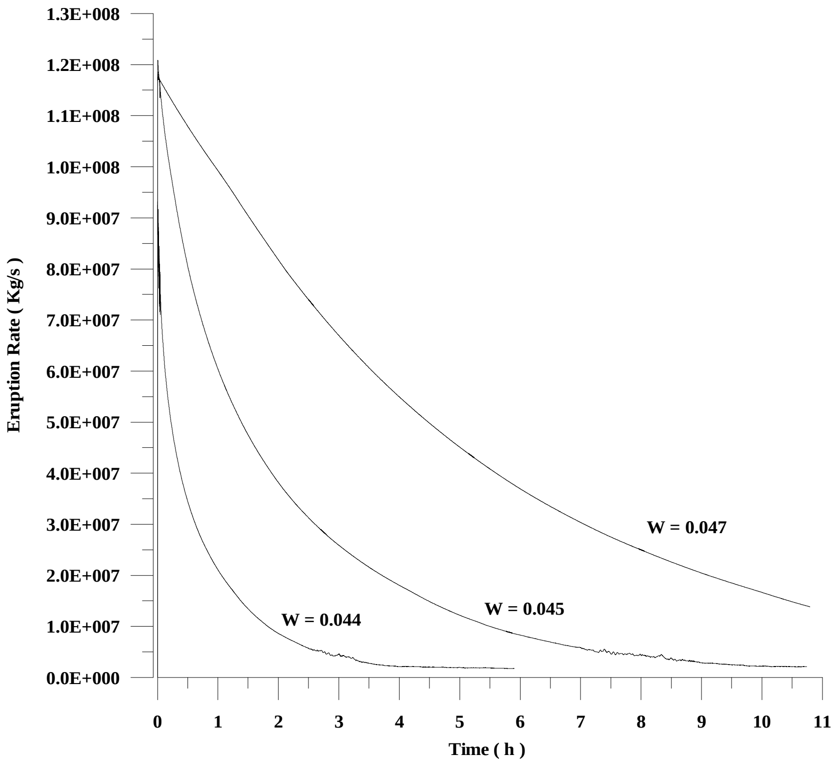

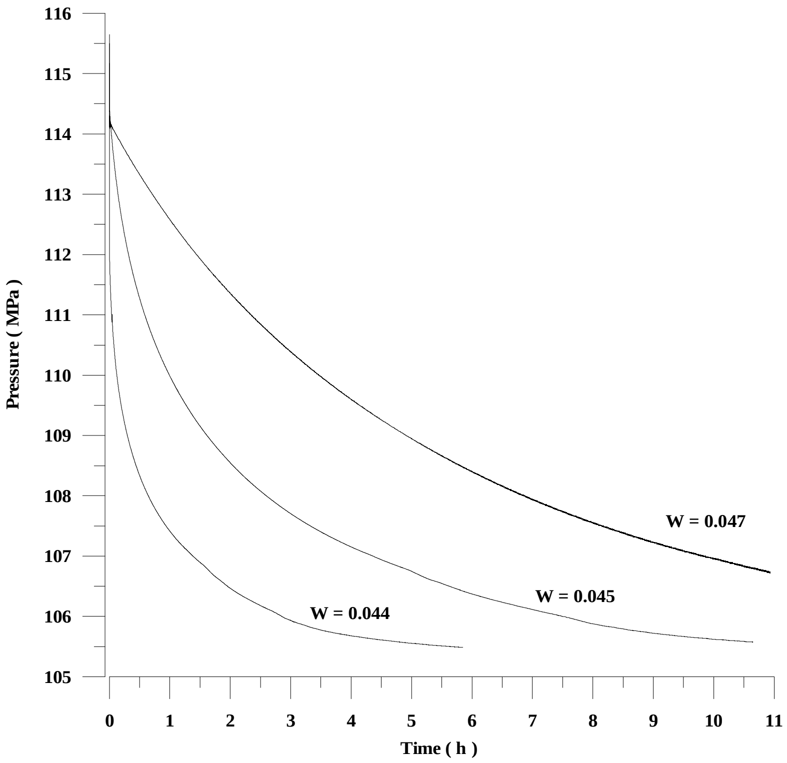

Figure 5.2.11. Eruption rate (top) and pressure at the conduit entrance (bottom) plotted versus time for the sill-like chamber with magma viscosity 10^5 Pa.s and considering three different water contents of 4.4, 4.5 and 4.7% in weight respectively.

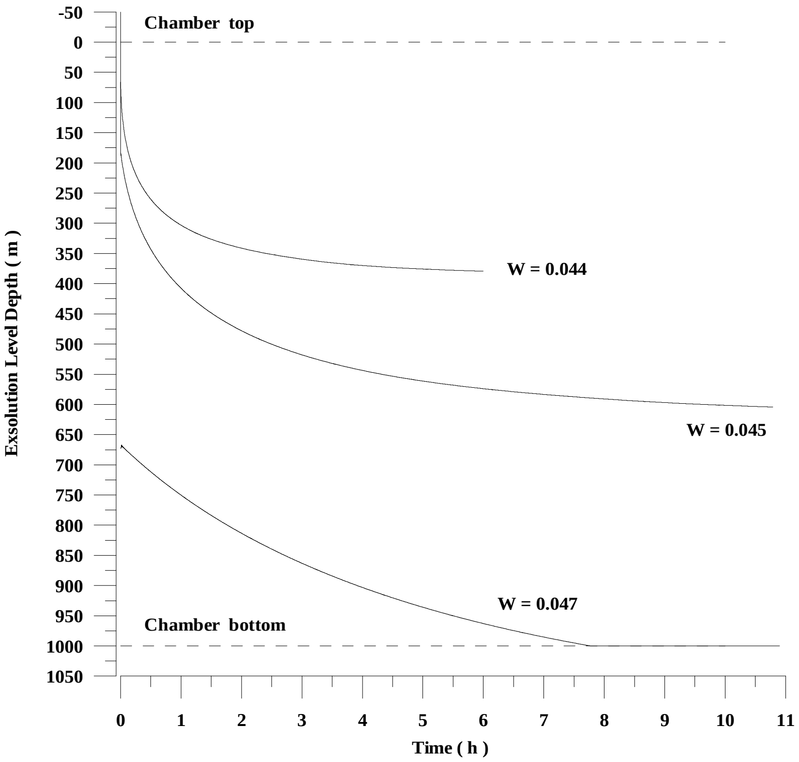

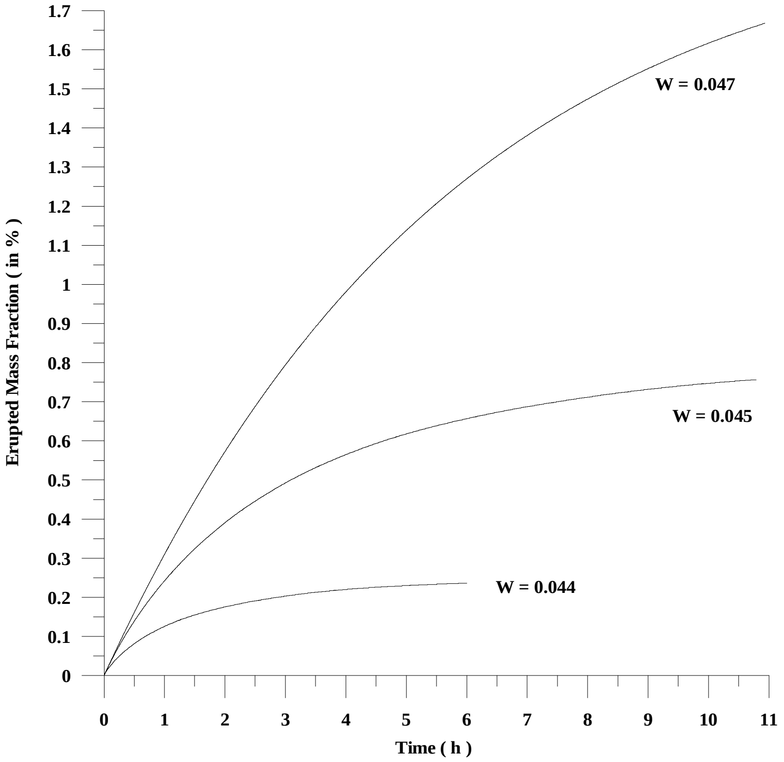

Figure 5.2.12. Position of the exsolution level (top) and erupted mass fraction (bottom) plotted versus time for the sill-like chamber with magma viscosity 10^5 Pa.s and considering three different water contents of 4.4, 4.5 and 4.7% in weight respectively.

Parameter	Effect on the **Eruption Rate**	Effect on the **Exsolution Level**	Effect on the **Erupted Mass**
Geometry (chambers with equal volume, at the same depth and filled with the same magma).	• Flattened chambers (sill-like) present a higher peak of intensity and a smoother eruption rate.	• Shifts more slowly in flattened (sill-like) cambers. • Initial and final positions do not depend on geometry.	• Flattened chambers (sill-like) erupt more mass since have a greater fraction of oversaturated magma.
Viscosity (magmas in the same chamber and having the same volatile content).	• More viscous magmas show a lower intensity peak and a smoother eruption rate.	• Shifts faster for less viscous magmas. • Initial and final positions do not depend on viscosity.	• Independent.
Volatile content (magmas in the same chamber and having the same viscosity).	• The higher the amount of volatiles the smoother the eruption rate.	• Shifts faster for lower volatile contents. • Initial and final positions depend on volatile content but the total shifting is not much sensitive to it.	• Chambers containing higher volatile content erupt more mass since have a greater fraction of oversaturated magma.

Table 5.2.1. Summary of the parametrical study. Some of the conclusions are intuitively expected and can be deduced from time-independent analytical models. However, numerical simulations allow to introduce also time dependencies.

5.2.2 Variable Volatile Content

The possibility of having a variable volatile content can also be contemplated. In this case, the Navier-Stokes equations must be complemented with the convective transport equation (4.2.1), the solution of which proportionates the volatile mass fraction W at each spatial point and for any time instant[1]. The initial value of the function W reflects the initial amount of volatiles inside the chamber. Note that the critical (exsolution) pressure p_c is still given by equation (3.2.8) but, since W is now variable, it must be computed at each numerical integration point every time that the use of the magma state law (3.2.13) is required.

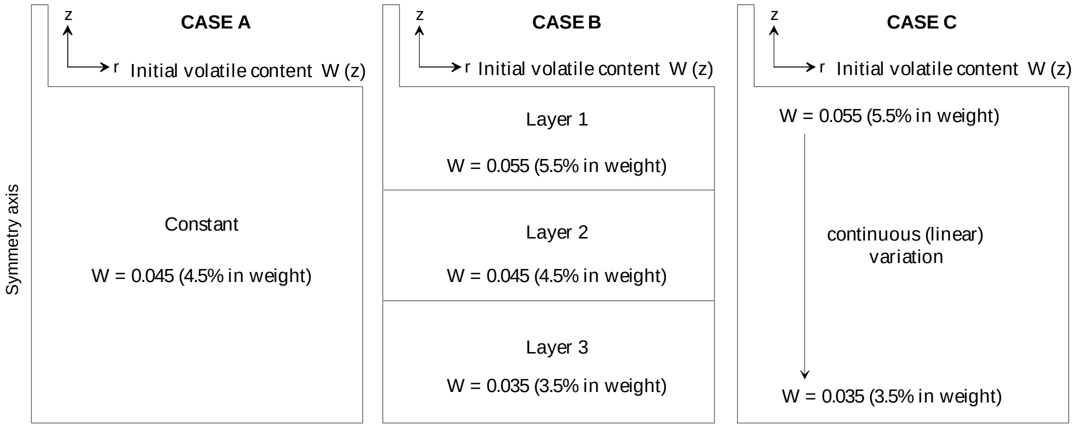

Figure 5.2.13. Initial distribution of volatiles for the cases A (constant volatile content), B (three layers) and C (linear variation). Whichever the case, the chamber is filled with rhyolitic magma with r_l= 2400 Kg/m^3 and viscosity μ=10^5 Pa.s.

Three different cases (named A, B and C respectively) are considered as example. These cases are illustrated in figure 5.2.13 and have the initial distribution of volatiles as follows: case A is the simulation already considered in section 5.2.1.1, i.e. a rhyolitic magma with a constant volatile content of $W = 0.045$ (4.5% in weight); case B is a three layered chamber with water contents of 5.5% (upper layer), 4.5% (middle layer) and 3.5% (lower layer) in weight respectively; and, finally, case C represents a chamber with a linear variation from 5.5% at the top of the chamber to 3.5% at the bottom[2]. The rest of parameters (density of the non-vesiculated magma, temperature, viscosity, etc.) are exactly the same in all the simulations.

---

[1] It can be shown that equation (4.2.1) for the mass fraction of volatiles W results from the imposition of mass conservation for the volatile species.

[2] Normally, the lower the amount of volatiles the higher the density of the magma. In consequence, buoyancy effects will tend to produce a pre-eruptive zonation from higher volatile mass fractions at the

Figure 5.2.14 plots the temporal variation of pressure at the entrance of the conduit and reflects how the process of decompression is rather similar in all the cases. The only appreciable discrepancy seems to be the value of the pressure at the entrance of the conduit once the final equilibrium has been established. Note that the pressure at the computational outlet is the same for all the cases (100MPa) but, in contrast, it differs at the entrance of the conduit (located 250m below the computational outlet) as a consequence of the different hydrostatic (magmastatic) loads resulting from the different density profiles (from the different volatile contents).

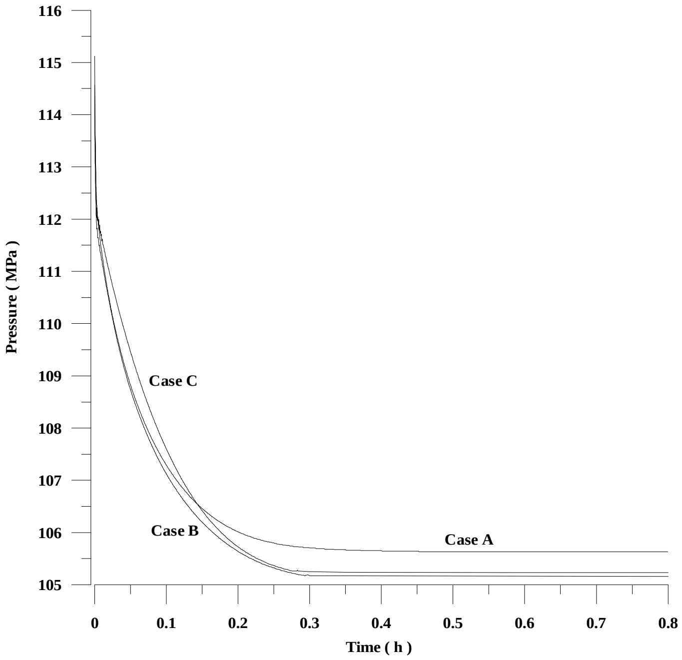

Figure 5.2.14. Pressure at the entrance of the conduit plotted versus time for the cases A (constant volatile content), B (three layers) and C (continuous stratification).

Figure 5.2.15 illustrates the initial and the final distributions of density inside the chamber as well as the position of the exsolution level. The initial depth of the exsolution level is 66, 333 and 445m for the cases A, B and C respectively (origin at the top of the chamber). In case A, the amount of volatiles (i.e. the exsolution pressure) is constant and, therefore, the position of the exsolution level shifts downwards only in response to the pressure variations which occur during the course of the eruption. In case B, the initial ambient conditions allow the upper layer (where $W = 0.055$) to be vesiculated but prevent the exsolution of volatiles within the intermediate and the lower layers (where $W = 0.045$ and $W = 0.035$, respectively). This initial distribution of volatiles produces a strong initial gradient in density at the interface between the upper and the intermediate layers. However, as the eruption proceeds, the

---

chamber top to lower volatile mass fractions at the bottom. The (unlikely) cases of reverse zonations are not contemplated here.

subsequent depressurisation of the chamber reduces the pressure in the intermediate layer below its critical value and, in consequence, part of the magma within this layer vesiculates and the exsolution level can shift downwards. The final position of the exsolution level is very similar to that obtained in case A. Finally, in case C, the exsolution level can shift only few meters because the linear decrease in the amount of volatiles almost compensates the effect of the depressurisation. The erupted mass fraction as well as the total erupted mass are depicted in figure 5.2.16.

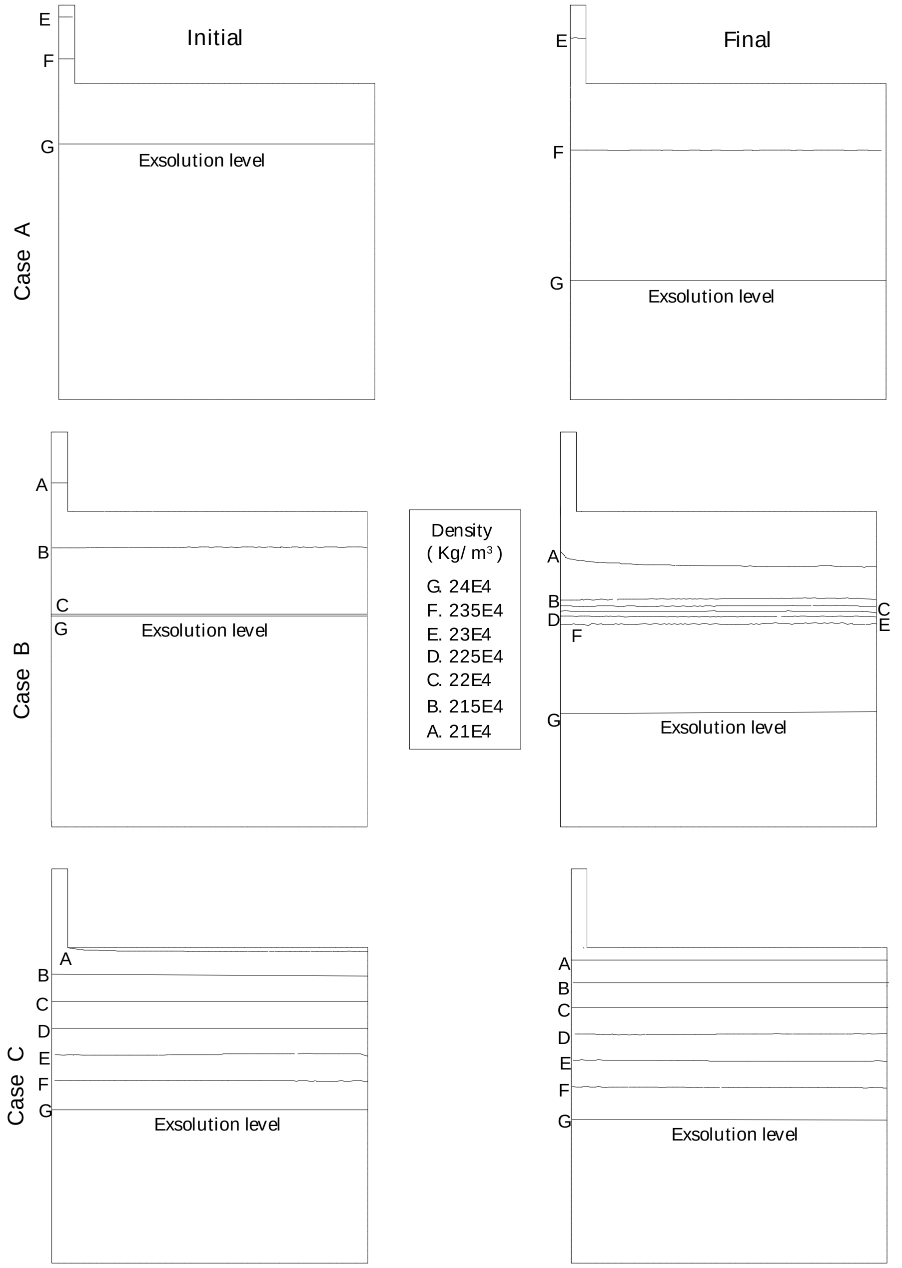

Figure 5.2.15 Initial and final distributions of density (in kg/m³) inside the chamber for the cases A (constant volatile content of 4.5% in weight), B (three layers with volatile contents of 5.5, 4.5 and 3.5% in weight) and C (continuous stratification in volatiles form 5.5% at the top

to 3.5% at the bottom). The position of the exsolution level, where $r=r_l$=2400 Kg/m^3, is also shown.

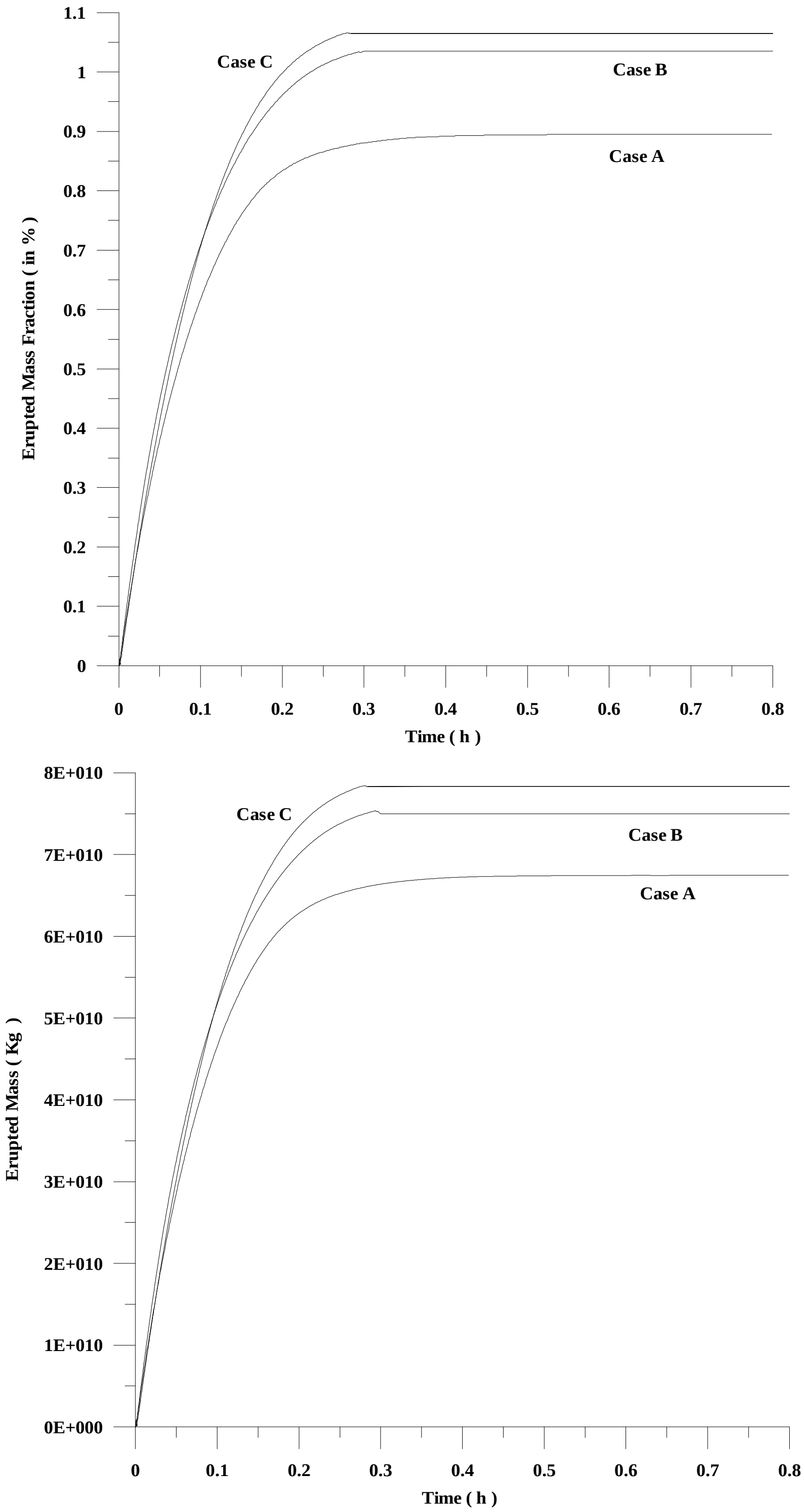

Figure 5.2.16. Erupted mass fraction (top) and total erupted mass (bottom) plotted versus time for the cases A, B and C respectively.

5.3 Withdrawal from Open Magma Chambers

This section presents some numerical examples concerning the withdrawal from open magma chambers (eruptions driven by magma replenishment).

5.3.1 Chemically Homogeneous Chambers

Consider first the simplest case of an eruption from a chemically homogeneous magma chamber triggered by injection of fresh magma having the same properties than the resident magma[1]. Two possible scenarios can be contemplated. The first, and the simplest, is that the host magma is not saturated in volatiles. Note that, in this case, the whole overpressure required to trigger the eruption must be induced by the injection itself. This situation was considered in [*Spera*, 1984] and its numerical simulation is "trivial" in the sense that involves only a single incompressible flow with uniform properties. The second possibility is more interesting and contemplates the possibility of having the host magma partially vesiculated prior to the injection. Note that, in this case, the chamber has some degree of pressurisation before the injection due to the previous presence of exsolved gas and that the effect of the injection –and secondary effect(s) associated to it- is just to bring the chamber to the critical condition of rupture.

As an example, consider the same case analysed in section 5.2.1.1 (cylindrical chamber with a lithostatic pressure at the outlet of 100MPa and a water content of 4.5% in weight) but now with an additional uniform vertical inflow velocity $\mathbf{u}_\mathrm{i}$ at the bottom face of the chamber. Figure 5.3.1 shows the evolution of the exsolution level and the pressure at the conduit entrance for three different inflow velocities of 1, 5 and 10 cm/s. These inflow velocities are arbitrary but characteristic of natural systems (e.g. [*Shaw*, 1985]). As observed from the figure, the initial overpressure decreases rapidly until it becomes stabilised to a steady value. The grater the inflow velocity, the higher the confining pressure associated to the injection and, in consequence, the lower the decrease in the chamber overpressure. Thus, for instance, for $|\mathbf{u}_\mathrm{i}| = 1\,\mathrm{cm/s}$ the decrease in pressure once the steady state has been reached is almost 10MPa while, in the case of $|\mathbf{u}_\mathrm{i}| = 10\,\mathrm{cm/s}$, is only 4MPa. Some degree of chamber depressurisation is always observed unless very high inflow velocities (physically unrealistic) are considered.

---

[1] It should be said that this situation is not very realistic, at least for explosive volcanism. Typically, magmas injected from the mantle (or lower crust) are of basic composition while the resident magmas are more chemically evolved. More realistic simulations involving two –or more- magmas of contrasted chemical (i.e. physical) properties are considered later, in section 5.3.2.

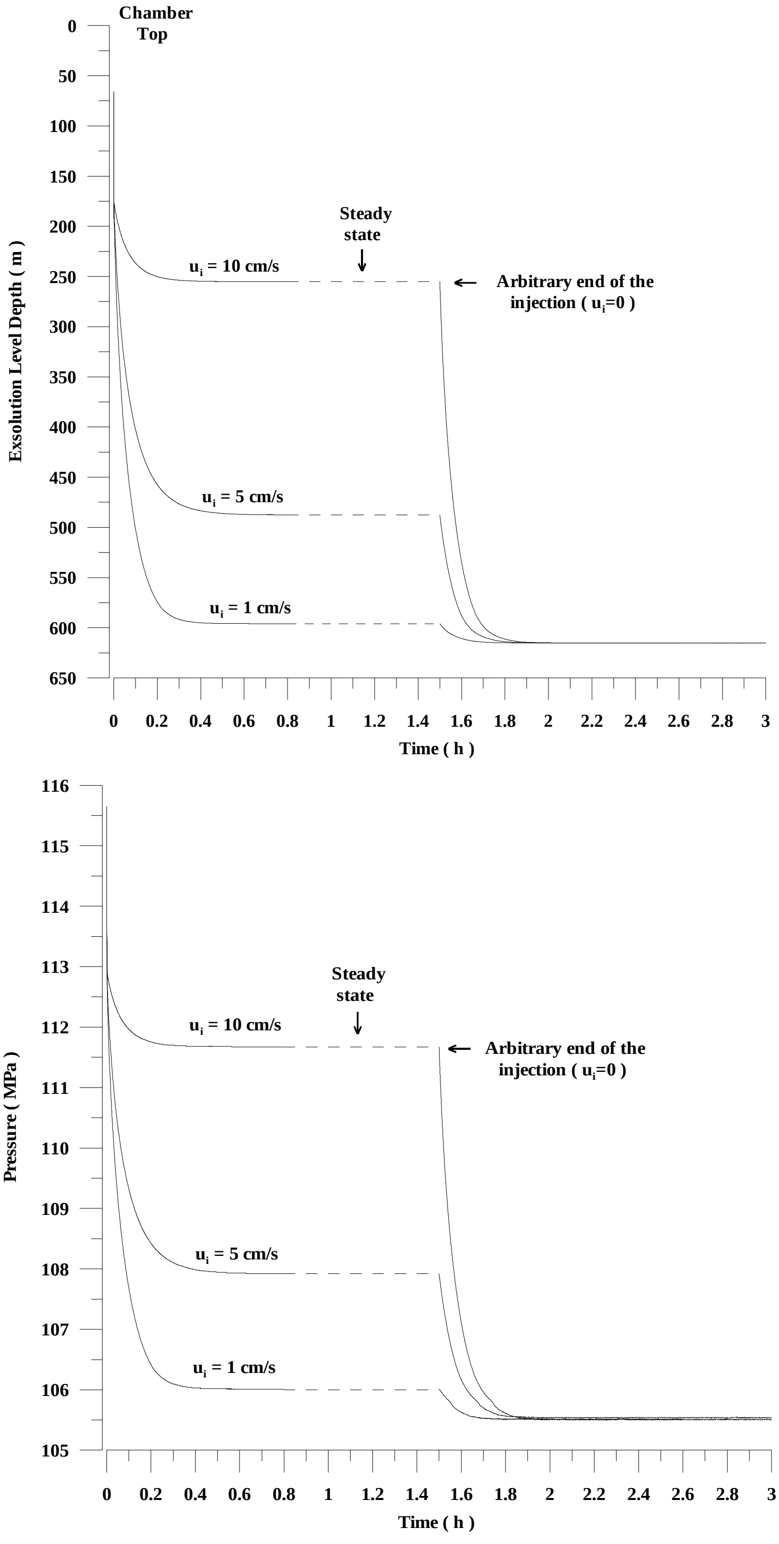

Figure 5.3.1. Position of the exsolution level (top) and pressure at the entrance of the conduit (bottom) plotted versus time for an open chamber with bottom inflow velocities of 1, 5 and 10 cm/s. In all the cases water content is 4.5% in weigh. The injection is switched off (arbitrarily) at *t* = 1.5 h, once the steady state has been reached. After the injection the evolution is analogous to that of a closed chamber with the same volatile content.

Obviously, the position of the exsolution level follows a similar trend: the greater the inflow velocity the lower the total shifting and the thickness of the upper oversaturated magma layer. This effect can be also observed from figure 5.3.2, which presents the streamlines and the density profile inside the chamber once the steady state has been achieved. The steady phase continues as long as the injection is maintained. In order to illustrate the final phases of the process, the inflow of magma has been arbitrarily switched off at *t* =1.5h[1]. After the injection the system evolves to a final situation analogous to that of the closed chamber.

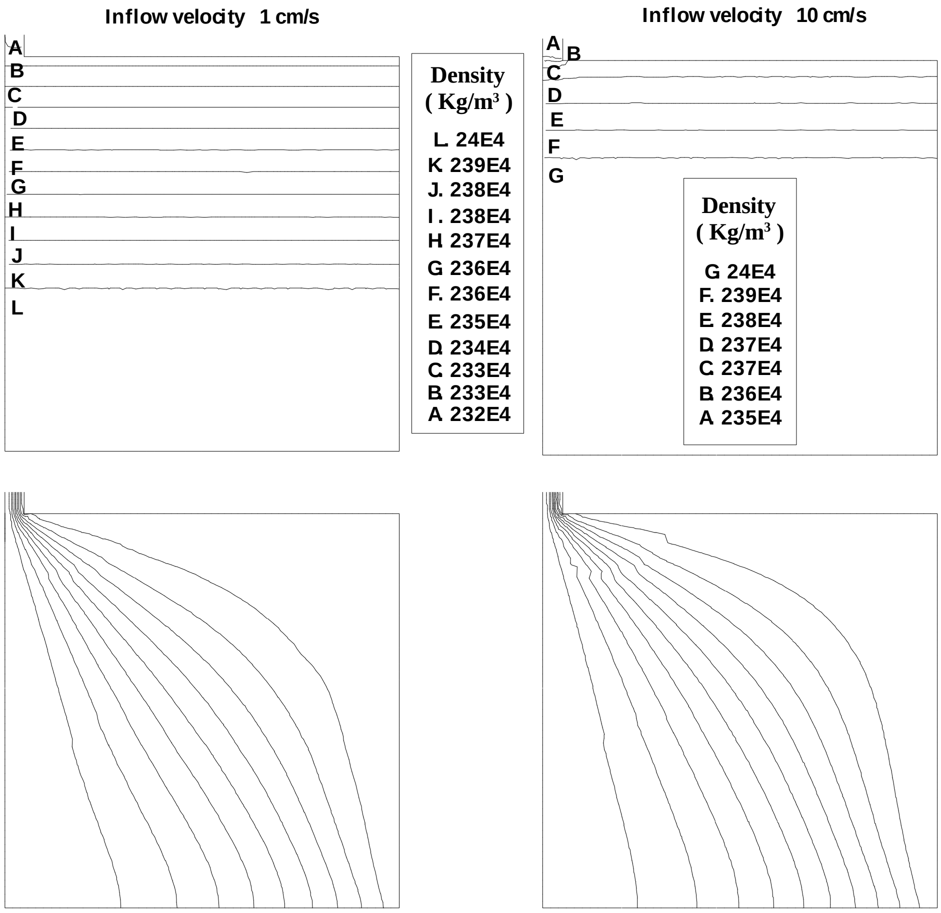

Figure 5.3.2. Density (Kg/m^3) and streamlines inside the chamber once the steady state has been reached for inflow velocities of 1 cm/s (left) and 10 cm/s (right). Water content is 4.5% in weight. An increase in the inflow velocity increases the confining pressure and shifts upwards the position of the exsolution level.

The evolution of the eruption rate is depicted in figure 5.3.3. It should be said that most of the eruptive intensity curves observed in historical explosive (Plinian) eruptions as well as those

---

[1] Remind that these examples aim to illustrate only a qualitative behaviour. A more physically realistic situation would probably show the same trends but in a much longer time-scale.

inferred from eruptive products, in the case of non-historical events, present eruption rates with a shape more similar to those of figure 5.3.3 than that of figure 5.2.4. This is an important result because might suggest that magmatic injection is probably the most common mechanism for triggering such eruptions. Figure 5.3.4 shows the total erupted mass and the erupted mass fraction and reflect that, during the stationary phase, the amount of extruded mass is proportional to time. Note that in open systems, and in contrast with the results obtained for closed chambers, the erupted mass fraction is not constrained. It implies that, even for small chambers, the amount of extruded material can grow indefinitely provided, of course, that the opening of the conduit and the inflow conditions are maintained.

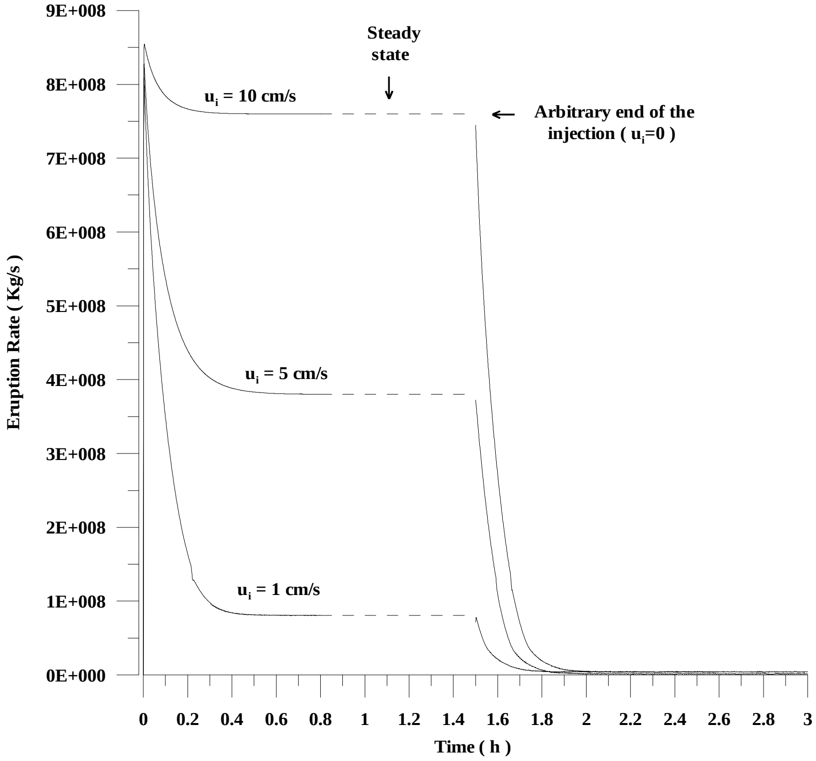

Figure 5.3.3. Eruption rate (Kg/s) versus time (in h) for an open chamber with bottom inflow velocities of 1, 5 and 10 cm/s. The injection is arbitrarily switched off at *t* = 1.5 h.

In the previous simulations, the amount of volatiles has been set to 4.5% in weight. In fact, and for these specific simulations of open chambers, this value should be regarded as an upper and “physically unnecessary” value. Any other lower value is, in principle, physically admissible. Thus, in this particular case, if $4.1\% \leq W \leq 4.4\%$ the chamber is totally non-vesiculated at *t*=0 but, as soon as the eruption starts, the pressure at the top of the chamber drops to the nucleation pressure. This is an isochore transformation of the magma without any generation of exsolved gas inside the chamber: during this “instantaneous” stage, no emission of mass occurs but just a sharp drop in pressure (and exsolution level).

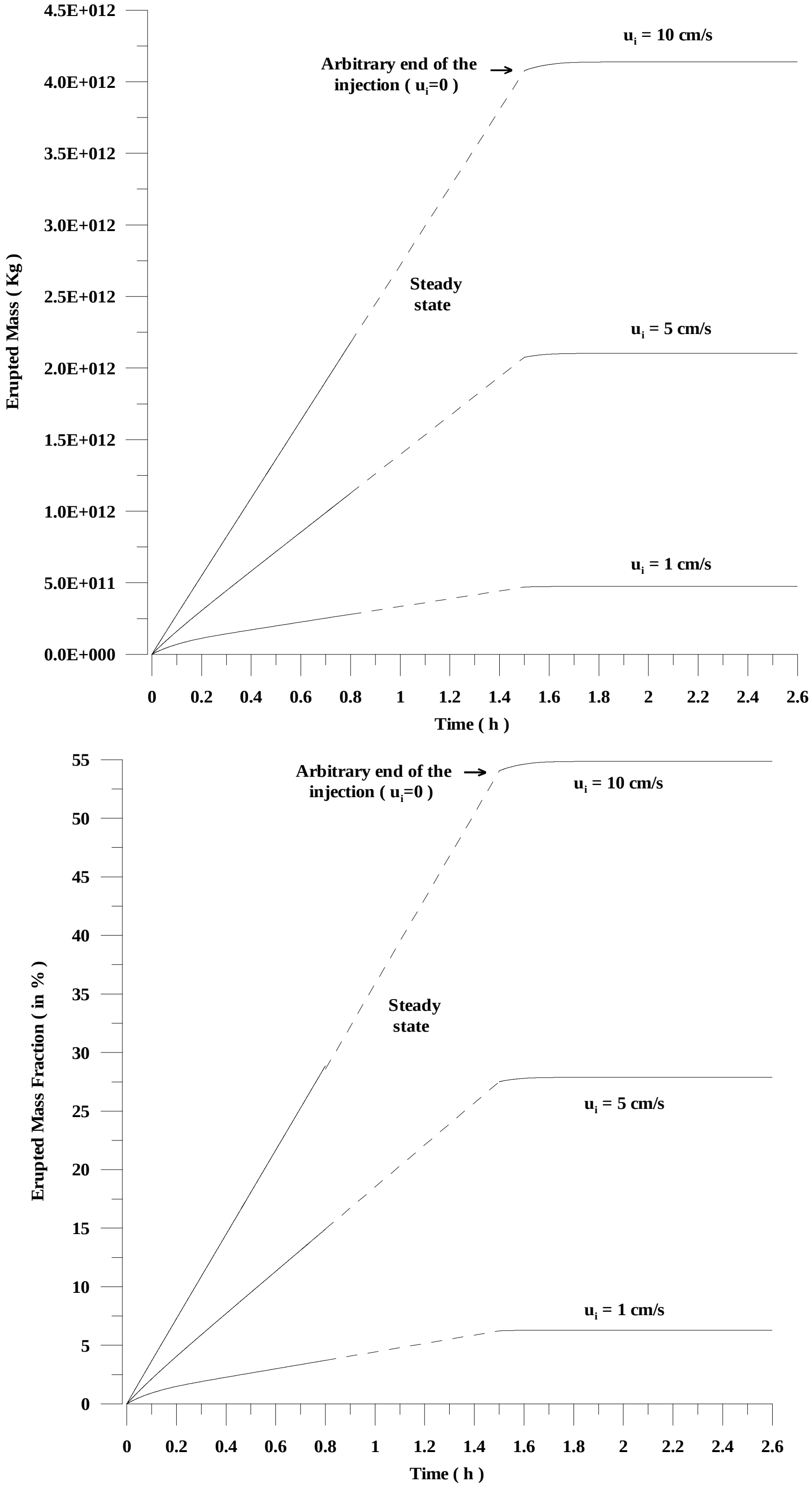

Figure 5.3.4. Total erupted mass and erupted mass fraction as a function of time for an open chamber with bottom inflow velocities of 1, 5 and 10 cm/s. Water content is 4.5% in weight and the injection is arbitrarily switched off at *t* = 1.5 h.

Once the chamber is vesiculated the system evolves as if $W \geq 4.4\%$ but, of course, the final position of the exsolution level depends on the specific value of W. This is illustrated in figure 5.3.5, where the position of the exsolution level for the cases $W = 4.5\%$ and $W = 4.35\%$ is plotted versus time. Finally, if $W \leq 4.1\%$, the computational domain (chamber and lowermost part of the conduit) never vesiculates. This case can perfectly be common in many natural eruptions but, as previously discussed, is not very interesting from a numerical point of view because the problem reduces to solve an incompressible flow with a given set of standard boundary conditions (velocity at inflow, pressure at outlet).

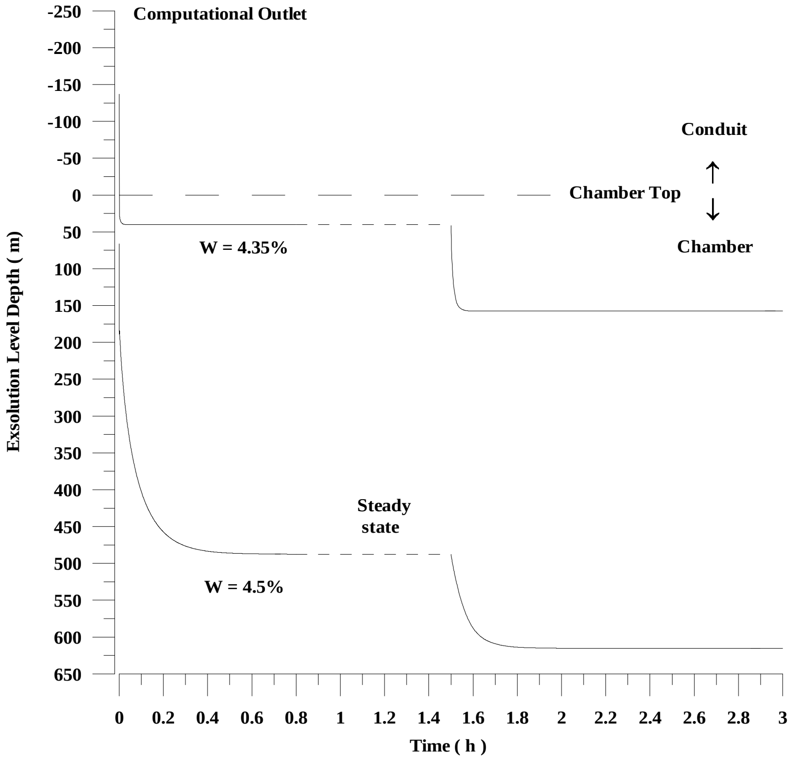

Figure 5.3.5. Exsolution level depth versus time for on open system considering an injection velocity of 5cm/s and two different volatile contents of 4.35 and 4.5% in weight. The injection is arbitrarily switched off at *t* = 1.5h.

5.3.2 Chemically Heterogeneous Chambers

The previous section has illustrated some examples of withdrawal from chemically homogeneous chambers during eruptions driven by magma replenishment. The assumption of chemical homogeneity simplifies notably the simulation of the process but, from a physical point of view, is rather unlikely[1]. This section considers a much more realistic example in which the injected magma (a basalt) has physical properties which markedly differ from those of the resident magma(s). The problem has been already faced in [*Greer*, 1986; *Spera et al.*, 1986; *Trial et al.*, 1992] and, for this reason, will not be treated here in detail. To deal with chemical heterogeneities it is commonly assumed that physical properties (density and viscosity) are functions of the composition field C ($\in [0,1]$)

$$\begin{aligned} r &= C r_2 + (1-C) r_1 \\ m &= C m_2 + (1-C) m_1 \end{aligned} \tag{5.3.1}$$

where C represents the volume fraction of the component 2 which, in our case, is the injected basaltic magma. This procedure allows to reproduce any initial compositional profile inside the chamber (e.g. two-layered, three-layered, continuos, etc.) between two extreme members named 1, with properties r_1 and m_1, and 2, with properties r_2 and m_2. The physical meaning ascribed to the compositional field C is the averaged composition of a magma parcel and, if chemical diffusion is neglected, it is solution of the purely convective transport equation (4.2.1) which must be solved together with the Navier-Stokes equations[2]. The compositional transport problem is well posed when C is prescribed (to 1 in our case) at the inflow part of the domain (see figure 5.3.6). The rest of boundary and initial conditions do not vary with respect to the homogeneous case.

The interest of these simulations is mainly to characterise the temporal evolution of the composition of the magma reservoir as well as to analyse how the dynamics of the magma withdrawal process may affect the geochemistry of the resulting volcanic deposits. For this purpose it is interesting to determine the averaged magma composition at the conduit entrance $\overline{C}$ by computing the integral

---

[1] In fact, many mineralogical and geochemical studies of volcanic deposits point out that, in most of the cases, chemical heterogeneities exist within the chamber.

[2] Note that, in practise, the problem is analogous to the filling of a mould. The compositional function plays the role of the pseudo-concentration function.

$$\overline{C} = \frac{\oint C\,dS}{\oint dS} = \frac{2}{r_c^2}\int_0^{r_c} C\,r\,dr \tag{5.3.2}$$

over the conduit (the above expression assumes axial symmetry and a vertical conduit of radius r_c). This averaged quantity can be measured from stratigraphic sections of any volcanic deposit using geochemical techniques. However, it should be noted that the relation between the averaged composition of a magma parcel at the entrance of the conduit $\overline{C}$ and that of the final deposit is not straightforward at all. Different processes that occur within the conduit as well as the own dynamics of the subaerial transport and subsequent emplacement of these volcanic products are likely to produce considerable variations in the averaged composition of the final deposits. It means that the results inferred here should be regarded only as a rough guide.

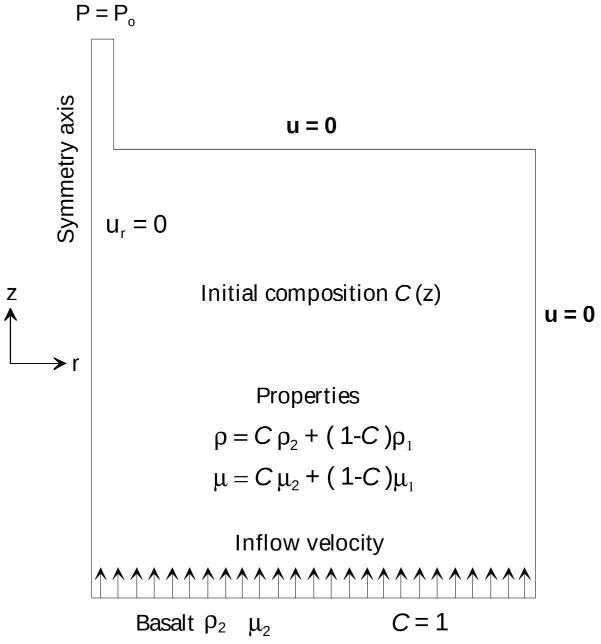

Figure 5.3.6. Boundary conditions. A basic magma is injected with a uniform inflow velocity into a cylindrical chamber containing more evolved magma (rhyolite). The compositional variable C represents the volume fraction of basalt and, in consequence, is prescribed to 1 at the bottom of the chamber (inflow). The initial composition of the chamber is characterised by the function C(z).

Consider first the example of an eruption triggered by the injection of a basalt with density $\rho_2 = 2800\,\mathrm{Kg/m^3}$ and viscosity $\mu_2 = 10^3$ Pa.s into an initially homogeneous cylindrical chamber (same geometry than in the previous section, lithostatic pressure of 100MPa at the computational outlet) filled with an evolved magma (rhyolite) having density $\rho_1 = 2400\,\mathrm{Kg/m^3}$ and viscosity $\mu_1 = 10^5$ Pa.s. Kinematic viscosities of both magmas are, in consequence,

$u_1 = 0.024$ and $u_2 = 2.8$. The inflow velocity is uniform, vertically upwards, and has a value of 10cm/s. The mass flow rate at the inflow ($r_2 \, |\mathbf{u}_\mathbf{i}| \, p \, a^2$) is 8.8×10^8 Kg/s. For simplicity it is assumed that the evolved resident magma is undersaturated in volatiles and, in consequence, both magmas can be regarded as incompressible flows. Initially, the compositional function C is a step function ($C = 1$ at the inflow, $C = 0$ on the rest of the domain). Figure 5.3.7 shows the position of the rhyolite-basalt interface ($C = 0.5$) at different time instants.

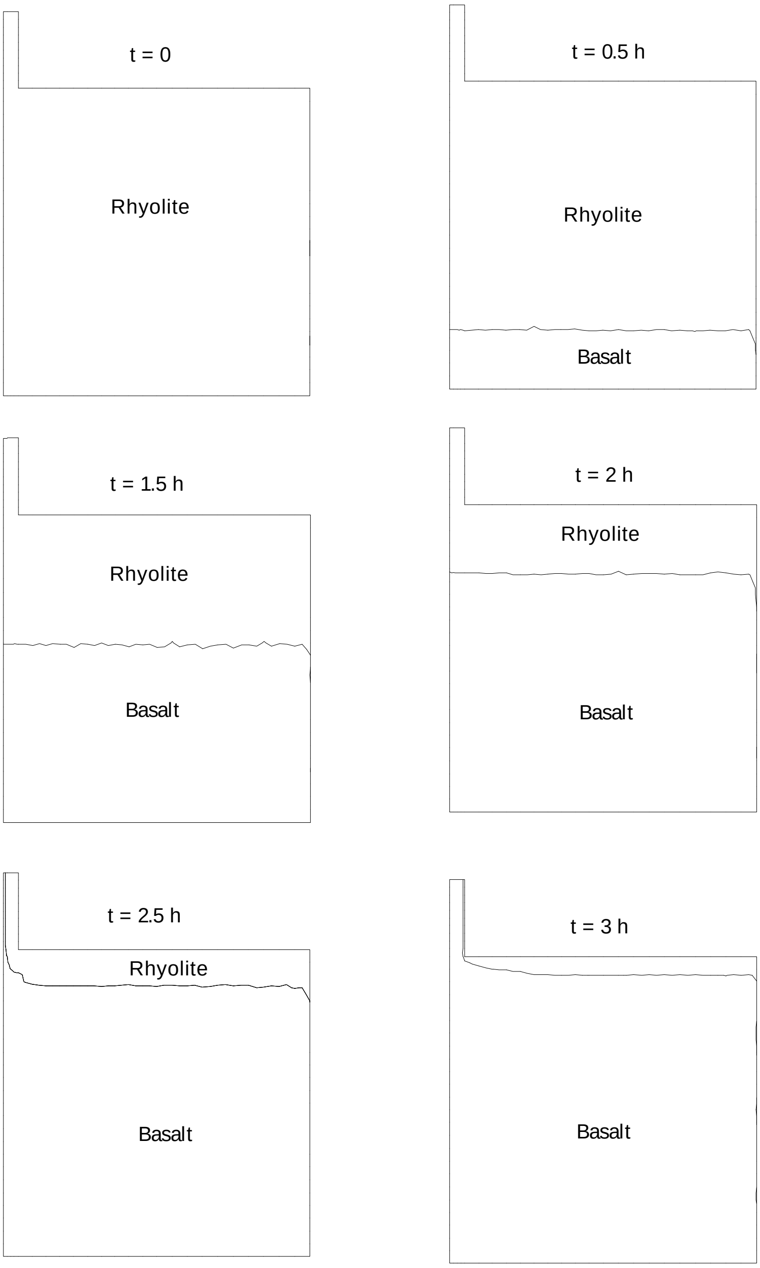

Figure 5.3.7. Position of the rhyolite-basalt interface (*C*=0.5) at different time instants. Note how at *t* = 2.5 h both layers begin to be simultaneously erupted.

As the eruption proceeds, the basalt-rhyolite interface is horizontally shifted and, due to its higher density, the basaltic layer remains at the bottom of the chamber. However, once the upper rhyolitic layer becomes thinner than some critical depth the interface tilts and both magmas are erupted simultaneously. In this particular example it occurs at approximately *t*=2.5h. The eruption enters then into a phase of mingling during which the erupted products progressively evolve from a pure rhyolitic composition to a purely basaltic (see figure 5.3.8). After this period of mingling (at approximately *t* = 3h) only basalt is erupted. Some residual rhyolitic magma is, however, left in the uppermost part of the chamber. The possibility of simultaneous eruption was already predicted in a series of laboratory experiments [*Blake and Ivey*, 1986a; *Blake and Ivey*, 1986b; *Blake and Fink*, 1987]. Working with experimental tanks containing two glycerol solutions with different kinematic viscosities, the authors investigated the conditions under which buoyancy force is overcome, allowing the more dense lower fluid to be drawn into the outlet. They came out with the conclusion that there exists a minimum thickness for the upper lighter layer required to prevent the withdrawal of the lower denser layer. In other words, if the upper layer is thinner than some critical depth, both layers are simultaneously erupted. Extrapolating these experimental results to magmas, the authors predicted draw-up depths in the range of 100m. This is in good agreement with the results obtained in the numerical simulations.

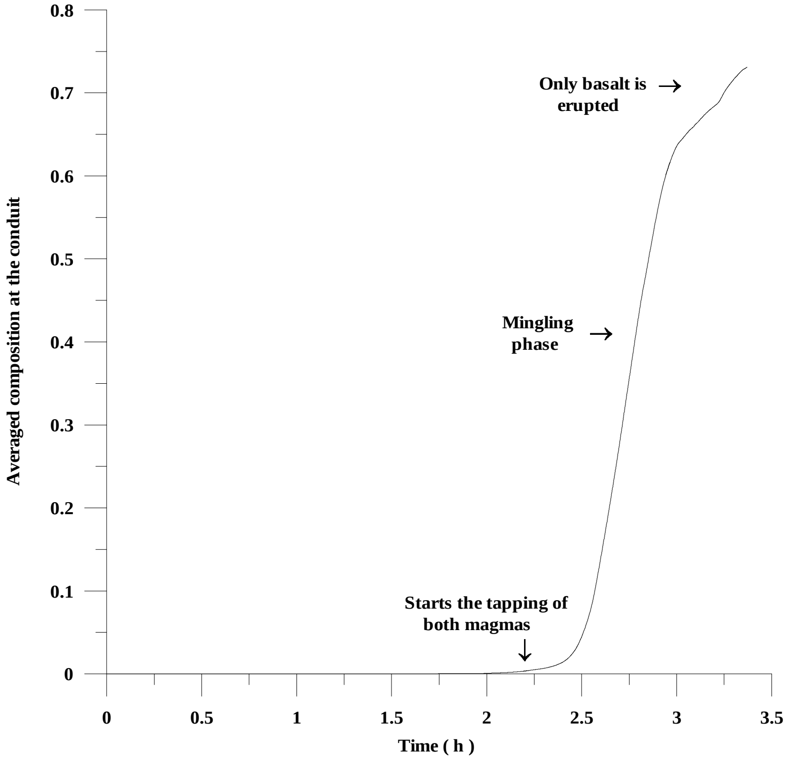

Figure 5.3.8. Averaged value of *C* at the entrance of the conduit plotted versus time. The values *C*=0 and *C*=1 correspond, respectively, to pure rhyolite and basalt compositions.

Observation The eruptive process may finish at any stage if the injection is switched off or if the conditions for conduit closure are achieved. If it would happen before the mingling phase there would not be neither mineralogical nor geochemical evidences of the triggering mechanism (magma injection) in the resulting deposits. In consequence, the non-existence of mingling in the volcanic products does not necessarily imply an eruption triggered by volatile oversaturation (closed system) from a chemically homogeneous chamber. Note also that the basic magma would remain initially at the bottom of the chamber where it would cool and crystallise. Chemical diffusion, overturning of the mafic layer [*Huppert et al.*, 1982; *Turner and Campbell*, 1986] or convective entrainment due to viscous coupling [*Snyder and Tait*, 1996] may lead to large-scale magma mixing. It implies that, if new injections or further exsolution of volatiles due to fractional crystallization in the felsic magma are, after some period of time, able to trigger a new eruption, the observed mixed products may correspond to previous replenishment events.

To illustrate the differences between several initial chemical compositions of the chamber three different initial functions C have been considered (see figure 5.3.9).

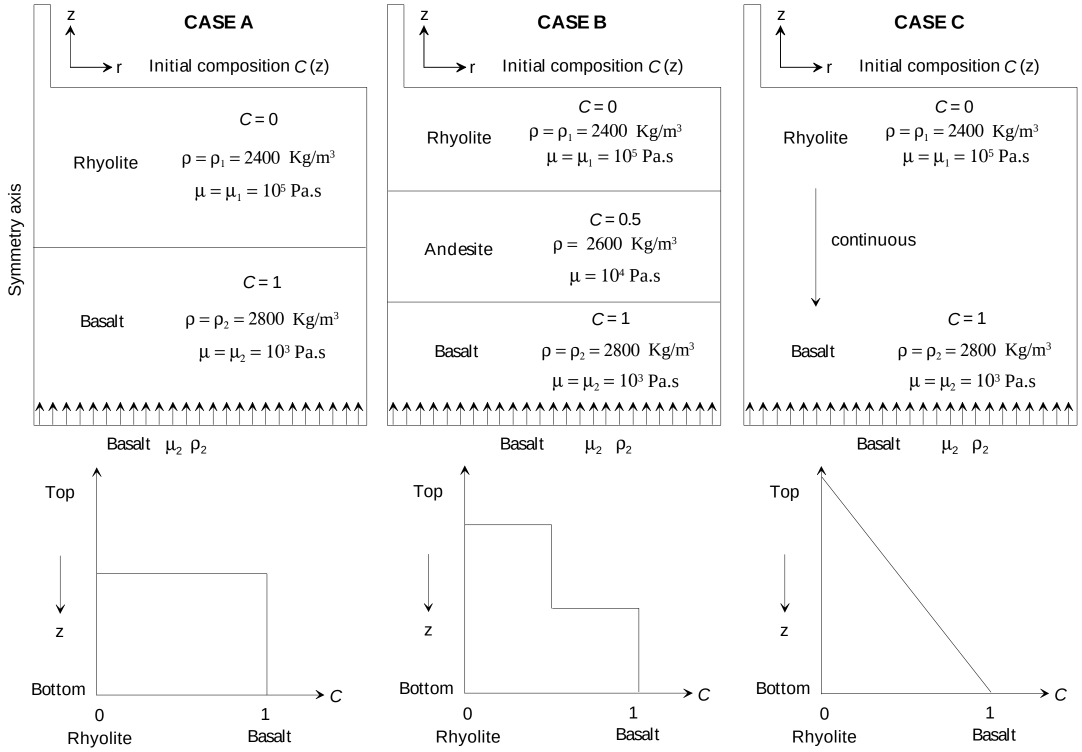

Figure 5.3.9. Initial value of the compositional function for the cases A (two discontinuous layers), B (three discontinuous layers) and C (continuous stratification).

Case A is a two layered system in which the upper half of the chamber contains rhyolite and the lower half basalt. Case B is a three layered system with $C = 0.5$ in the middle layer (its physical properties are $r = 2600\,\mathrm{Kg/m^3}$ and $m = 10^4$ Pa.s which approximately correspond to a magma of intermediate composition such as, for instance, an andesite). Finally, case C reflects a continuous stratified composition ranging from a rhyolite at the top to a basalt at the bottom.

Figure 5.3.10 illustrates how the averaged composition of the extruded material evolves with time and points out the possibility (already suggested in [*Spera et al.*, 1986]) of distinguishing, at least theoretically, between the different initial distributions by accurate volcanological sampling. Figure 5.3.11 shows how the composition of the chamber evolves with time. The main conclusion is that the same trends observed in the case of an initially homogeneous chamber (horizontal displacement of the interfaces and posterior tilt and simultaneous eruption of magmas once a critical thickness is reached) are observed now for the different layers.

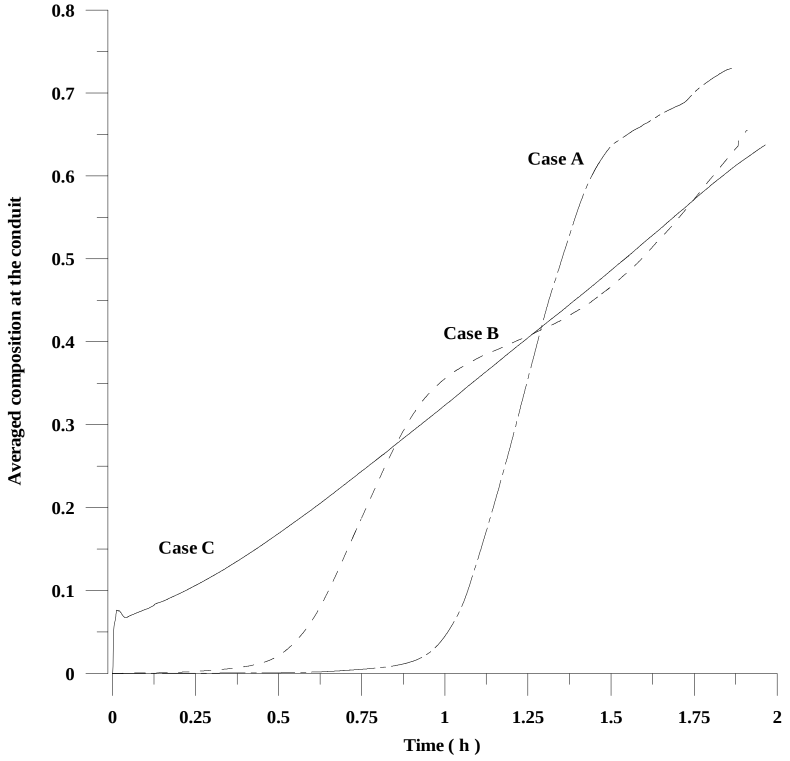

Figure 5.3.10. Averaged value of C at the entrance of the conduit plotted versus time for the cases A (two-layered chamber), B (three-layered chamber) and C (continuous stratification). The values *C*=0 and *C*=1 correspond, respectively, to rhyolitic and basaltic compositions.

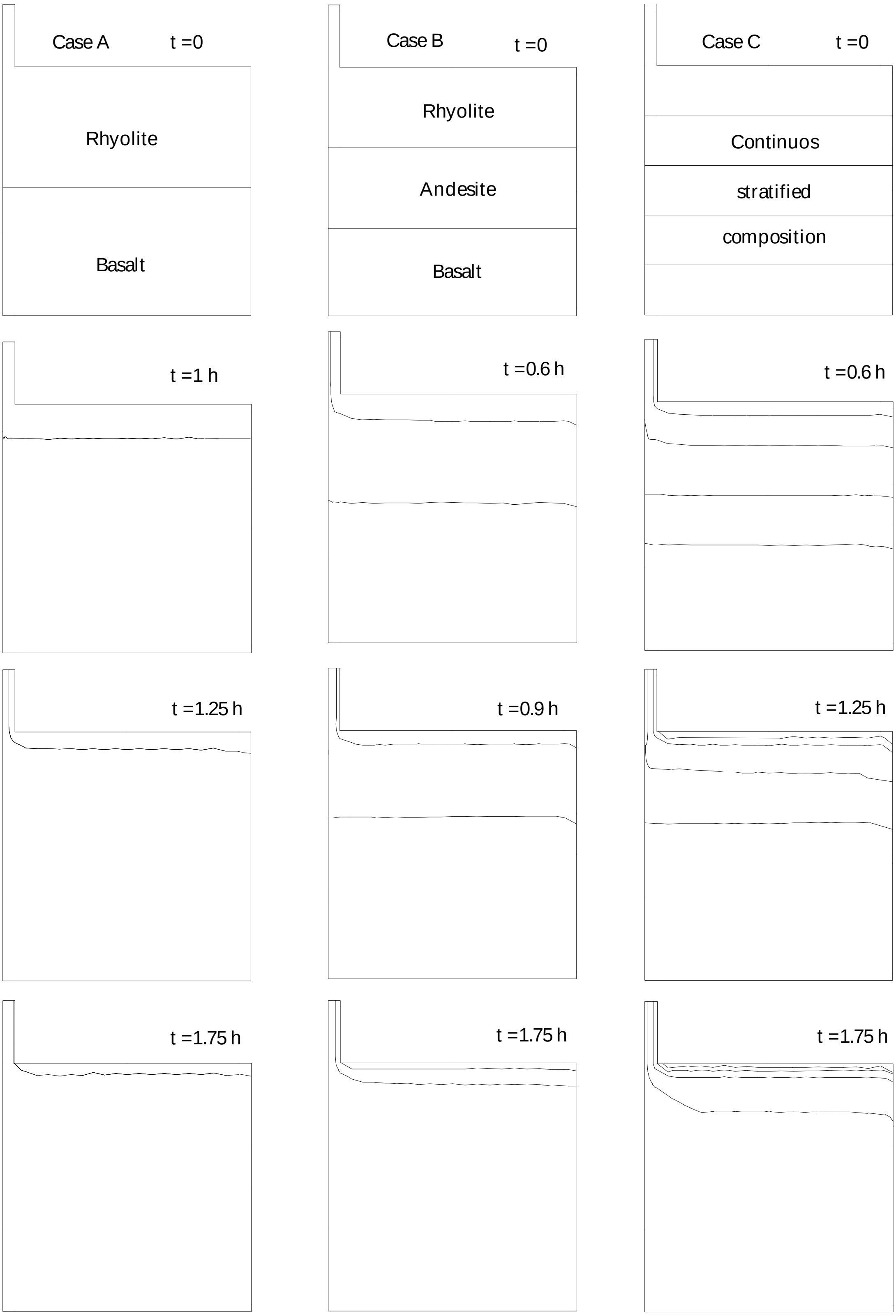

Figure 5.3.11. Composition of the chamber at different time instants for the cases A (left column), B (central column) and C (right column).

5.4 Caldera-Forming Eruptions

This section presents some numerical examples concerning caldera-forming eruptions[1]. The reader is referred to section 2.3.3 for major details concerning to this kind of eruptions. Boundary and initial conditions are illustrated in figure 5.1.3. In the examples it is assumed that the eruption starts once the ring fault is already open[2] and that the subsiding block behaves as a coherent rigid solid (i.e. without holding deformations or splitting into secondary blocks). The driving mechanism of the eruption is the density contrast between the magma and the block (i.e. the pressure differences), which induces the movement of the block downwards and squeezes magma out of the chamber through the ring fault. Two different magma chamber geometries (elliptical and cylindrical) are contemplated in the examples. In both cases, the chambers have an horizontal extension $a = 4\text{Km}$, a vertical extension $b = 0.5\text{Km}$, are located at depth $H_{cha} = 4\text{Km}$ below the surface of the Earth, the ring fault is placed at a distance $a_c = 3.5\text{Km}$ from the symmetry axis and the volcanic conduit has a thickness of $r_c = 50\text{m}$. Figure 5.4.1 summarises the geometrical properties.

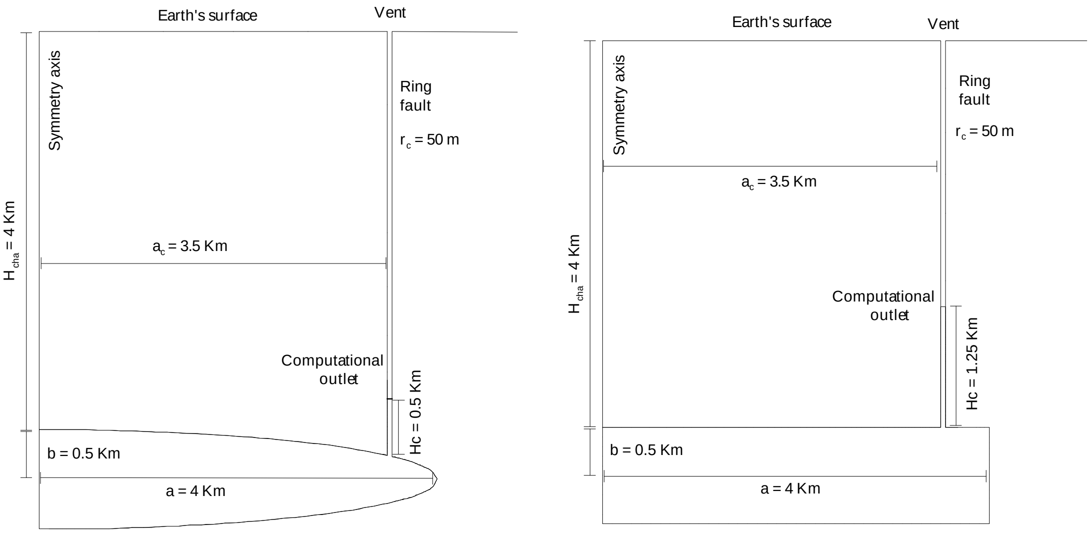

Figure 5.4.1. Geometries at the onset of the eruption for the elliptical and the cylindrical chambers.

---

[1] The only previous attempt to model such kind of eruptions can be found in [*Spera*, 1984], where the process is modelled in a 2D domain, considering that magma beheaves as an incompressible flow and without mechanical coupling, that is, imposing the velocity of subsidence of the block arbitrarily.

[2] Typically, a caldera-forming eruption is preceded by a central vent eruption which decompresses the magma chamber and, under certain favourable conditions, allows the formation of ring faults and, eventually, the closure of the primary central fissure [*Martí et al.*, 2000]. In consequence, these eruptions are the culmination of previous complex processes which are neglected in the numerical simulations, partly to simplify the problem and partly because are not well determined yet.

Again, geometries and magma properties considered are arbitrary but perfectly compatible with natural cases[1]. The mean density of the host rock is assumed to be $r_r = 2600 \text{Kg/m}^3$ (implying masses for the subsiding blocks of $4.11 \times 10^{14}\,\text{Kg}$ and $4.00 \times 10^{14}\,\text{Kg}$ for the elliptical and the cylindrical geometries respectively), whereas the non-vesiculated magma has a density $r_l = 2400 \text{Kg/m}^3$ and a viscosity $m = 10^4\,\text{Pa.s}$.

<u>Observation</u> Only "explosive" caldera-forming eruptions (associated to evolved magmas) are simulated here. However, calderas can also result from lateral migration of magma and, in consequence, can be produced without the extrusion of magma through the ring faults. This second possibility, normally associated to magmas of more primitive compositions (basalts), is not considered in this thesis.

Modelling of caldera-forming eruptions involves the solution of a fluid-structure interaction problem in which the fluid (magma) can be either incompressible (when non-vesiculated) or compressible (when vesiculated). The general procedure and the staggered algorithm proposed here to solve such kind of problems have already been widely discussed in section 4.3. Three different meshes (fluid, block and background) are required in the simulations. The (moveable) mesh of the fluid is used to solve the ALE Navier-Stokes equations while the other two, which do not vary and can be as coarse as desired, are auxiliary. The mesh of the fluid is considered to be unacceptable when any of its linear triangular elements has an angle lower than 10° or greater than 160°. Every time that this critical condition of distortion is attained a new mesh is automatically generated by the program and the interpolation of nodal variables onto the new mesh is performed. The mesh of the block defines its geometry and, obviously, moves with a velocity $\mathbf{u_b}$. This mesh is used every time that a remeshing is performed to check whether a node of the new generated mesh of the fluid belongs to the fluid/structure interface or not. Finally, the purpose of the fixed background mesh is just to check whether the points of the structure belong to some element of the background mesh in order to detect shocks of the block against the walls of the chamber and, in consequence, to determine the end of the simulation.

---

[1] Recent studies [*Gudmundsson et al.*, 1997; *Gudmundsson*, 1998] on stress field generating ring faults in volcanoes have suggested that horizontally elongated (sill-like) chambers offer the most suitable stress configuration for the initiation of ring faults. The geometries considered here have an horizontal to vertical aspect ratio in agreement with those suggested by these previous studies.

5.4.1 Non-Vesiculated Magma

Consider first, as a first approach, the simplest case in which the magma within the chamber is non-vesiculated and, therefore, behaves as an incompressible fluid[1]. Results for the elliptical chamber are shown in figures 5.4.2 to 5.4.7. The whole simulation requires up to 6 different meshes for the fluid (i.e. 5 remeshings). Figure 5.4.2 illustrates the different domains (fluid, block and background) as well as its meshes at three different time instants. Figure 5.4.3 shows views of 5 different meshes for the fluid. Figures 5.4.4 to 5.4.6 present some numerical results (pressure contours, streamlines, contours of mesh velocity norm and contours of velocity norm) at different time instants. A characteristic feature of the process is that, as the eruption proceeds, a big central vortex (and secondary small ones) develops at the outermost part of the chamber, just below the entrance of the conduit. This phenomena is illustrated in figure 5.4.7. The vortex is formed because the non-slip condition at the fluid/structure interface induces a tangential slide[2]. Results for the cylindrical chamber are qualitatively equal to those of the elliptical one and are presented in figures 5.4.8 to 5.4.13. In this case, the simulation requires 9 different meshes for the fluid (i.e. 8 remeshings).

Figure 5.4.14 shows the subsidence of the block and the eruption rate plotted versus time. As soon as the caldera collapse starts, the velocity of the subsiding block increases rapidly downwards due to buoyancy effects. However, viscous forces and as well as the pressure exerted by the magma over the block rapidly compensate the density differences and, in consequence, the net force acting over the block becomes nearly zero. The result is that the block subsides at an approximately constant "terminal" velocity[3]. In the particular cases considered, these "nearly steady" velocities are 0.55 m/s for the elliptic geometry and 0.7 m/s for the cylindrical one. The nearly constant velocity of subsidence is maintained during most of the eruptive process and only ceases during the last phase of the eruption, when the block begins to stop before shocking against the walls of the chamber. A consequence of this kinematic behaviour is that the eruption rate presents a rapid increase, a plateau which corresponds to the "constant fall velocity" phase and, finally, a relatively sudden decrease. This numerical prediction is in excellent qualitative agreement with the eruptive intensities observed (or indirectly inferred) during caldera-forming eruptions.

---

[1] The much more realistic situation in which part of the magma chamber is vesiculated at the onset of the collapse (or vesiculates during it) is considered later, in section 5.4.2. However, note that the absence of gas within the chamber does not necessarily imply that the caldera-forming eruption is non-explosive.

[2] Note the similarities with the driven cavity flow. See section 4.4.1.

[3] The kinematic behaviour is, in fact, quite similar to that of the Stokes problem. See section 4.4.5.

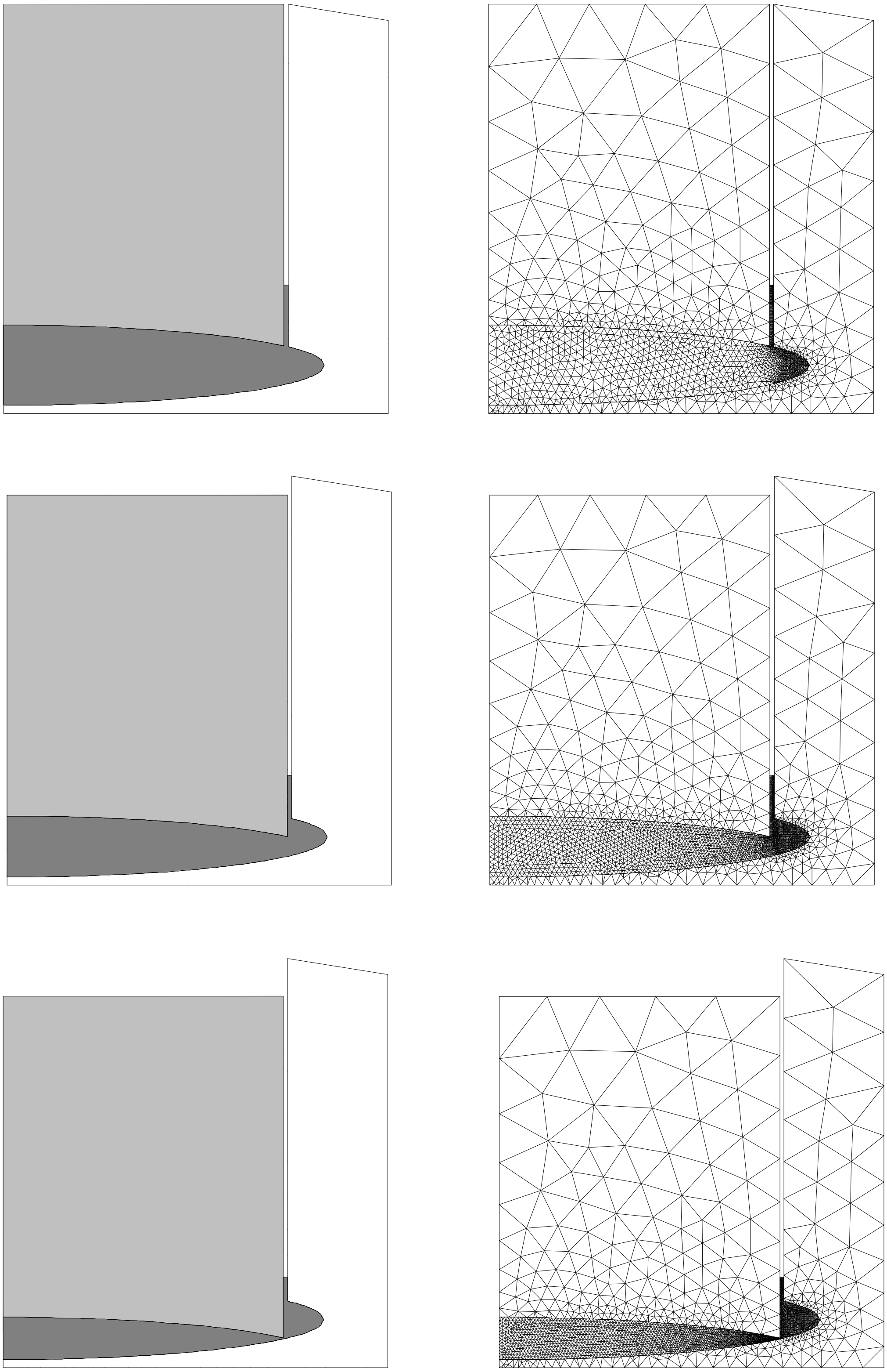

Figure 5.4.2. Geometry and space discretisation for the elliptical chamber at three different time instants. Left column: illustration of the different domains: fluid (dark grey), block (grey) and background (white). Right column: space discretisations (3 different non-matching meshes at any time instant). The corresponding time instants are, form top to bottom, *t*=0, *t*= 8min and *t*=16min.

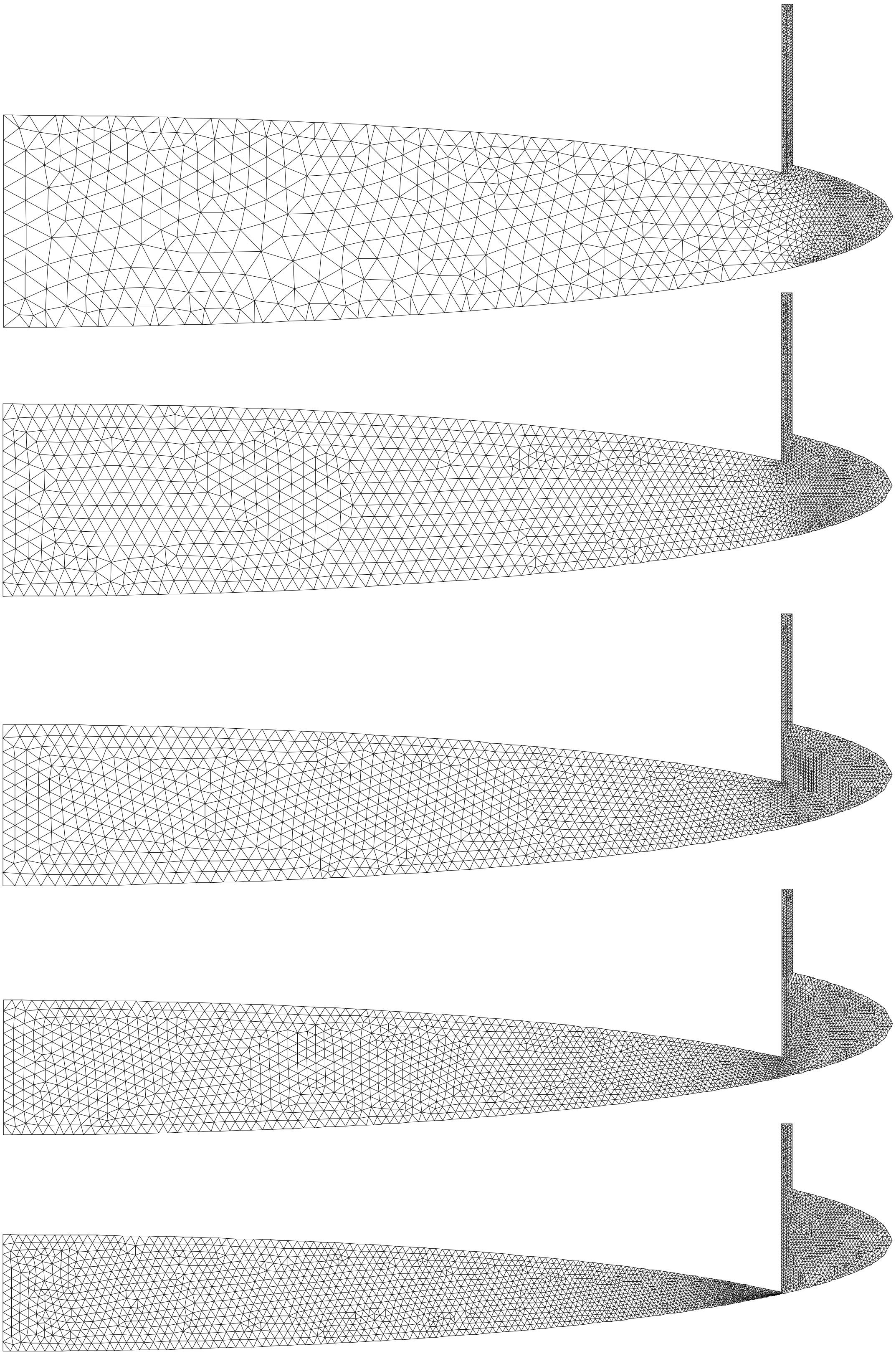

Figure 5.4.3. From top to bottom: views of the fluid's meshes 1, 2, 3, 4 and 6. The corresponding time instants at which these meshed are generated are t=0, t=4.5min, t=8min, t=11min and t=16min respectively.

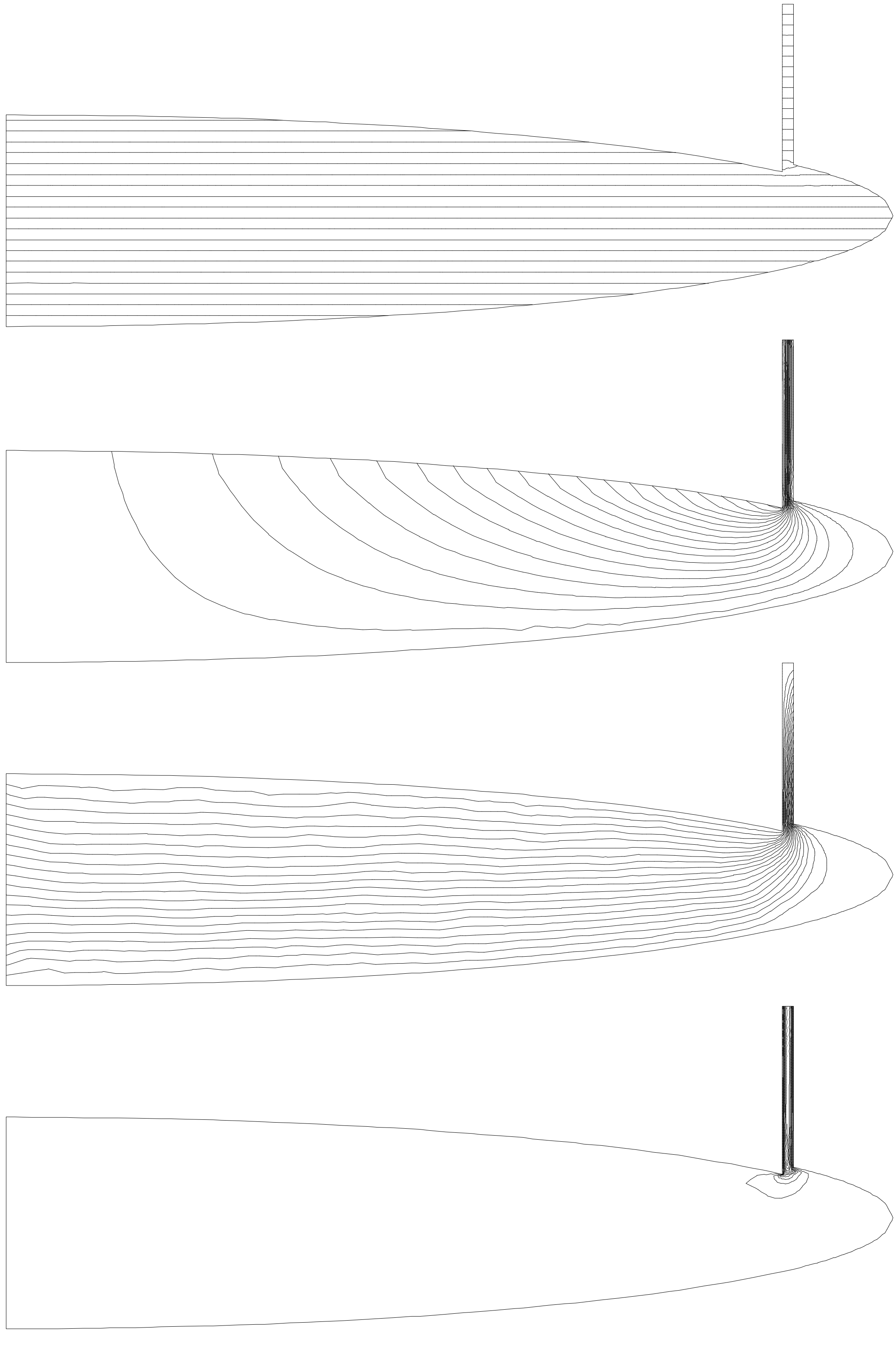

Figure 5.4.4. Numerical results at *t*= 2min. Results shown are, form top to bottom, pressure contours, streamlines, contours of mesh velocity norm and contours of velocity norm.

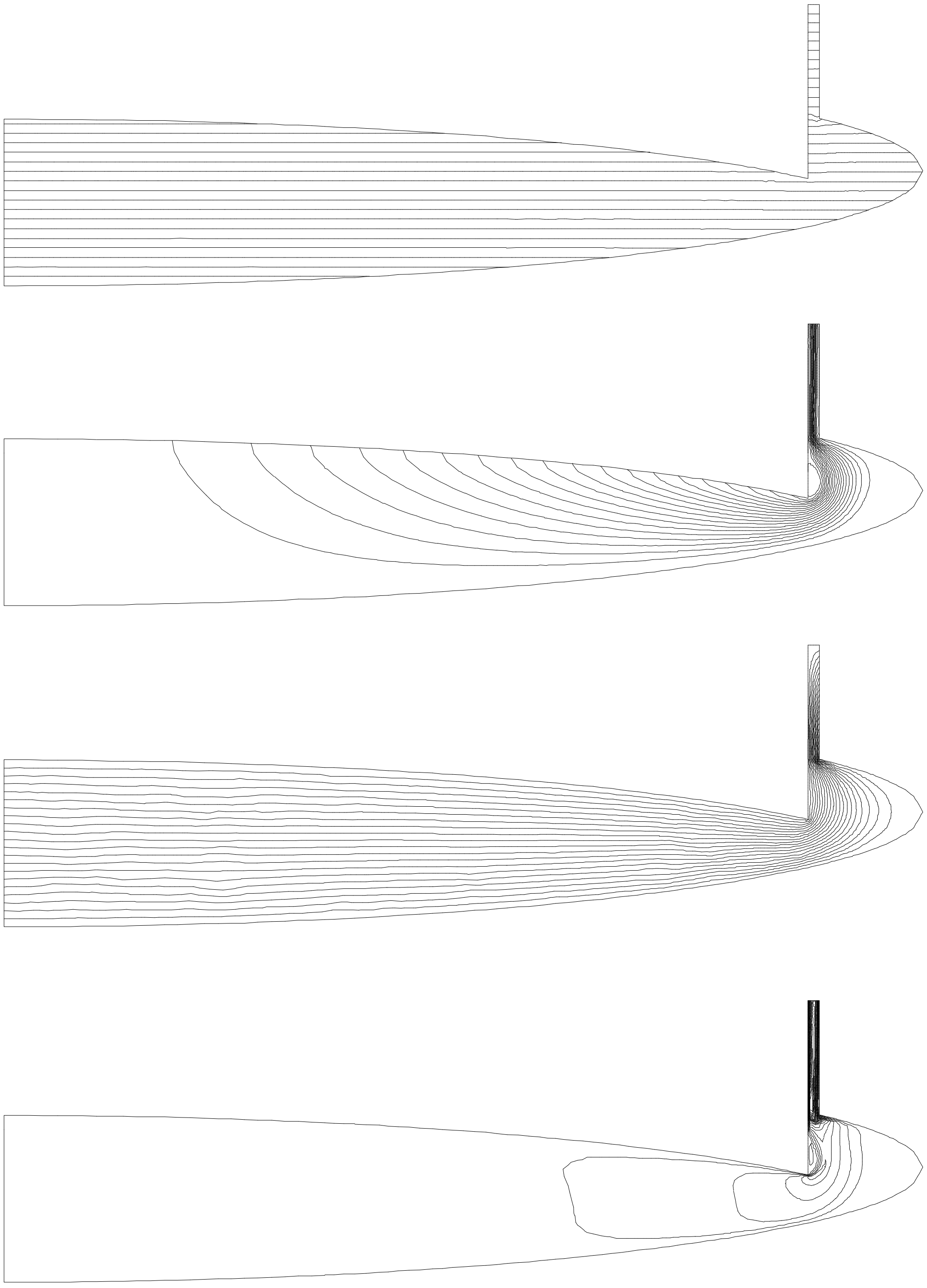

Figure 5.4.5. Numerical results at *t*= 9min. results shown are, from top to bottom, pressure contours, streamlines, contours of mesh velocity norm and contours of velocity norm.

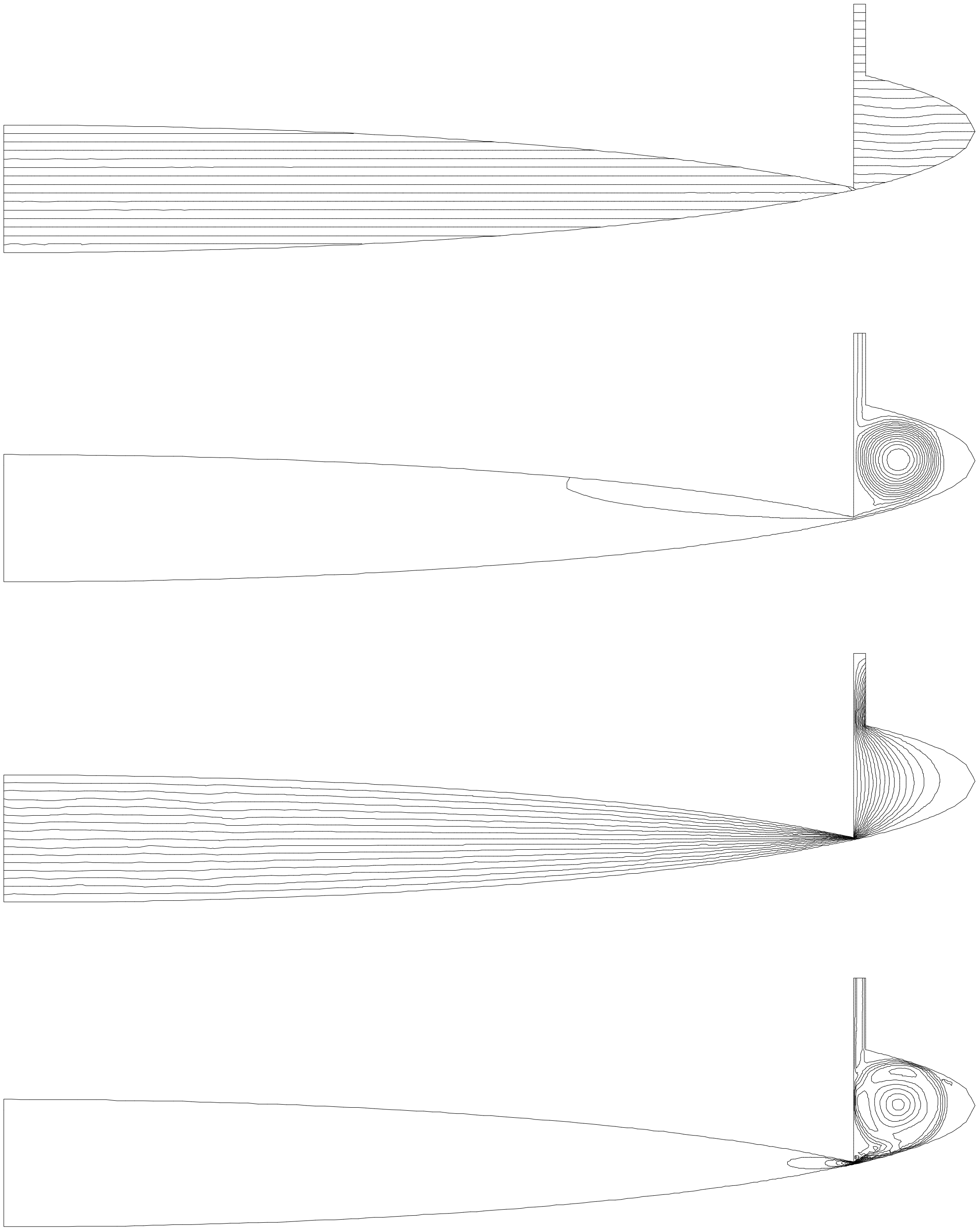

Figure 5.4.6. Numerical results at *t*= 16min. Results shown are, from top to bottom, pressure contours, streamlines, contours of mesh velocity norm and contours of velocity norm.

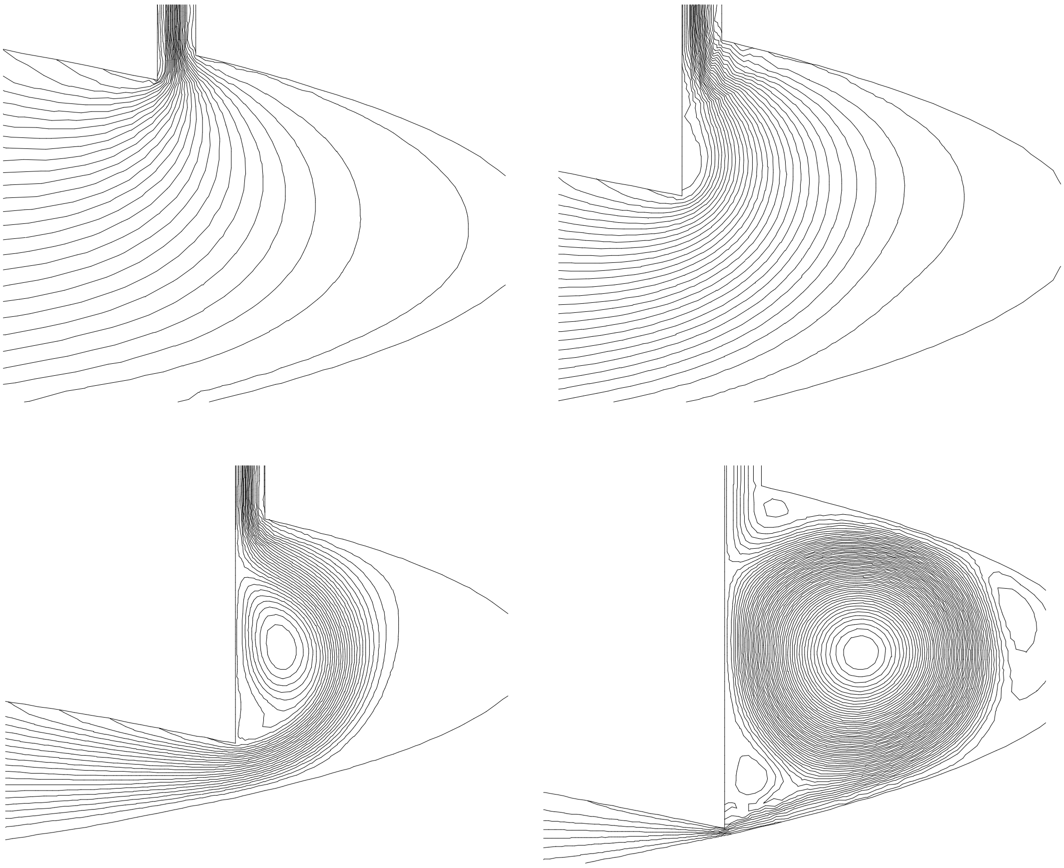

Figure 5.4.7. Zoom of the streamlines at the external (rightmost) part of the chamber to illustrate the development of a big central vortex as the eruption proceeds. The corresponding time instants are *t*= 2min (top left), *t*= 7min (top right), *t*= 12min (bottom left) and *t*=16min (bottom right). Pictures are not on the same scale.

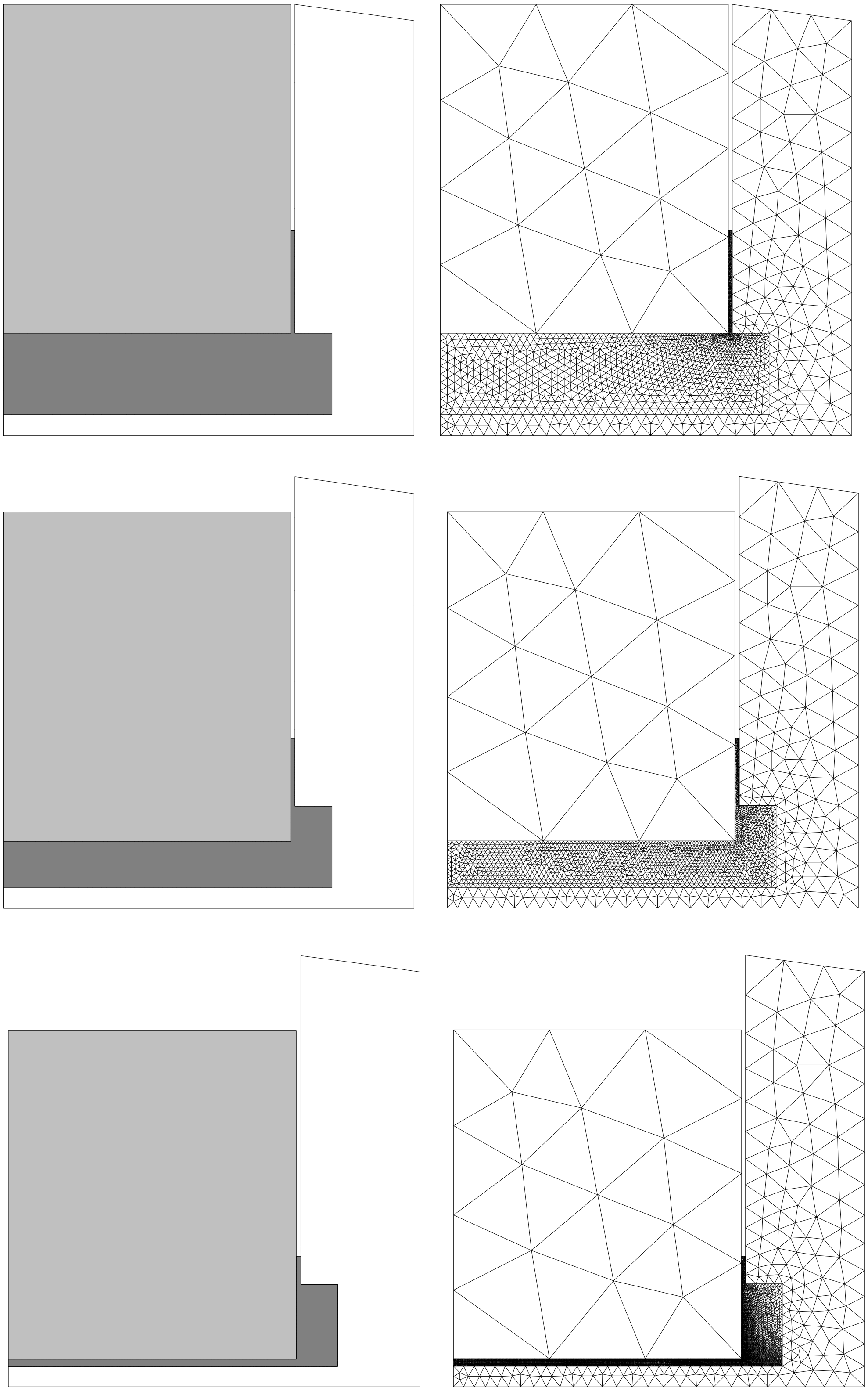

Figure 5.4.8. Geometry and space discretisation for the cylindrical chamber at three different time instants. Left column: illustration of the different domains: fluid (dark grey), block (grey) and background (white). Right column: space discretisations (3 different non-matching meshes at any time instant). The corresponding time instants are, form top to bottom, *t*=0, *t*= 12min and *t*=23min.

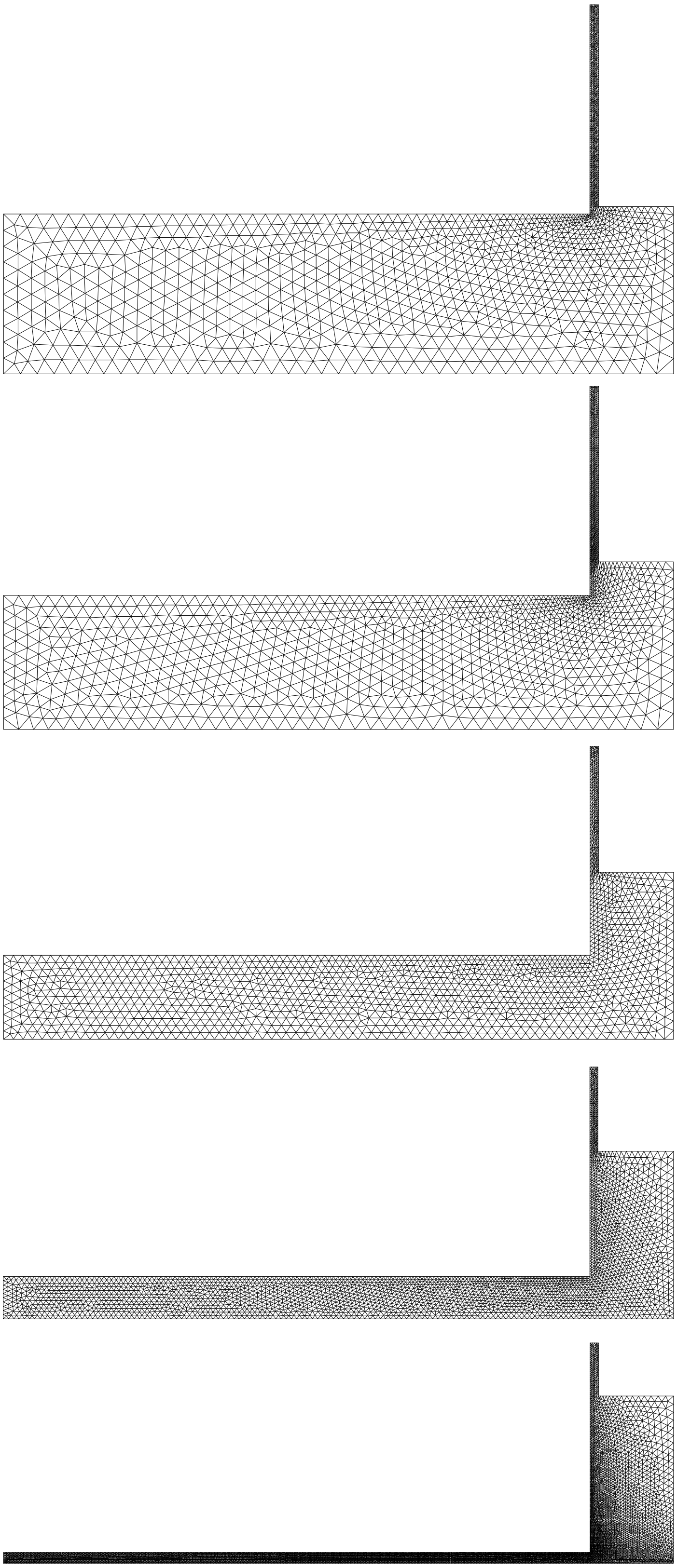

Figure 5.4.9. From top to bottom: views of the fluid's meshes 1, 2, 5, 7 and 9. The corresponding time instants at which these meshes are generated are *t*= 0, *t*= 3.5min, *t*= 11.5min, *t* =17.5min and t= 24min respectively.

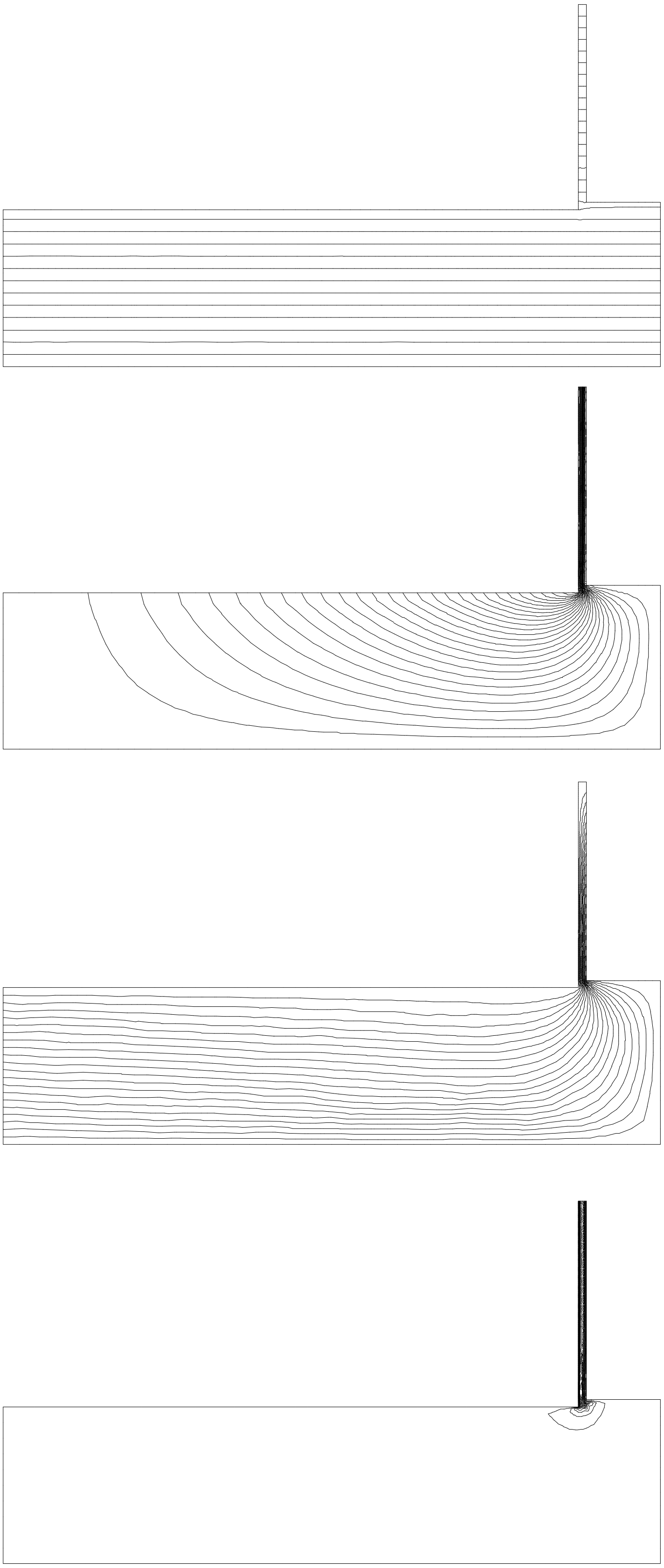

Figure 5.4.10. Numerical results at *t*= 2min. Results shown are, form top to bottom, pressure contours, streamlines, contours of mesh velocity norm and contours of velocity norm.

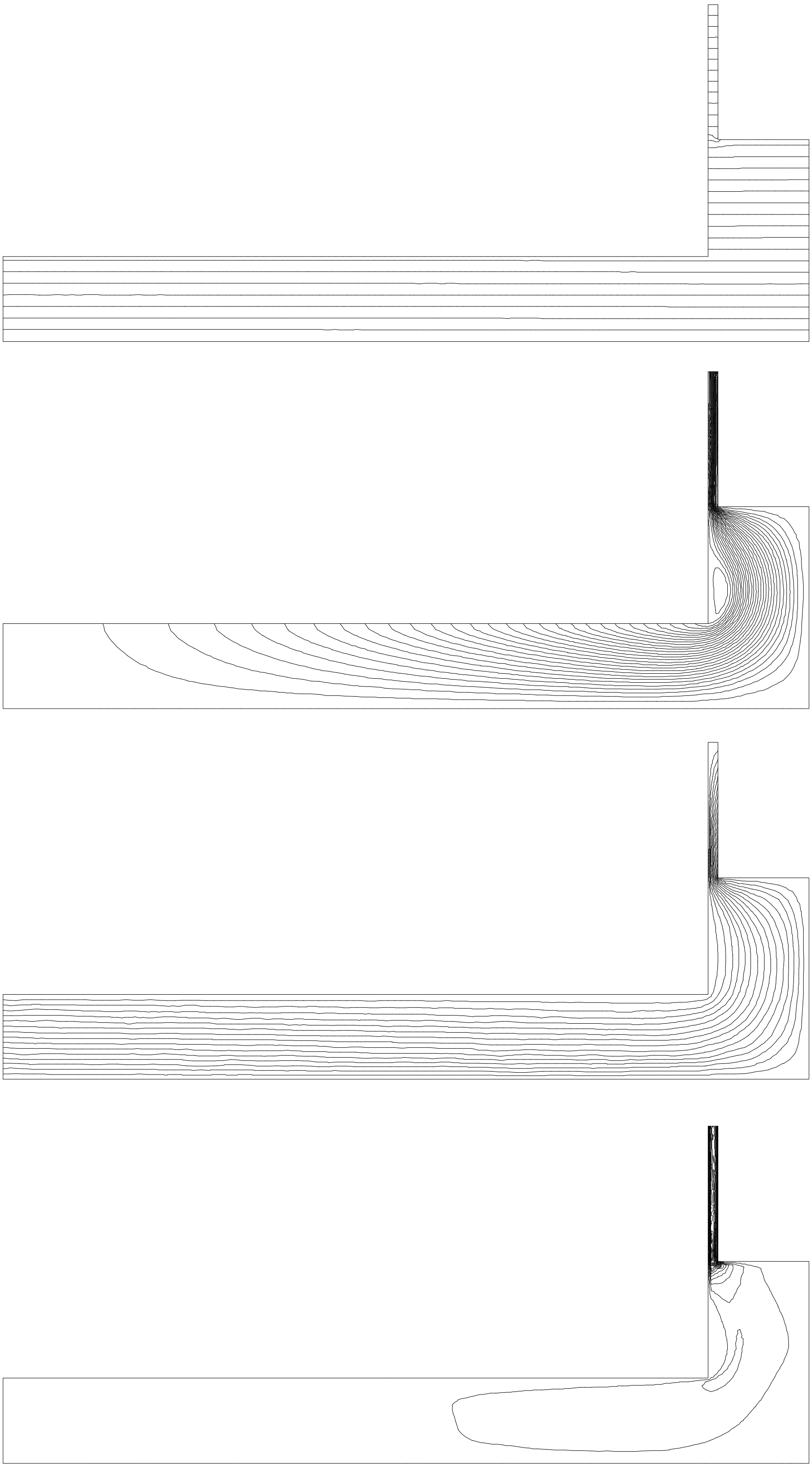

Figure 5.4.11. Numerical results at *t*= 15min. Results shown are, form top to bottom, pressure contours, streamlines, contours of mesh velocity norm and contours of velocity norm.

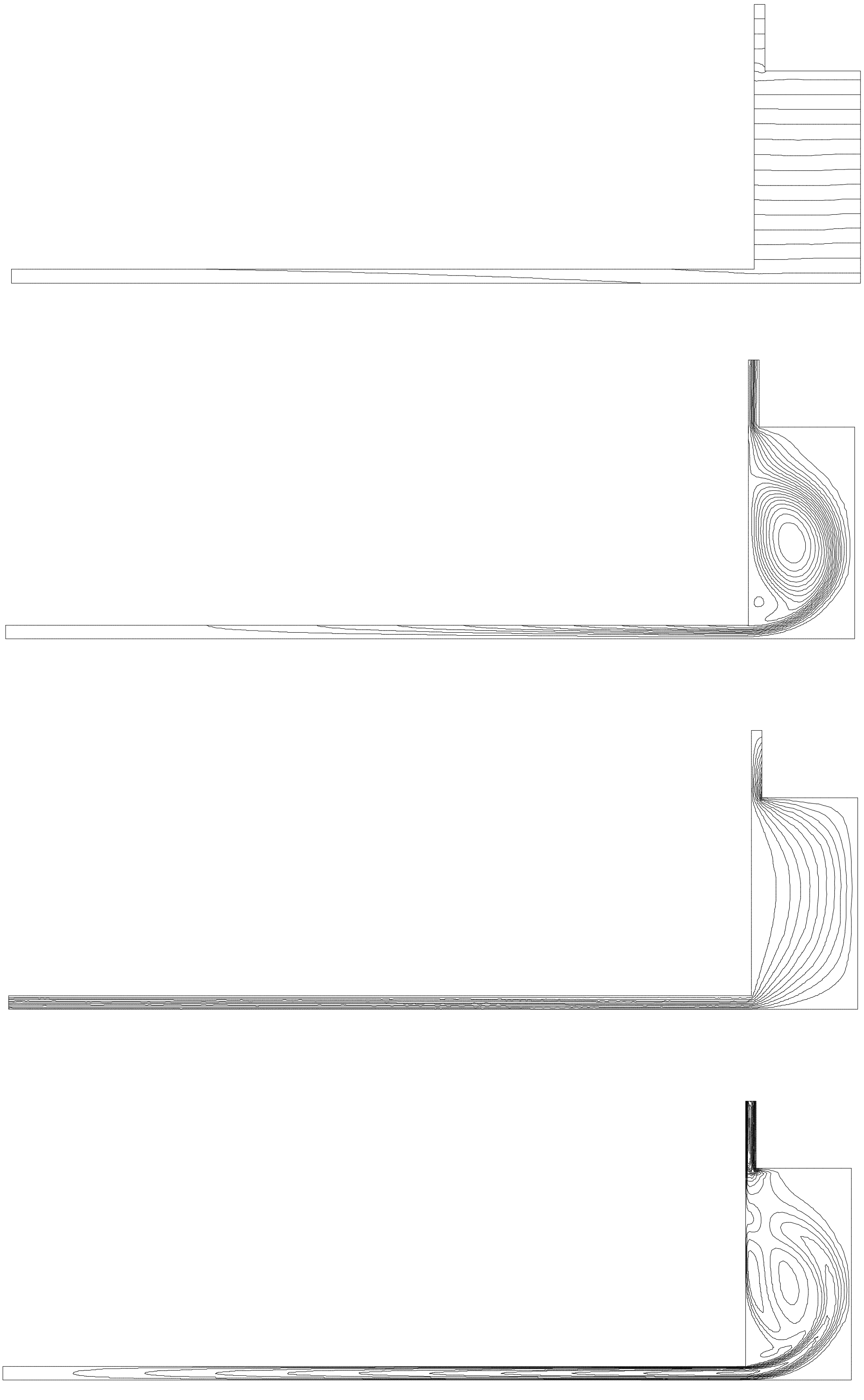

Figure 5.4.12. Numerical results at *t*= 24min. Results shown are, form top to bottom, pressure contours, streamlines, contours of mesh velocity norm and contours of velocity norm.

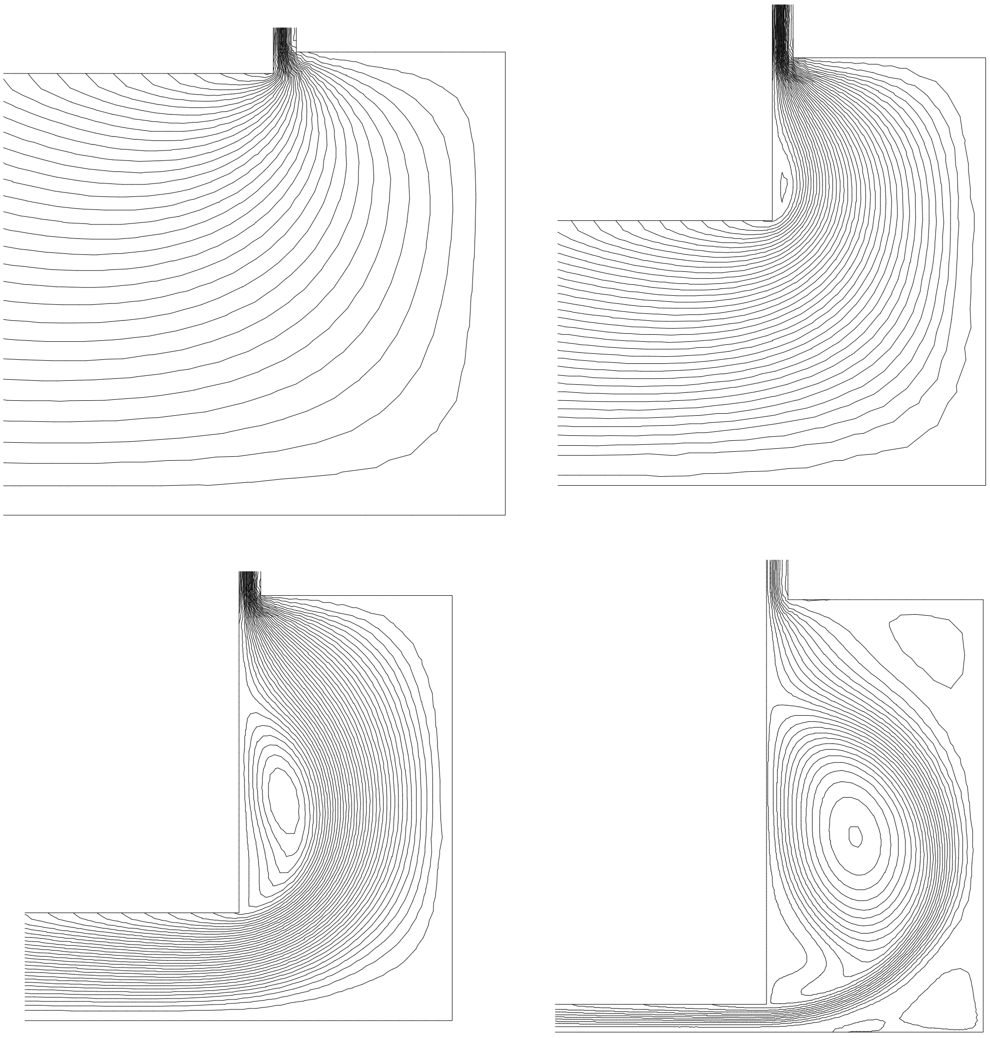

Figure 5.4.13. Zoom of the streamlines at the external (rightmost) part of the chamber to illustrate the development of a big central vortex as the eruption proceeds. The corresponding time instants are *t*= 2min (top left), *t*= 10min (top right), *t*= 19min (bottom left) and *t*=24min (bottom right).

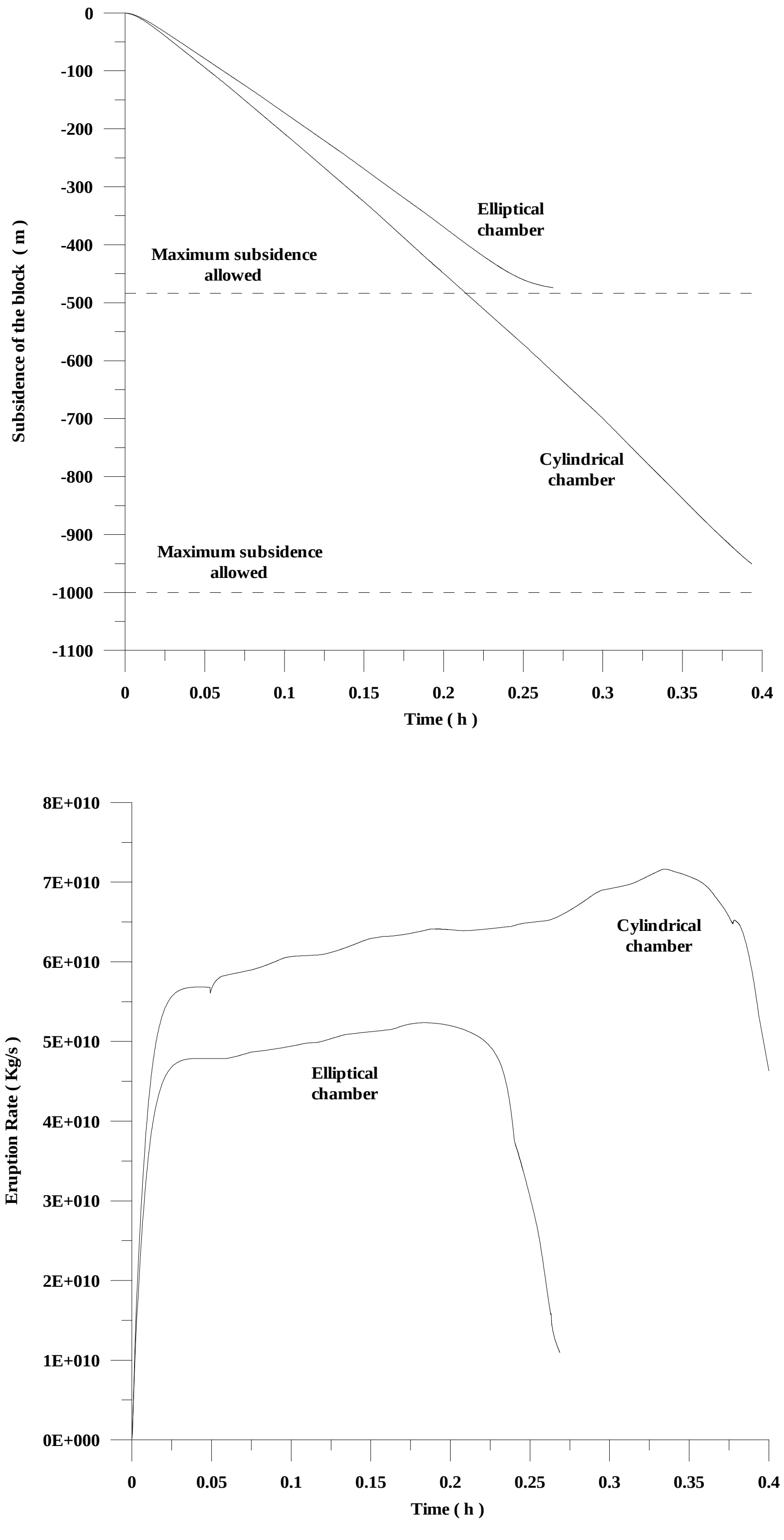

Figure 5.4.14. Top: subsidence (displacement) of the block plotted versus time for the elliptical and cylindrical chambers. The maximum subsidence allowed is indicated by discontinuous lines. Bottom: eruption rate plotted versus time. Numerical simulations predict an initial rapid increase of the eruptive intensity, a plateau and a rapid decrease at the final stages. Oscillations during the plateau phase are a numerical effect originated by the remeshings.

Figure 5.4.15 shows the total erupted mass and the erupted mass fraction plotted versus time for the elliptical and cylindrical chambers. Simulations suggest that once caldera collapse has started it will tend to empty most of the chamber. However, it is important to point out that, in the simulations, the end of the eruption is given only by a geometrical criteria, that is, the process stops when the subsiding block shocks against the bottom walls of the chamber[1]. It represents an extreme (but not unrealistic) case in which the subsidence is the maximum allowed, most of the magma is extruded, and the original magma chamber is completely destroyed. In natural systems, however, the process may stop at any previous instant by two main reasons. Firstly, it has been assumed that the chamber is filled with a chemically homogeneous magma lighter than the environment. Nevertheless, one could perfectly imagine a chemically heterogeneous chamber (stratified in density) having a magma, at its bottom, denser than the subsiding block. Such a framework would result in a withdrawal of the uppermost parts of the chamber (those filled with lighter magma) and a subsequent stop of the eruption once the denser magma, initially placed at the bottom of the chamber, begins to be extruded, i.e. when the weight of the magma column within the ring fault and the viscous forces could overcome the weight and the inertia of the subsiding block which, at the end of the eruption, would float over the denser remainder magma[2]. The second possibility to stop the process could be a closure of the conduit originated either by a change in the surrounding stress field or because the ring faults are not, in fact, completely vertical fissures. In fact, the inclination of dipping inwards faults could perfectly result in a closure of the fault induced by the subsidence of the block downwards.

A final remark. Some results of the simulations (velocity of subsidence, eruption rate, formation of vortexes, etc.) are, obviously, very dependent on the magma viscosity. To envisage this dependency, other simulations considering different magma viscosities of 10^3, 10^4 and 10^5 Pa.s have been also carried out. Some interesting results, only for the case of the elliptical geometry, are illustrated in figures 5.4.16 to 5.4.18. As expected, the higher is the magma density the lower is the "terminal" velocity of subsidence and, therefore, the longer is the duration of the eruption. However, it can be observed from these figures how the cases with viscosities 10^3 and 10^4 are very similar. This non-intuitive result is explained because the term which accounts for the forces of the fluid over the structure has two contributions, one due to pressure and another due to viscous forces (traction) which are proportional to viscosity (see equation (4.3.4)).

---

[1] For the particular geometries considered, it occurs when the subsidence is 475m for the elliptical chamber and 1000m (the whole initial chamber thickness) for the cylindrical.

[2] In fact, field evidences show that, in many cases, caldera-forming eruptions end with the emplacement of rhyolitic non-vesiculated (i.e. denser) lava domes along the ring fault.

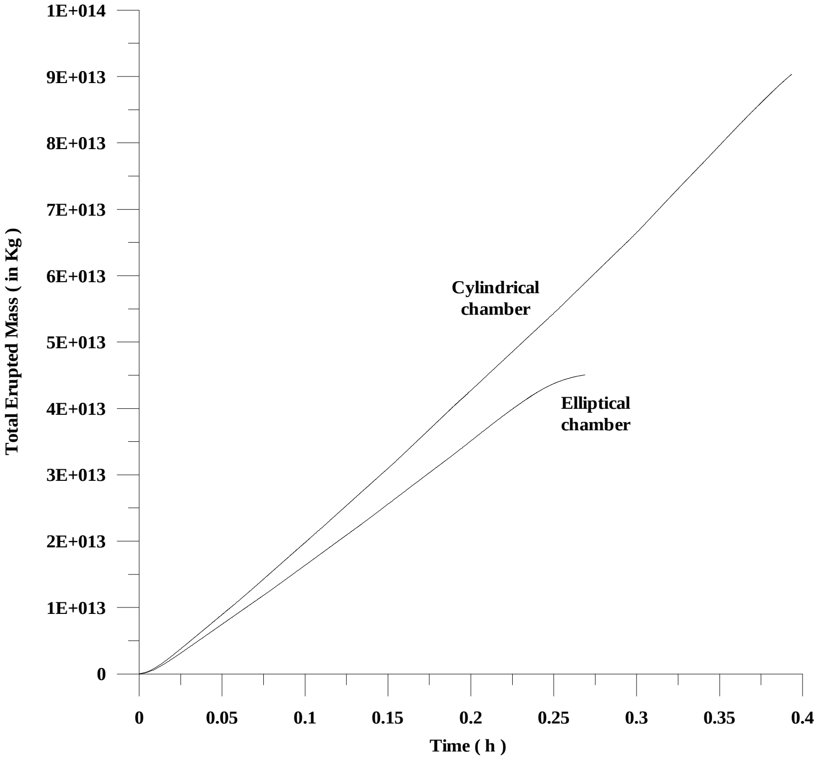

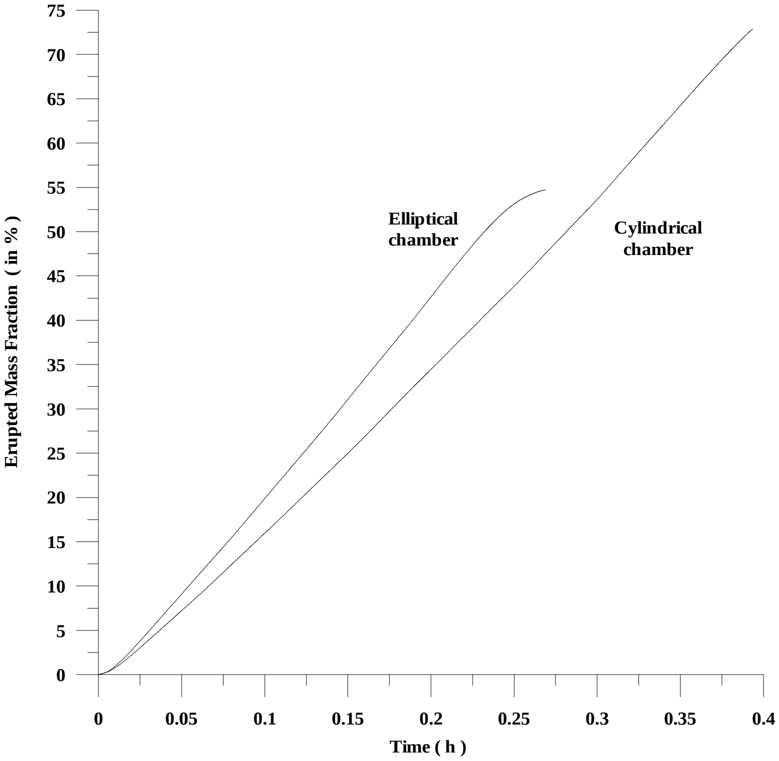

Figure 5.4.15. Total erupted mass (top) and erupted mass fraction plotted versus time for the elliptical and cylindrical chambers.

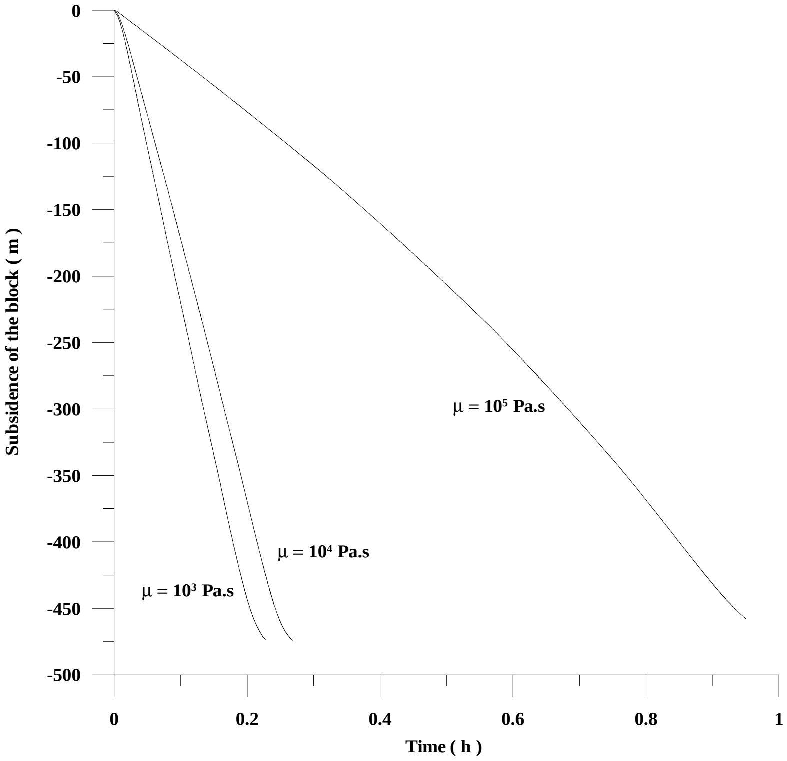

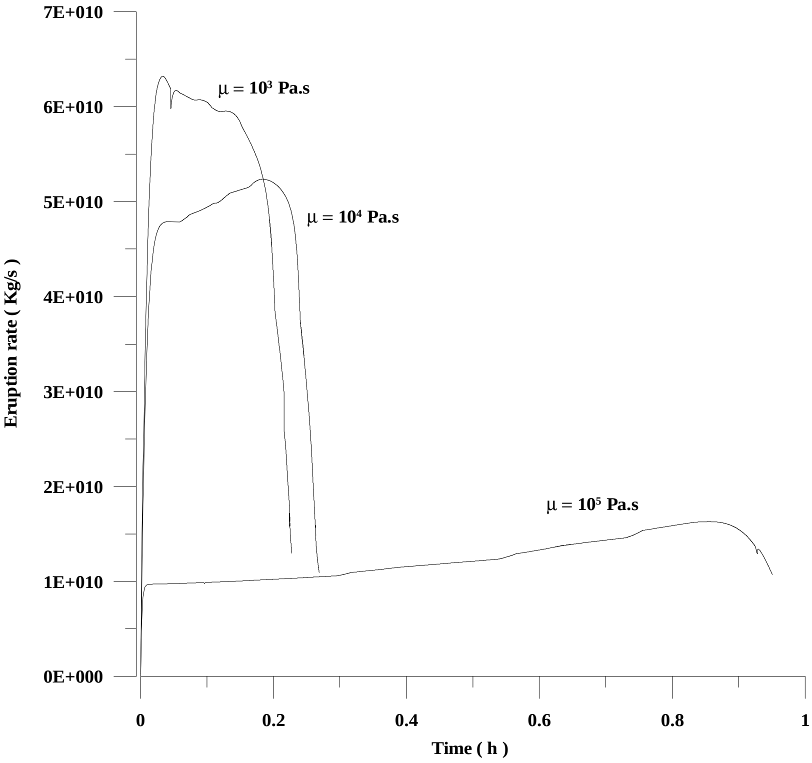

Figure 5.4.16. Results for the elliptical chamber considering different magma viscosities of 10^3, 10^4 and 10^5 Pa.s. Top: subsidence (displacement) of the block plotted versus time. Bottom: eruption rate plotted versus time.

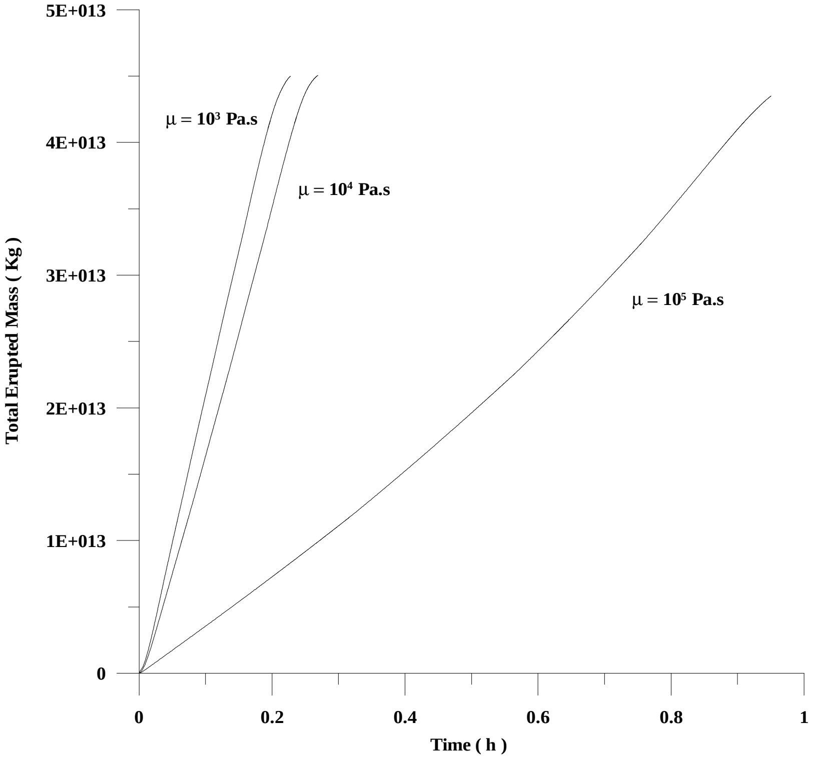

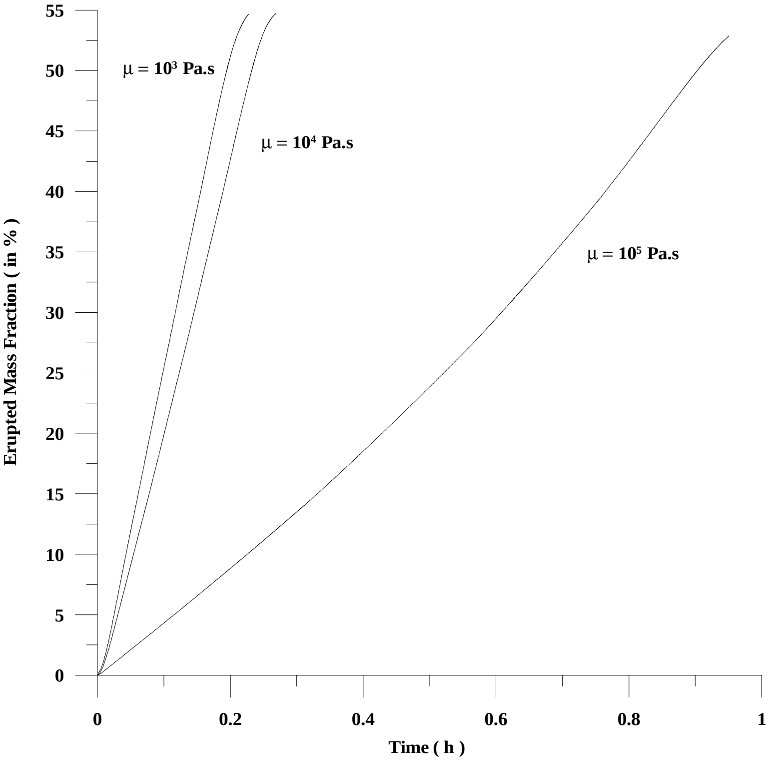

Figure 5.4.17. Total erupted mass (top) and erupted mass fraction (bottom) plotted versus time for the elliptical chamber and considering different magma viscosities of 10^3, 10^4 and 10^5 Pa.s.

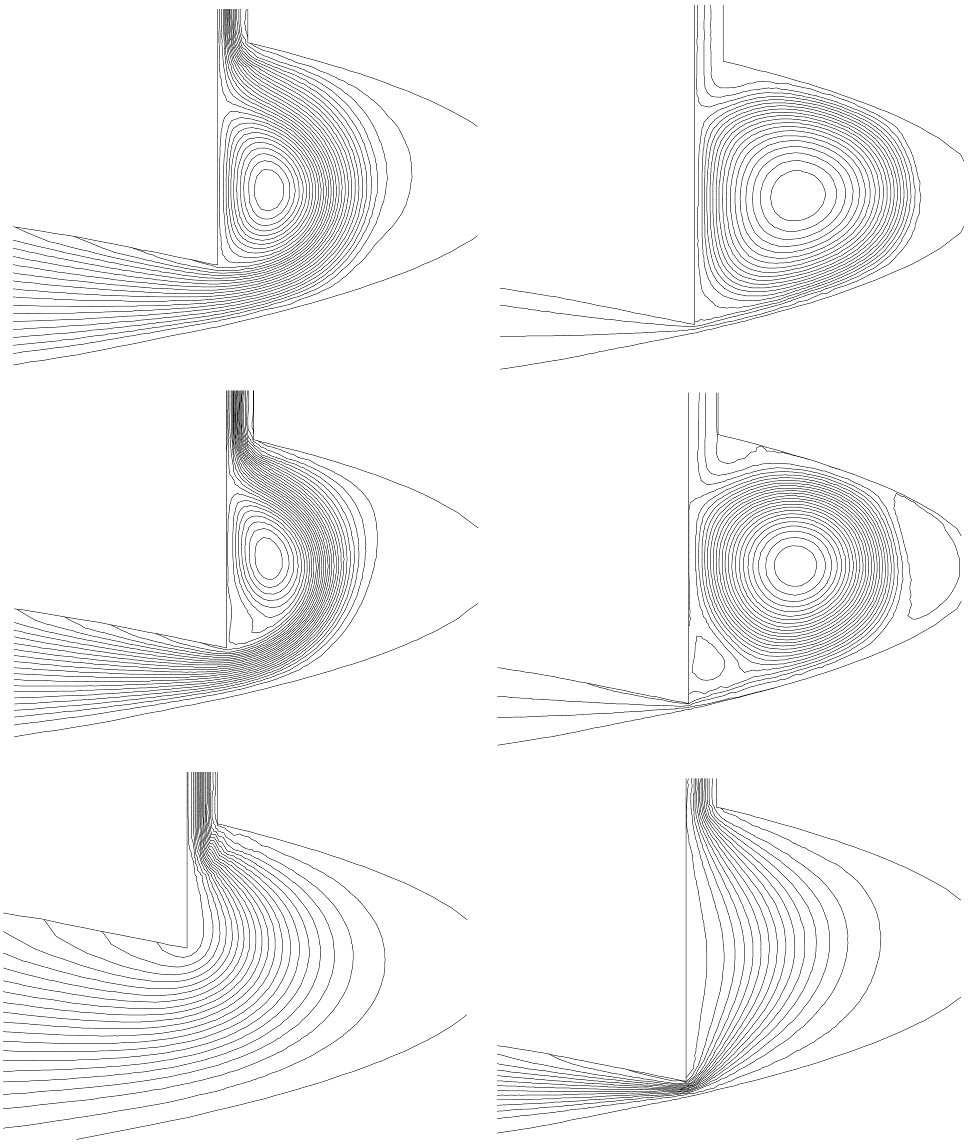

Figure 5.4.18. Zoom of the streamlines at the external part of the chamber, just below the entrance of the conduit. Results are for different magma viscosities of 10^3 Pa.s (top), 10^4 Pa.s (middle) and 10^5 Pa.s (bottom). Assuming that $\mathbf{u_b}$ is 0.5 m/s, the corresponding Reynolds numbers are 60, 6 and 0.6 respectively. The cases with viscosities 10^3 Pa.s and 10^4 Pa.s are very similar. However, no vortex is formed when the viscosity is 10^5 Pa.s.

For viscosities in the range or lower than 10^4 the pressure contribution dominates over the viscous one and, therefore, variations of viscosity within this range produce only minor corrections to the force which acts over the block. In contrast, for viscosities in the range or greater than 10^5 the viscous contribution becomes comparable (or greater) than that due to pressure and the terminal velocity (i.e. the eruption rate) reduces substantially. It should be noted that all the simulations performed underestimate the force that acts over the falling block due to the cutting of the computational domain (remind that only the lowermost part of the conduit is considered). The viscous contribution at the uppermost part of the conduit, where magma viscosity increases notably due to volatile exsolution, would lead to a lower terminal velocity and, hence, to a longer eruption. The results obtained here still apply but, in a real case, would probably be observed in a much longer time scale.

5.4.2 Partially Vesiculated Magma

Consider now the more realistic case in which magma is partially vesiculated. Only results for the elliptical chamber geometry are presented here as example. Pressure at the computational outlet is set to lithostatic (90 MPa for this particular geometry and host rock density). Under these conditions and, for a rhyolitic magma composition, the minimum volatile (water) content required to ensure vesiculation is 3.9% in weight. Two cases, named A and B, will be contemplated. In case A the amount of volatiles is 4% in weight ($W = 0.04$). This value is close to the minimum so that only part of the conduit is vesiculated at the beginning of the eruption. The exsolution level is initially located about 300m above the top of the chamber[1]. In case B the amount of volatiles is 4.25% in weight ($W = 0.0425$) and the exsolution level is placed initially at about 200m below the chamber top (23% of the chamber volume is initially vesiculated). In both cases the whole simulation of the eruption requires up to 6 different meshes for the fluid (i.e. 5 remeshings). Figures 5.4.19 and 5.4.20 present some results (contours of density and streamlines) for case A at different time instants. Same results for case B are illustrated in figures 5.4.21 and 5.4.22. In general, the behaviours (erupted mass, kinematics of the block, etc.) are quite similar to the case presented in the previous section, where magma is assumed to be non-vesiculated. Figure 5.4.23 plots the subsidence of the block and the temporal evolution of the exsolution level for cases A and B. Finally, the total erupted mass and the erupted mass fraction is depicted in figure 5.4.24. A characteristic feature of the simulations is that the exsolution level deepens (shifts downwards) with a velocity similar to that of the subsiding block. This phenomena is illustrated in figure 5.4.23 (see also figures 5.4.19 to 5.4.22). Note that when the chamber is vesiculated, as it occurs in case B, the exsolution surface[2] is not horizontal because the movement of subsidence causes a pressure gradient so that pressure is greater "below the block" and lower at the "outermost part of the chamber", below the entrance of the conduit. In consequence, and as reflected in figure 5.4.22, the level of exsolution (i.e. the exsolution surface) is not horizontal at all.

---

[1] The top of the chamber is, by definition, the point which at $t = 0$ is closer to the Earth's surface. Note that for elliptical chambers this point is located at a radial coordinate $r = 0$ (i.e. at the symmetry axis). Note also that, in caldera-forming eruptions, the vertical coordinate of this point varies due to the subsidence of the block.

[2] The exsolution surface is determined by the condition $P = P_c$

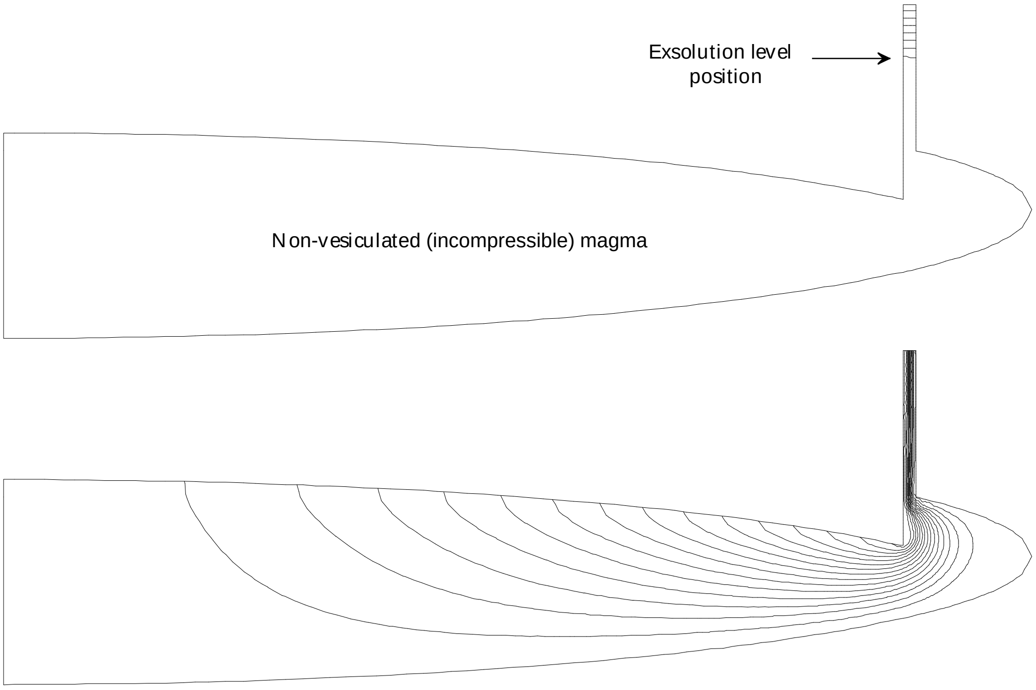

Figure 5.4.19. Case A. Results at *t* = 15min. Top: contours of density. Bottom: streamlines

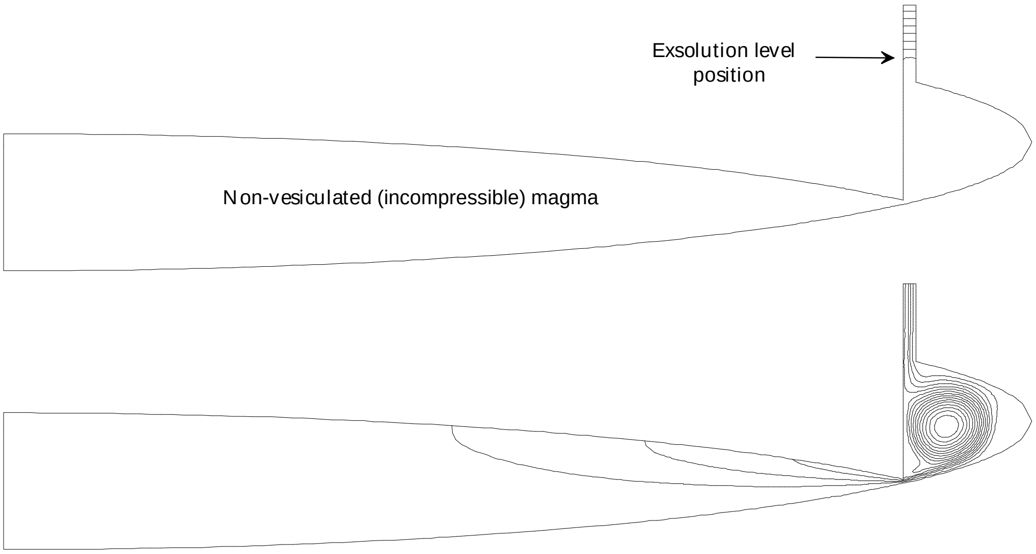

Figure 5.4.20. Case A. Results at *t* = 30min. Top: contours of density. Bottom: streamlines.

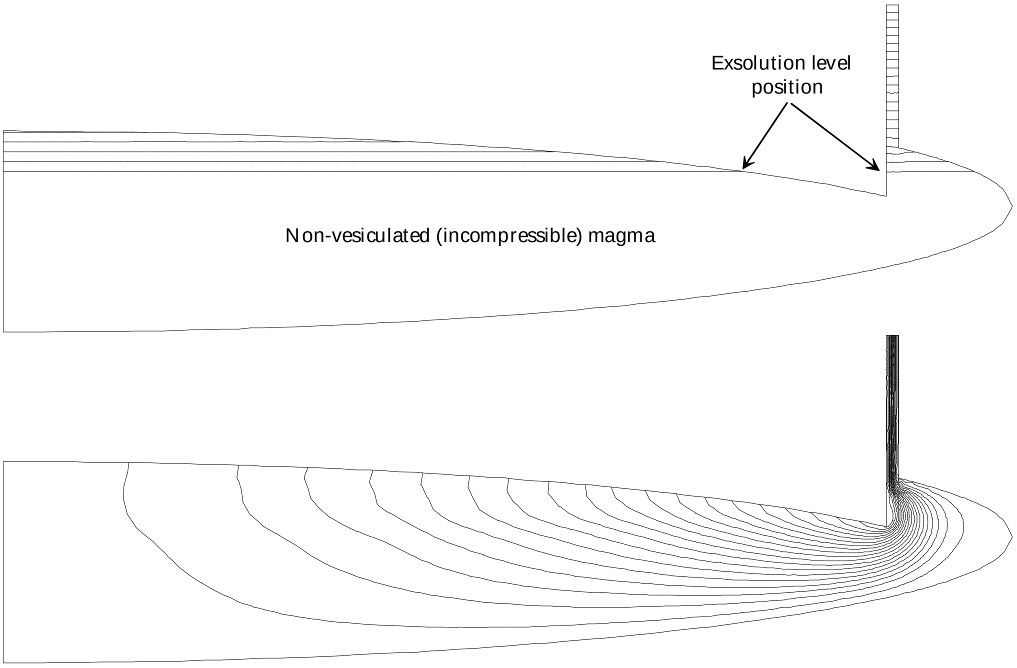

Figure 5.4.21. Case B. Results at *t* = 10min. Top: contours of density. Bottom: streamlines.

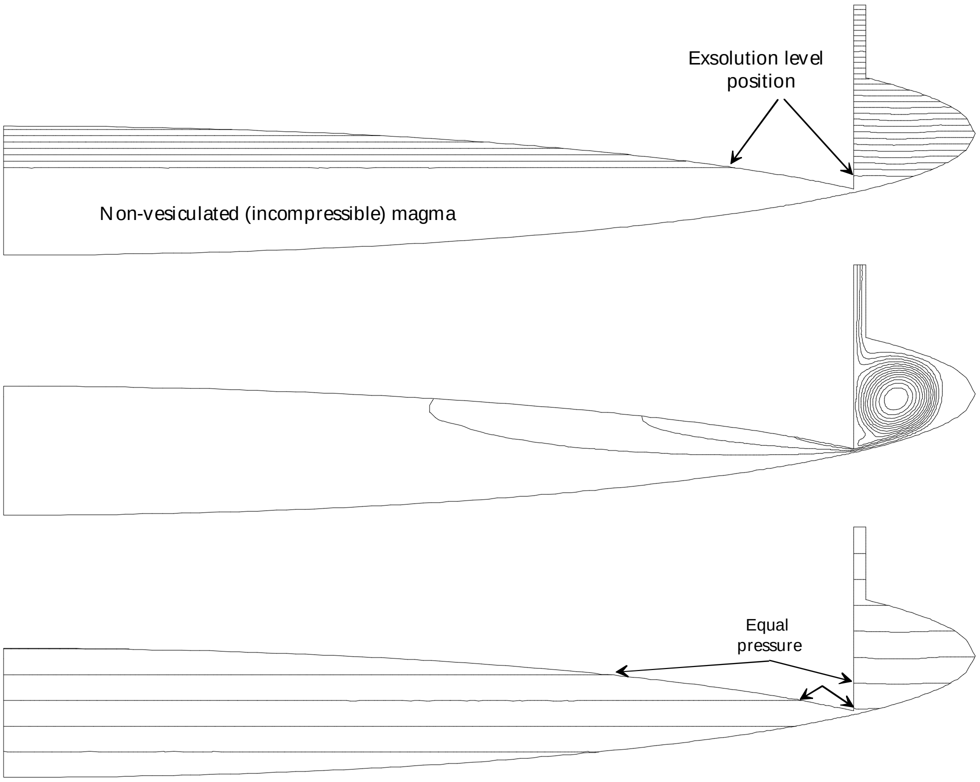

Figure 5.4.22. Case B. Results at *t* = 22.5min. Top: contours of density. Middle: streamlines. Bottom: pressure contours.

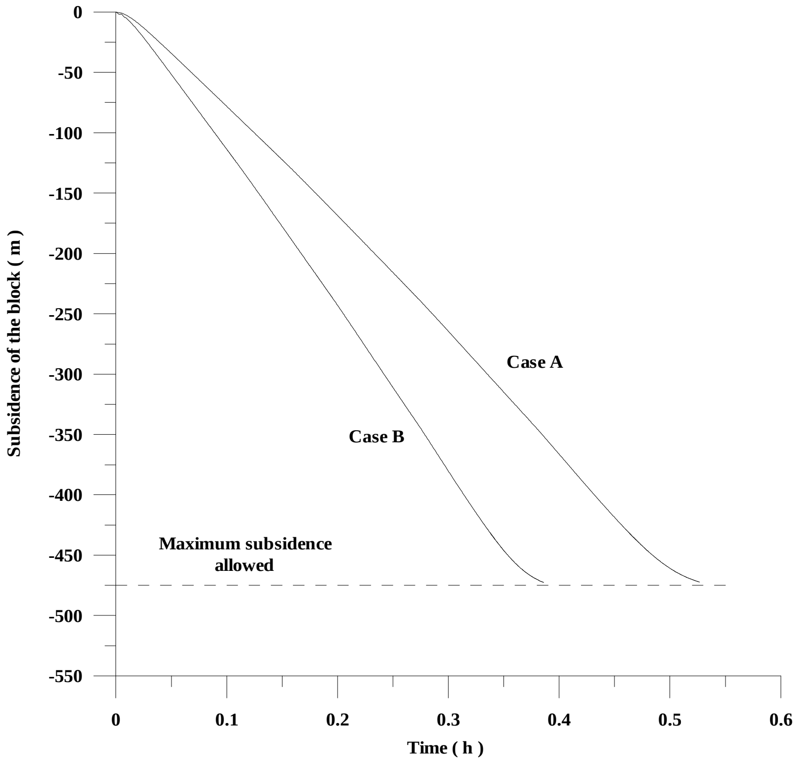

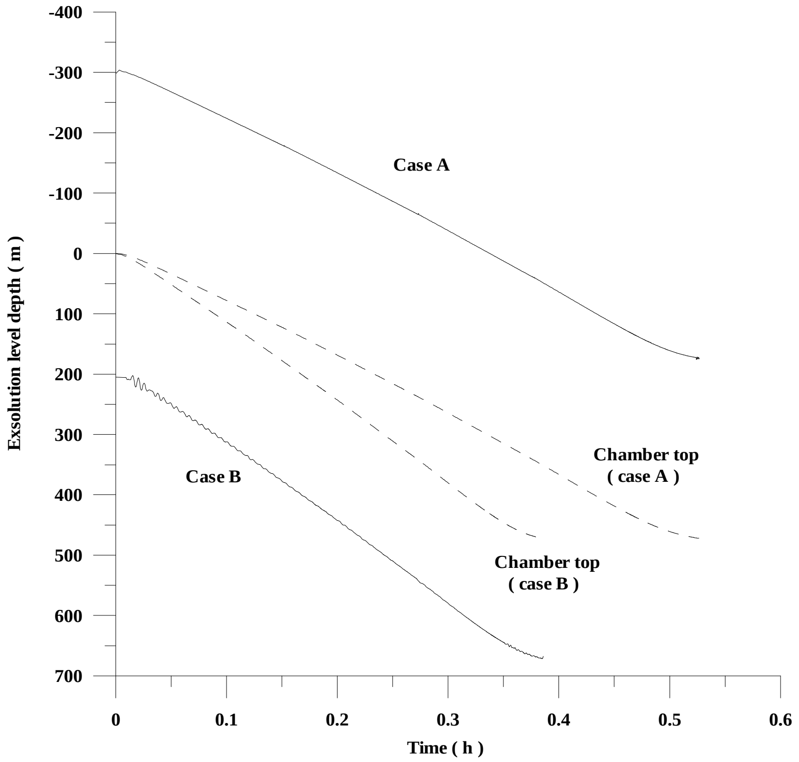

Figure 5.4.23. Top: subsidence (displacement) of the block plotted versus time for cases A and B. The final subsidence is the maximum allowed. Bottom: position of the exsolution level. The origin is the position of the chamber top at t = 0. The (variable) position of the chamber top is also indicated by discontinuous lines.

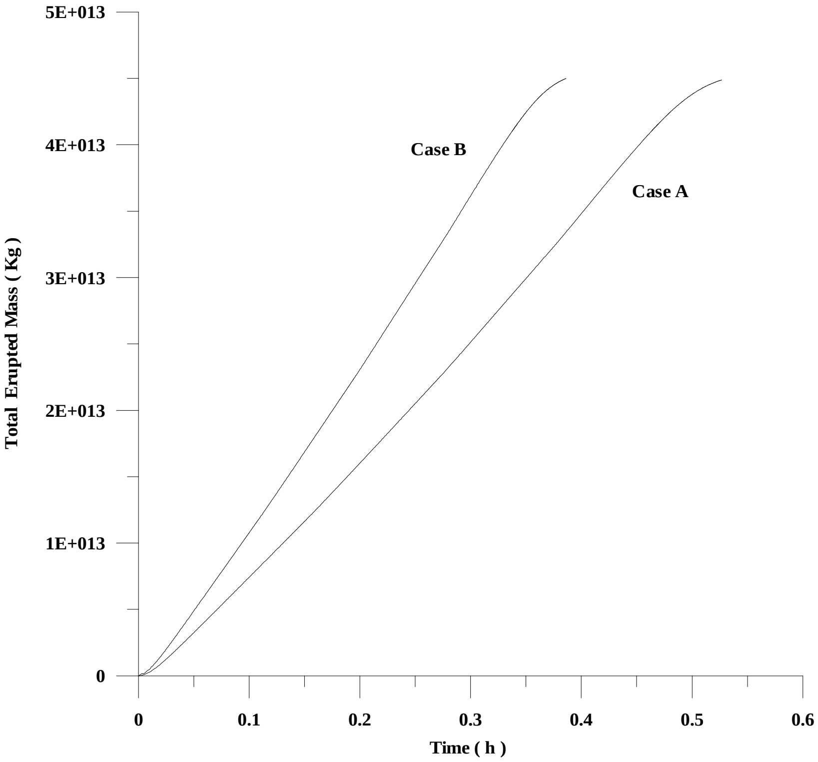

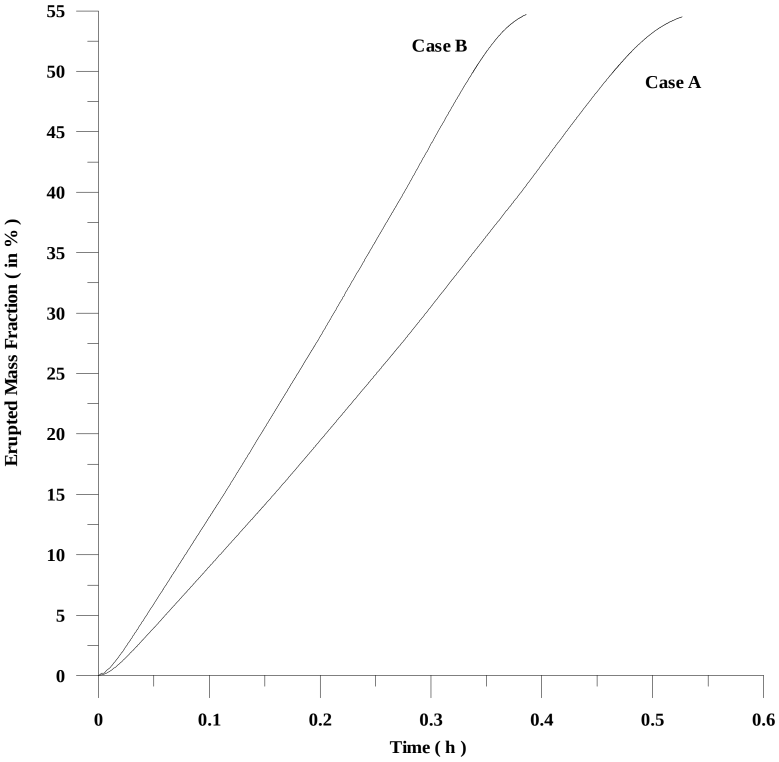

Figure 5.4.24. Total erupted mass (top) and erupted mass fraction (bottom) for the cases A and B respectively.

5.5 References

Blake, S., and G. N. Ivey, Density and viscosity gradients in zoned magma chambers, and their influence on withdrawal dynamics, *J. Volcanol. Geotherm. Res.*, *30*, 201-230, 1986a.

Blake, S., and G. N. Ivey, Magma mixing and the dynamics of withdrawal from stratified reservoirs, *J. Volcanol. Geotherm. Res.*, *27*, 153-178, 1986b.

Blake, S., and J. H. Fink, The dynamics of magma withdrawal from a density stratified dyke, *Earth Planet. Sci. Lett.*, *85*, 516-524, 1987.

Bower, S., and A. W. Woods, Control of magma volatile content and chamber depth on the mass erupted during explosive volcanic eruptions, *J. Geophys. Res.*, *102*, 10273-10290, 1997.

Dobran, F., Nonequilibrium flow in volcanic conduits and application to the eruptions of Mt. St. Helens on May 18, 1980, and Vesuvius in AD 79, *J. Volcanol. Geotherm. Res.*, *49*, 285-311, 1992.

Folch, A., J. Martí, R. Codina, and M. Vázquez, A numerical model for temporal variations during explosive central vent eruptions, *J. Geophys. Res.*, *103*, 20883-20899, 1998.

Folch, A., M. Vázquez, R. Codina, and J. Martí, A fractional-step finite-element method for the Navier-Stokes equations applied to magma chamber withdrawal, *Computers & Geosciences*, *25*, 263-275, 1999.

Greer, J. C., Dynamics of withdrawal from stratified magma chambers, M. A. Thesis, Ariz. State Univ., Tempe, 1986.

Gudmundsson, A., Formation and development of normal-fault calderas and the initiation of large explosive eruptions, *Bull. Volcanol.*, *60*, 160-171, 1998.

Gudmundsson, A., J. Martí, and E. Turón, Stress fields generating ring faults in volcanoes, *Geophys. Res. Lett.*, *24*, 1559-1562, 1997.

Hirsch, C., Numerical Computation of Internal and External Flows, *John Wiley & Sons*, 1991.

Huppert, H. E., R. S. J. Sparks, and J. S. Turner, Effects of volatiles on mixing in calc-alkaline magma systems, *Nature*, *297*, 554-557, 1982.

Martí, J., A. Folch, G. Macedonio, and A. Neri, Pressure evolution during caldera forming eruptions, *Earth Planet. Sci. Lett.*, *175*, 275-287, 2000.

Papale, P., and F. Dobran, Modelling of the ascent of magma during the plinian eruption of Vesuvius in AD 79, *J. Volcanol. Geotherm. Res.*, *58*, 101-132, 1993.

Papale, P., and F. Dobran, Magma flow along volcanic conduit during the plinian and pyroclastic flow phases of the May 18, 1980, Mount St. Helens eruption, *J. Geophys. Res.*, *99*, 4355-4373, 1994.

Shaw, H. R., Links between magma-tectonic rate balances, plutonism and volcanism, *J. Geophys. Res.*, *90*, 11275-11288, 1985.

Snyder, D., and S. Tait, Magma mixing by convective entrainment, *Nature*, *379*, 529-531, 1996.

Spera, F., Some numerical experiments on the withdrawal of magma from crustal reservoirs, *J. Geophys. Res.*, *89*, 8222-8236, 1984.

Spera, F., D. A. Yuen, J. C. Greer, and G. Sewell, Dynamics of magma withdrawal from stratified magma chambers, *Geology*, *14*, 723-726, 1986.

Tanner, R. I., Engineering rheology, *Claderon Press*, 1985.

Touloukian, Y. S., W. R. Judd, and R. F. Roy, Physical properties of rocks and minerals, v. 1, *McGraw-Hill,* New York, 1981.

Trial, A. F., F. Spera, J. Greer, and D. Yuen, Simulations of magma withdrawal from compositionally zoned bodies, *J. Geophys. Res.*, *97*, 6713-6733, 1992.

Turner, J. S., and I. H. Campbell, Convection and mixing in magma chambers, *Earth Sci. Rev.*, *23*, 255-352, 1986.

Chapter 6

Ground Deformation

Chapter Contents

Abstract

This chapter contents some examples to illustrate the applicability of the numerical model developed in order to compute viscoelastic ground deformations in volcanic areas. Firstly, the general procedure for an axisymmetrical problem is outlined. Secondly, a parametric comparison between the analytical (point source) and the numerical (extended source) versions of the method is performed. The assimilation of the pressure source with a point source is a necessary requirement to derive analytical solutions, and thus, analytical methods have always an implicit error. The comparison allows to quantify this error and constrains quantitatively the range of applicability of these widely used analytical procedures. In section 6.3, the model is used to simulate the 1982-1984 uplift episode of the Campi Flegrei volcanic field. Finally, a 3D application to Tenerife island is done in order to predict which would be the effect of a hypothetical pressurisation of the present shallow magmatic system. Due to the numerous simplifying hypothesis, this practical example should be regarded only as a first approach but, however, gives some insights to improve the design of the monitoring system. It also points out how, at least for this particular case, the use of a 2D (axisymmetric) model with an approximated conical topography proportionates also similar deformation values.

6.1 The Axisymmetrical Problem

This section considers an axisymmetrical example to illustrate the application of the numerical model herein proposed in order to compute viscoelastic ground deformations in volcanic areas. The numerical procedure as well as the different rheological models, named 1, 2, and 3, been already exposed in section 4.5.2 (table 4.5.1 summarises the properties of these three viscoelastic rheologies commonly assumed for the crust). Figure 6.1.1 illustrates schematically the general axisymmetric problem in which an ellipsoidal magma chamber of semi axis a and b is buried at depth H_{cha} below the Earth's surface. Obviously, topographic effects such as, for instance, the presence of a volcanic edifice, can be also considered. The media is characterised by the elastic Lamé parameters l and m as well as by the type of viscoelastic relaxation.

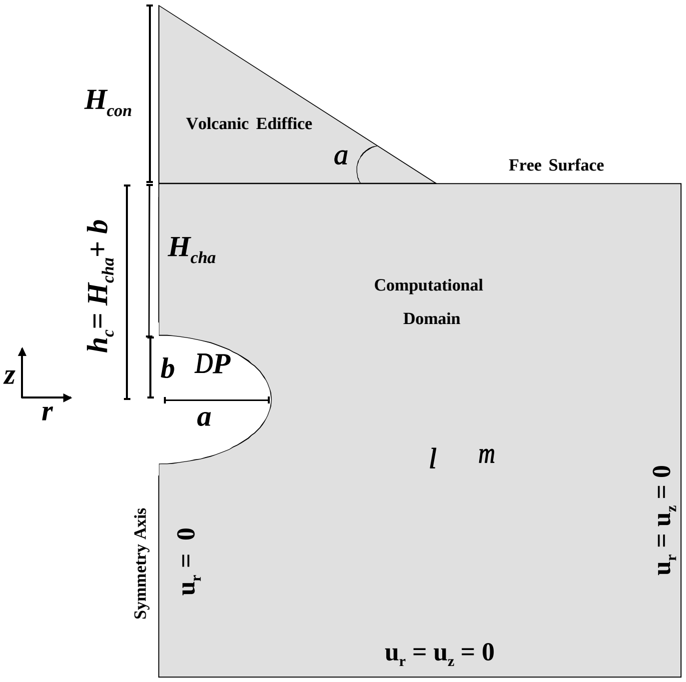

Figure 6.1.1. Schematic illustration of a general axisymmetrical problem. An ellipsoidal magma chamber with semi-axis a and b is located at depth H_{cha} below the Earth's surface. The size to depth ratio is defined as $e \equiv b/(b + H_{cha}) = b/h_c$. Optionally, a volcano with height H_{con} and average slope of the flanks a can be also considered (in particular, if $a = 0$ the topographic effects are neglected). The chamber has an overpressure ΔP and the crust is characterised by the Lamé parameters l and m that, optionally, may vary with depth. Symmetry axis is located at $r = 0$. Boundary conditions are as follows. Radial displacement along the symmetry axis is set to zero. The surface of the Earth is a free surface whereas displacements are fixed at both basal and lateral boundaries. These boundaries are located far away from the chamber in order to diminish the influence of boundary conditions on the solution.

Boundary conditions are always imposed in terms of the pressure increase inside the chamber ΔP[1]. Displacements are prescribed to zero in both basal and lateral faces of the domain while only the radial component is fixed to zero along the symmetry axis. The solution of this general problem allows to determine viscoelastic displacements and stresses within the domain at any time instant.

To illustrate the effect of the kind of relaxation consider first the case of a spherical magma chamber with $a = b = 1$Km and placed at 3Km below the surface. For simplicity, topography is neglected and the Lamé parameters are constant and equal to $l = m =$ GPa

$E = 75$GPa and $n = 0.25$). Despite in this example all the parameters are arbitrarily chosen and, hence, do not represent any specific real situation, their values are close to those commonly found in nature. Two different rheological responses are considered in a media composed by a layer of thickness 10 Km overlying a half-space.

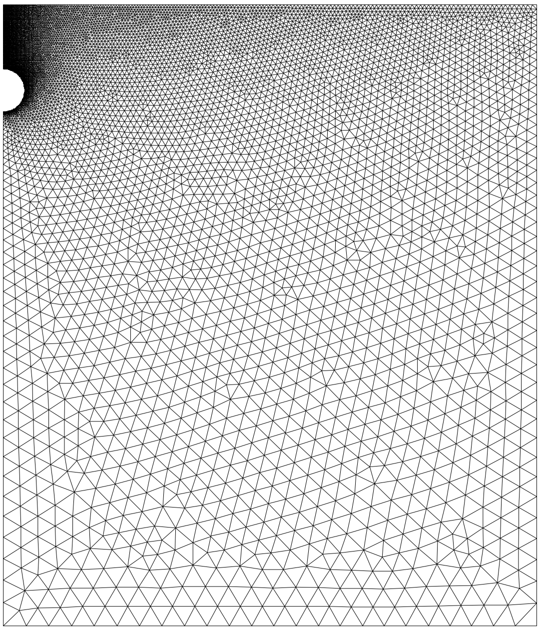

Figure 6.1.2. Spatial discretisation of the problem. The mesh is composed of 21457 triangular elements (11032 nodal points) and refined near the chamber and at the surface. Boundaries with prescribed displacements are located 25Km away from the chamber in order to make negligible the influence of boundary conditions on the solution.

---

[1] For simplicity, only constant overpressures will be considered here. However, if overpressures are time-dependent, the only change that must be taken into account is to take the Laplace transform of this boundary condition accordingly.

In case A the layer undergoes relaxation type 2 (i.e. the upper crust behaves as a Maxwell solid in both the deviatoric and the normal stresses) while in case B the layer follows relaxation type 3 (i.e. the upper crust behaves as a Maxwell solid in the deviatoric stresses and as a SLS in the normal ones). The underlying half-space simulates the lower crust and is always considered to relax following relaxation type 1 (i.e. behaves as a Maxwell solid in the deviatoric stresses and as an elastic material in the normal ones).

Figure 6.1.2 shows the spatial discretisation of the problem. The mesh is made up with 21457 triangular linear elements (11032 nodal points) and refined both near the Earth's surface and at the vicinity of the magma chamber.

Figures 6.1.3 and 6.1.4 show the obtained displacements around the chamber and at the Earth's surface respectively for different time instants. Time is given in terms of the characteristic time t [1]. Note from these figures how relaxation 2 induces higher deformations than relaxation 3. However, the type of relaxation does not change significantly the deformation pattern. Figure 6.1.5 shows the components of the stress tensor around the chamber at t=0 (elastic stresses) and after a characteristic time. Despite stresses are time dependent, it is difficult to appreciate these changes from this figure. Nevertheless, these changes can be appreciated from figure 6.1.6, where the stress component S_{rr} is plotted (at the Earth's surface) versus radial distance. The rest of the stress components show a similar trend at the surface except, of course, S_{rz} which is always zero (free surface).

---

[1] The relation between this characteristic time and the physical time depends on the viscosity of the media. See equation (4.5.22).

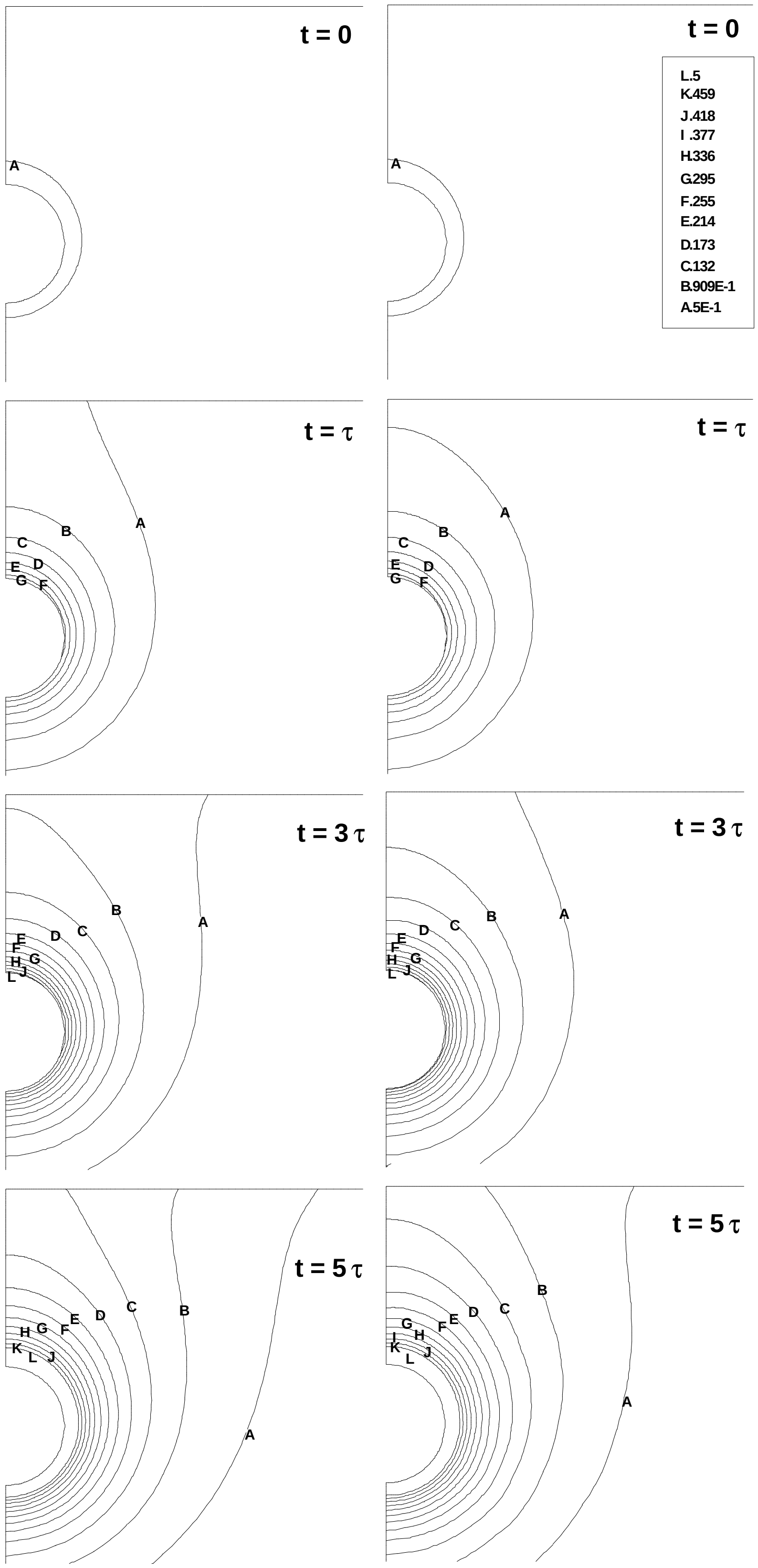

Figure 6.1.3. Total displacement (in m) at different characteristic times τ. Results around the chamber for the cases A (left column) and B (right column). Solutions at *t*=0 coincide with the elastic case.

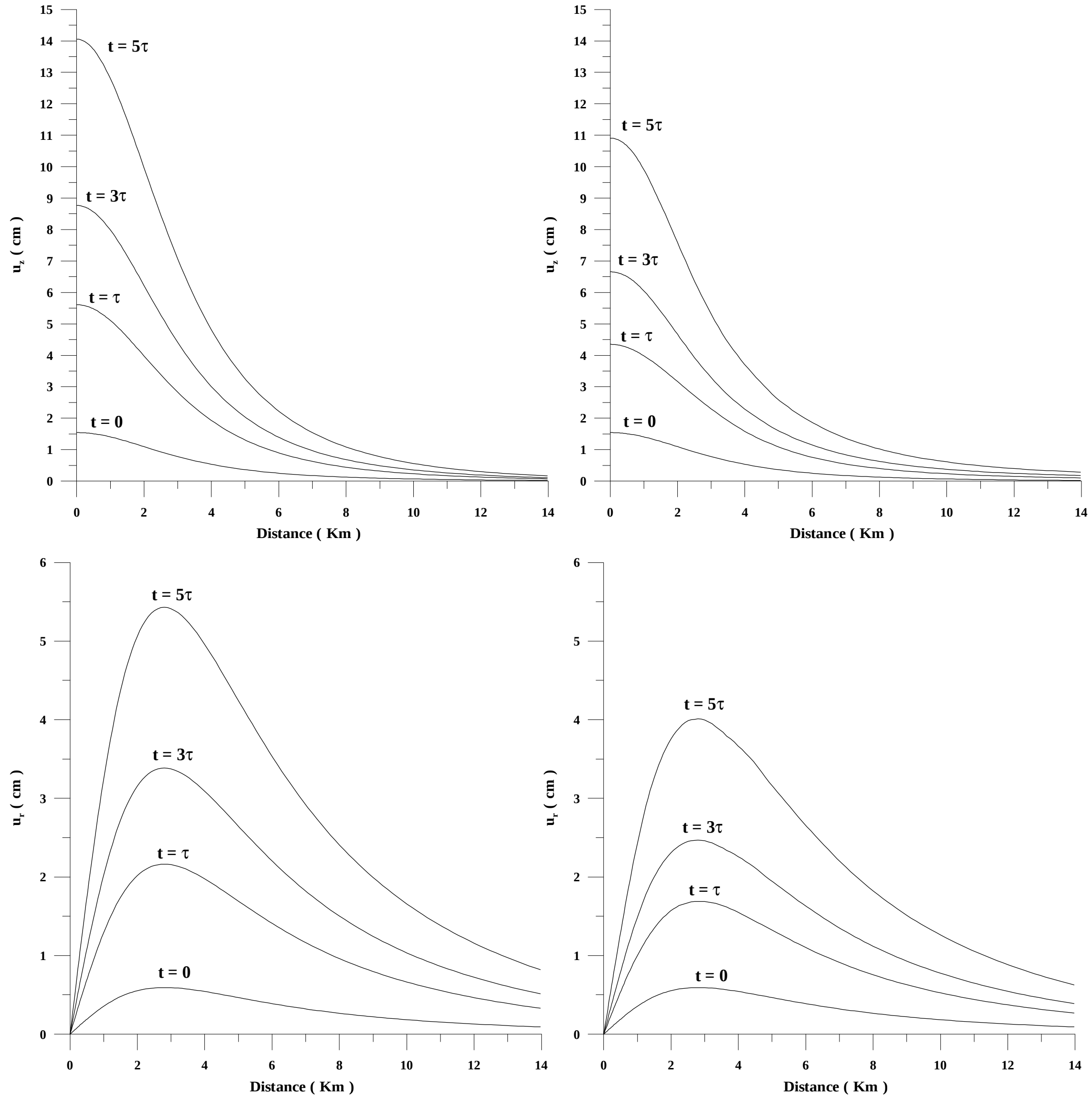

Figure 6.1.4. Vertical u_z (top) and radial u_r (bottom) displacements (in cm) at the Earth's surface versus distance (in Km) for different characteristic times τ and for the cases A (left column) and B (right column). The origin is always located at the symmetry axis.

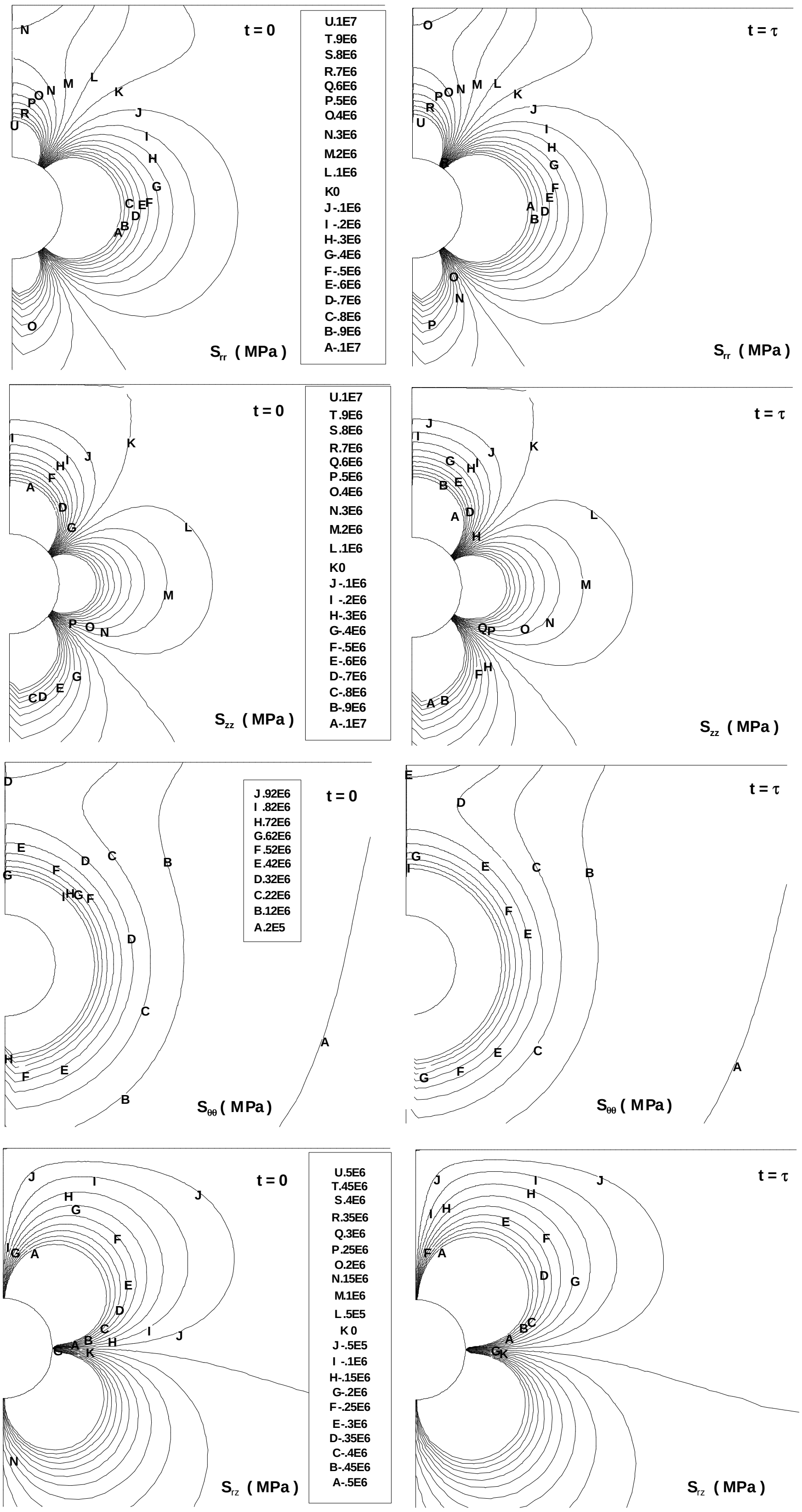

Figure 6.1.5. Components of the Cauchy stress tensor (S_{rr} , S_{zz} , S_{qq} and S_{rz} in MPa from top to bottom) for the case A. Left: results at *t*=0. Right: results after a characteristic time τ. Positive stresses indicate traction and negative stresses indicate compression.

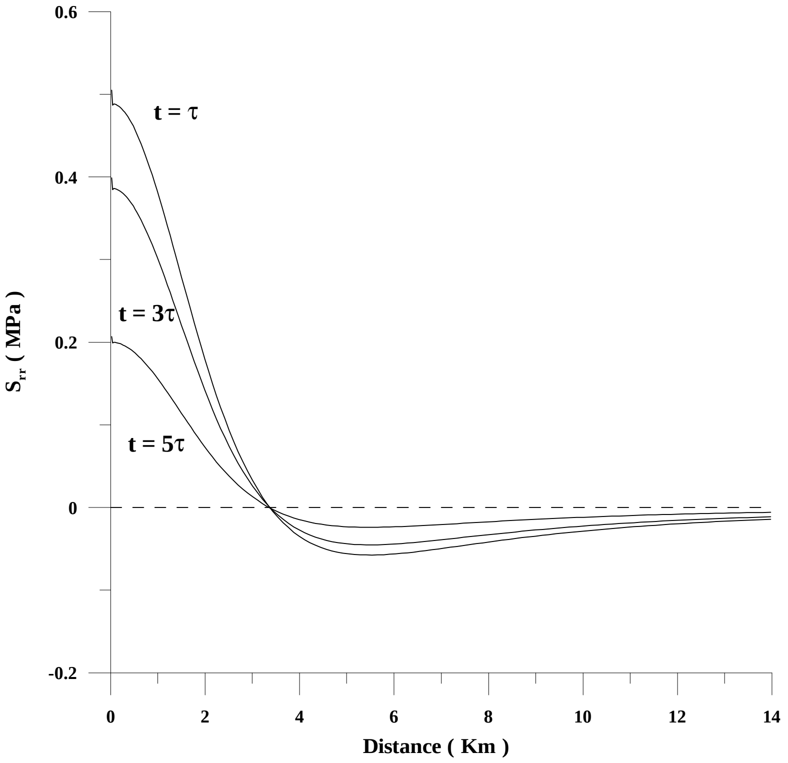

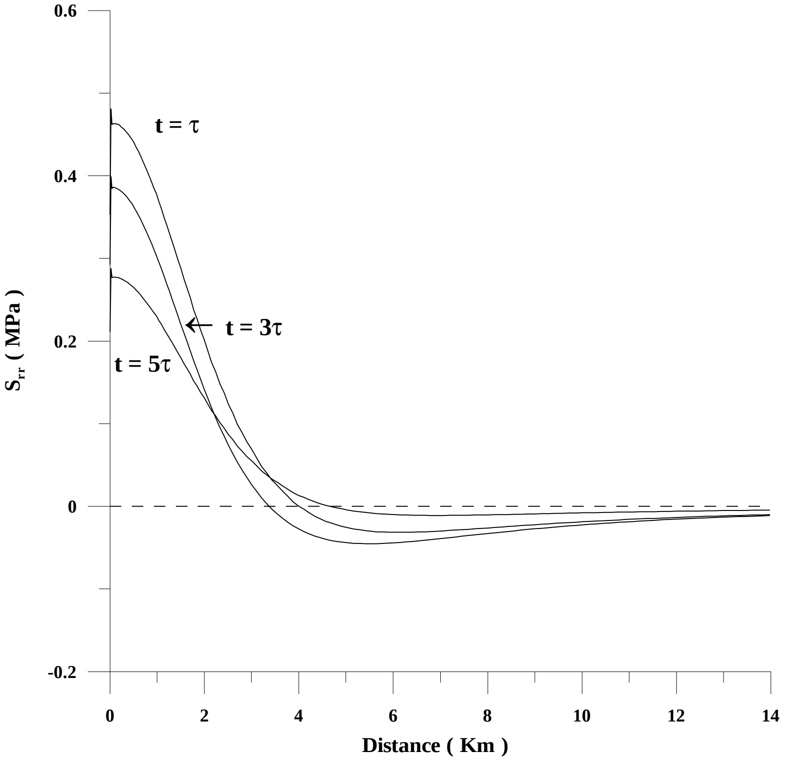

Figure 6.1.6. Stress component S_{rr} (in MPa) at the Earth's surface versus radial distance (in Km) and at different characteristic times for the cases A (top) and B (bottom). Note the temporal dependence of the stress field.

6.2 A Comparison between Point and Extended Sources. Constrains on the Analytical Solutions

So far, all the models available in the literature to compute viscoelastic ground deformations in volcanic areas are analytical, i.e. they assume both a point source of pressure and a flat surface. Despite the advantages of these models, it is well known from the purely elastic case that the assimilation of the magma chamber with a point of dilatation implicitly assumes that the dimension of the body is small compared to its depth. In other words, the applicability of these analytical solutions is constrained to those cases where $e \to 0$, being $e \equiv b/h_c$ the chamber size to depth ratio (see figure 6.1.1). The objective of this section is to compare analytical (point source) and numerical (extended source) solutions at surface in order to constrain and quantify the error produced by the point source hypothesis. Surface displacements produced by the viscoelastic response depend on several parameters such as size, depth and shape of the chamber. As in [*Folch et al.*, 2000], different tests have been performed in order to evaluate the influence of these parameters on the viscoelastic solution as well as the validity of the point source hypothesis. In each test, all the parameters except the one which is under study are fixed to the "standard" values in order to analyse the effect of the changing parameter on the solution. Whichever the case, the elastic Young modulus is 75GPa, the Poisson ratio is 0.25 (then both Lamé parameters are 30GPa), the overpressure inside the magma chamber is 10MPa and the relaxation is of type 2. The standard values employed in the tests are summarised in table 6.2.1. Viscoelastic solutions are given in terms of the characteristic time τ, so that some value for the viscosity of the crust must be necessarily assumed for practical applications.

Parameter	Standard value
Chamber depth h_c $(= H_{cha} + b)$	3 Km
Major axis a	1 Km
Minor axis b	1 Km
Slope of the volcano edifice a	0^o

Table 6.2.1. Standard values used in the tests. In all the cases, the Lamé parameters are 30GPa, the chamber overpressure is 10MPa and the relaxation is type 2.

Numerical solutions are obtained as exposed in section 4.5.2. The meshes used in the tests, quite similar to that shown on figure 6.1.2, are made up with bilinear triangular elements and, on average, are composed of 20000 elements (10000 nodal points). Analytical solutions are obtained using the method originally proposed by Dr. J.B. Rundle [*Rundle*, 1980; *Rundle*, 1982] and successively refined by his co-workers (e.g. [*Fernández and Rundle*, 1994; *Fernández et al.*, 1997; *Fernández et al.*, 1998]). Present versions of this method are, doubtless, the most complete analytical methods to compute gravity changes and viscoelastic deformations due to a magmatic intrusion in a multilayered crust. Viscoelastic solutions are obtained from the elastic ones employing the correspondence principle together with the Prony series method[1]. In turn, elastic solutions (at surface) for the case of a stratified half-space composed by homogeneous layers are derived using the dislocation theory and the propagator matrix technique (see the above references for a major description). Analytical results have been obtained using *vis2vis*, a program developed and written by Dr. J. Fernández. It has been checked that numerical errors in the elastic solution at surface are in the range, or lower than, 1/1000 by performing a remeshing and moving aside the margins of the computational domain. This is an important point because, as the objective is to quantify the errors in the point source hypothesis by comparing analytical and numerical results, one must be sure that numerical solutions are "error free". With this margin of tolerance, the only numerical errors in the viscoelastic solution will come from the procedure employed to perform the Laplace inversion (the Prony series method). However, note that this errors are, in principle, the same for both analytical and numerical procedures. In summary, assuming that the obtained numerical results are "exact", the difference numerical-analytical provides in a straightforward way the absolute error of the point source hypothesis.

6.2.1 Influence of the Size to Depth Ratio

Firstly, the effect of the size to depth ratio ε has been analysed considering two series of tests in which the size of a spherical chamber as well as its depth are respectively varied[2]. The rest of the parameters involved are held constant. Figures 6.2.1 and 6.2.2 show, respectively, vertical and radial numerical (i.e. extended source) and analytical (i.e. point source) displacements at surface for chambers with radius of 0.5, 1.0, 1.5 and 2 Km. Since in all the cases chamber depth is h_c=3Km, the corresponding values of ε are 0.16, 0.33, 0.50 and 0.66. Analogously, figures 6.2.3 and 6.2.4 show the same results but for chambers with a constant radius b=a=1Km and located at changing depths of 3.0, 6.0 and 9.0 Km. The point to point difference between numerical and analytical results (i.e. the absolute error of the analytical

---

[1] Note that, in fact, the method developed in this work is nothing but a "numerical version" of this analytical procedure.

[2] Analytical solutions depend on the intensity of the source which, in turn, can be related to the chamber size. In consequence, and despite the point source hypothesis, these analytical solutions are, in fact, dependent on the size of the chamber.

procedure) is reflected on figures 6.2.5 and 6.2.6. It can be observed from these figures how, as in the elastic case (e.g. [*Dieterich and Decker*, 1975]), analytical and numerical solutions tend to converge for small values of ε but, in contrast, when ε increases appreciable discrepancies appear. For small ε values ($e \leq 0.25$), the differences are negligible (in the millimetric range or even lower), for medium ε values ($0.25 \leq e \leq 0.5$) fall in the centimetric range, being 5-20% of the maximum displacement in both radial and vertical components and, finally, for large ε values ($e \geq 0.5$) the discrepancies are greater than 30% and can have, in some cases, an absolute value in the metric range. However, it should be pointed out that, in nature, such large values of ε are uncommon (if not unexistent) so that, for most practical cases, the point source hypothesis is likely to induce relative errors in the range or lower than 20%. When ε is small, the absolute value of the difference between both solutions is very similar to that of the elastic case (the solution at t=0) but, as ε approaches to 1, this absolute value increases with time. Nevertheless, it can be observed how, whichever the ε value, the relative error decreases for long values of the characteristic time despite the absolute difference between both solutions may increase.

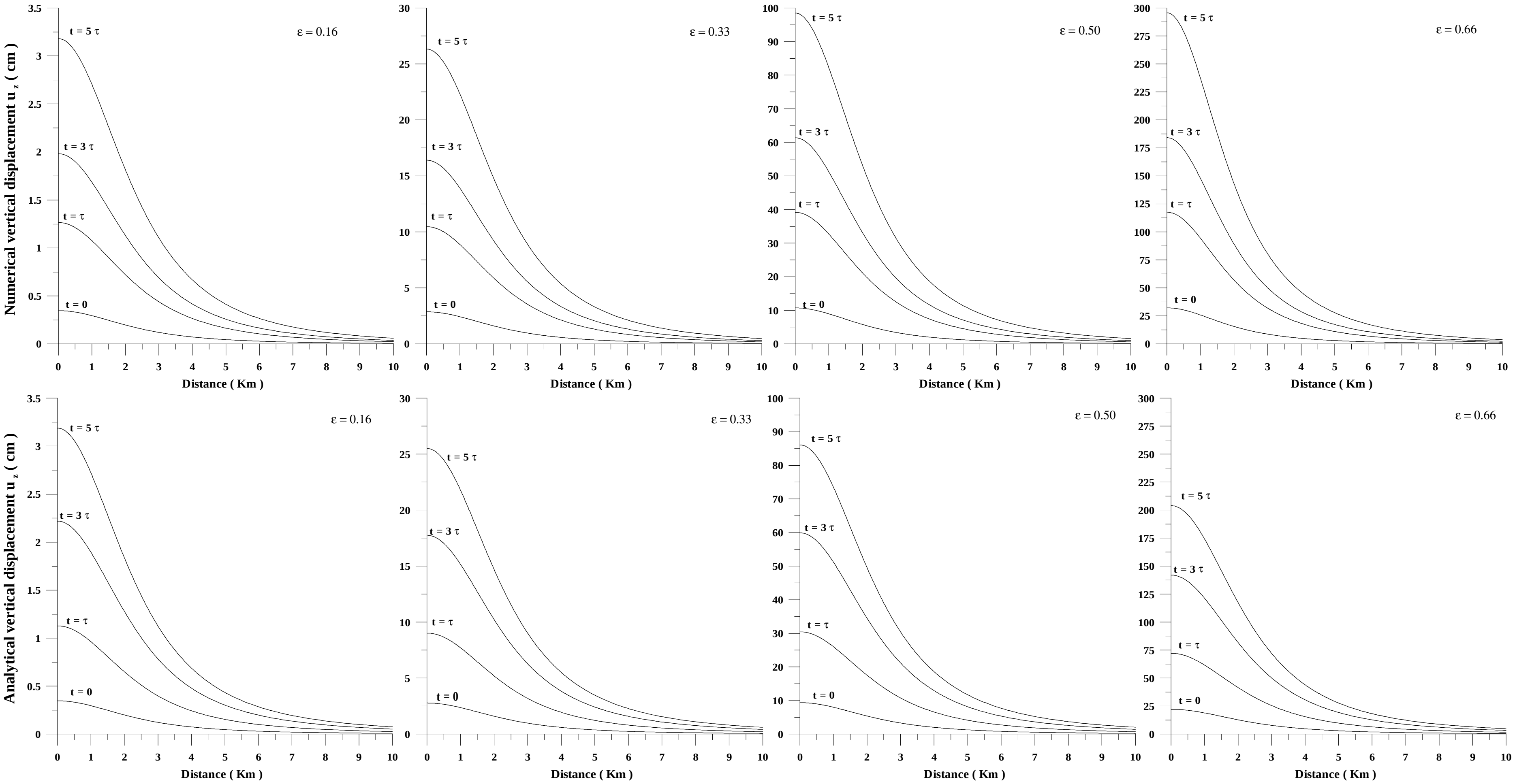

Figure 6.2.1. Comparison between numerical (extended source) and analytical (point source) vertical displacements plotted versus radial distance to the symmetry axis. Results for spherical chambers with h_c=3Km and different radius of 0.5, 1.0, 1.5 and 2 Km from left to right respectively. Note the different predictions of both procedures as ε increases.

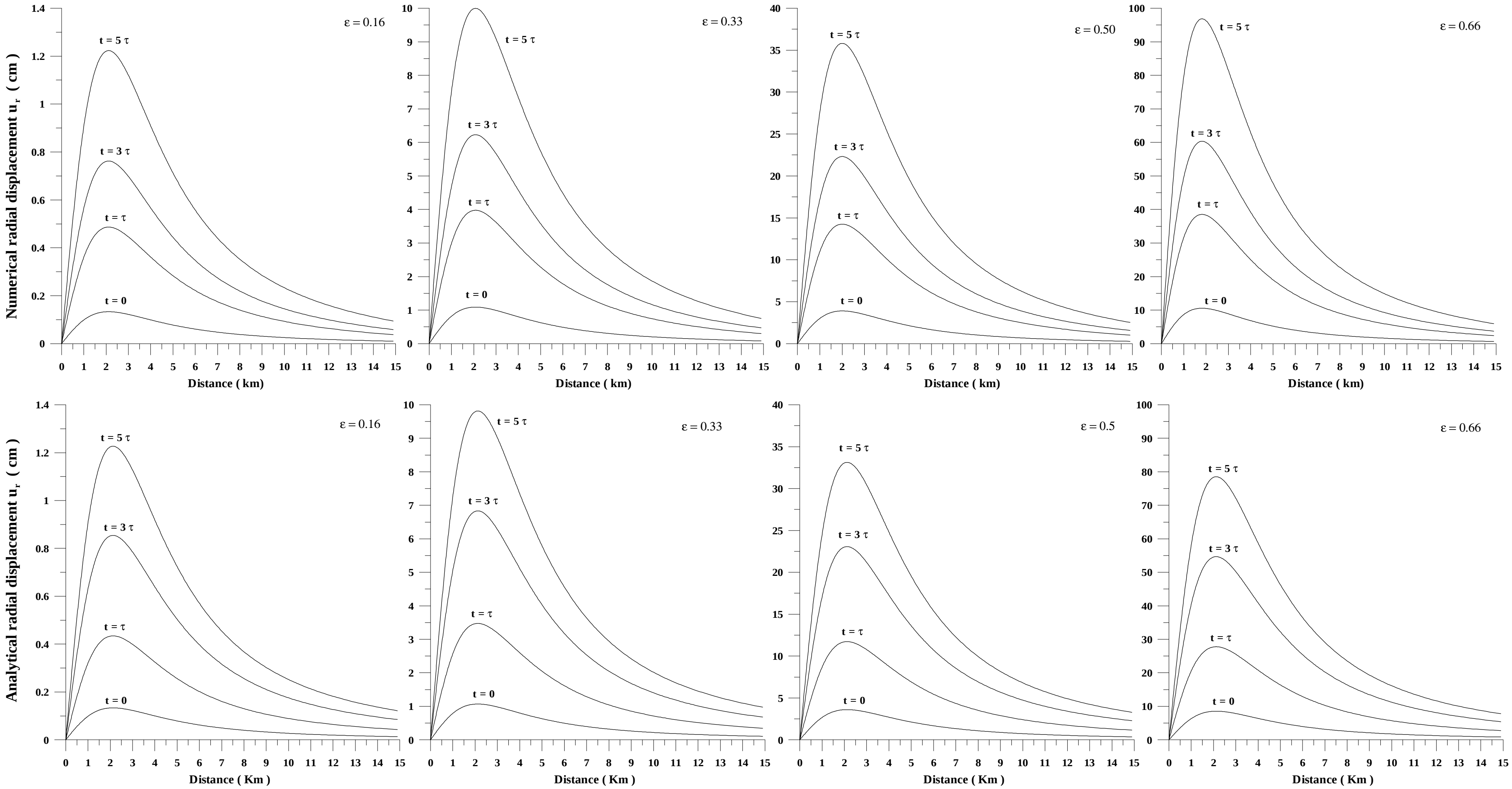

Figure 6.2.2. Comparison between numerical (extended source) and analytical (point source) radial displacements plotted versus radial distance to the symmetry axis. Results for spherical chambers with h_c=3Km and different radius of 0.5, 1.0, 1.5 and 2 Km from left to right respectively. Note the different predictions of both procedures as ε increases.

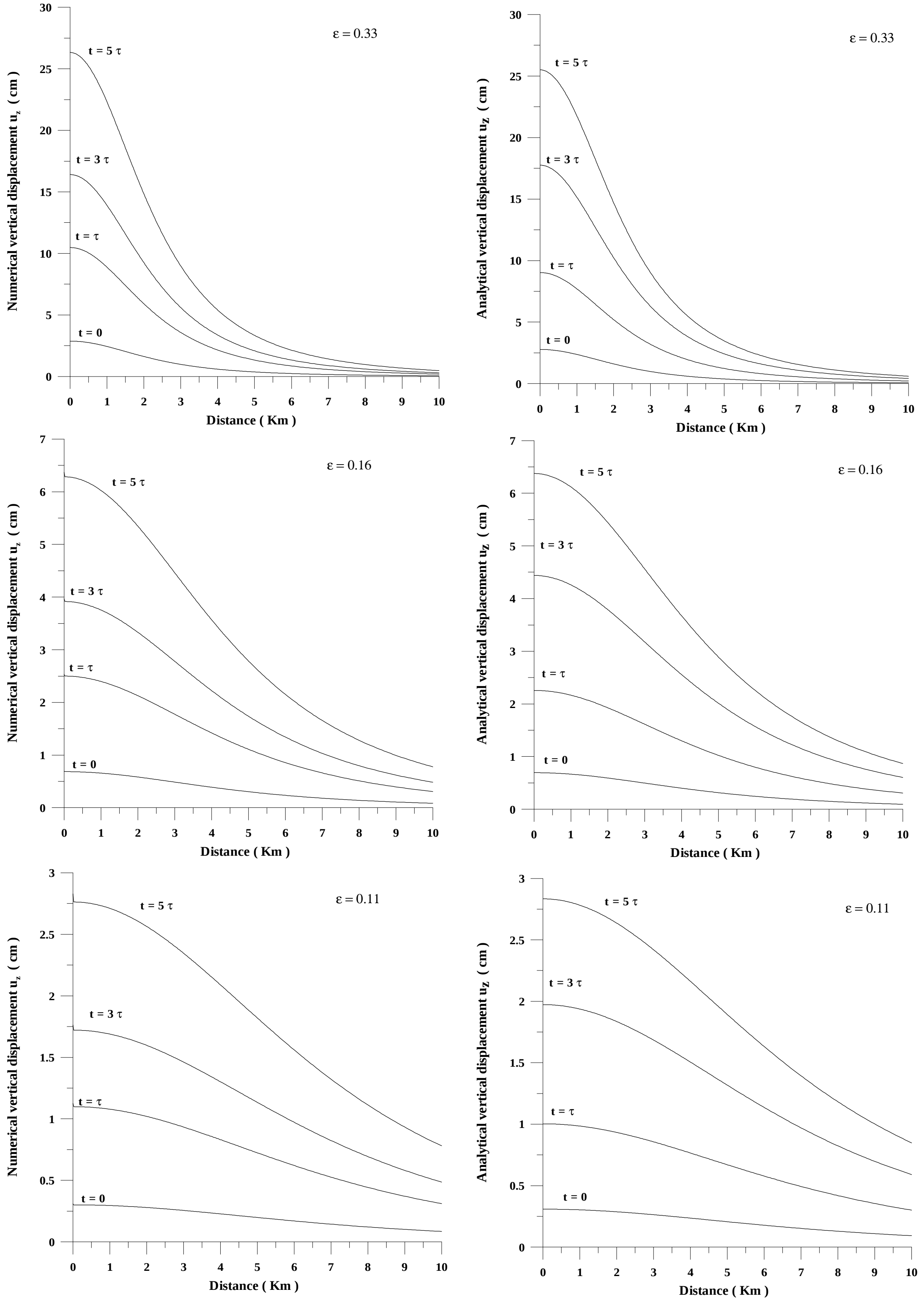

Figure 6.2.3. Comparison between numerical (extended source) and analytical (point source) vertical displacements u_z plotted versus radial distance. Results for chambers with a=b=1Km and located at different depths of h_c=3, 6 and 9 Km from top to bottom respectively.

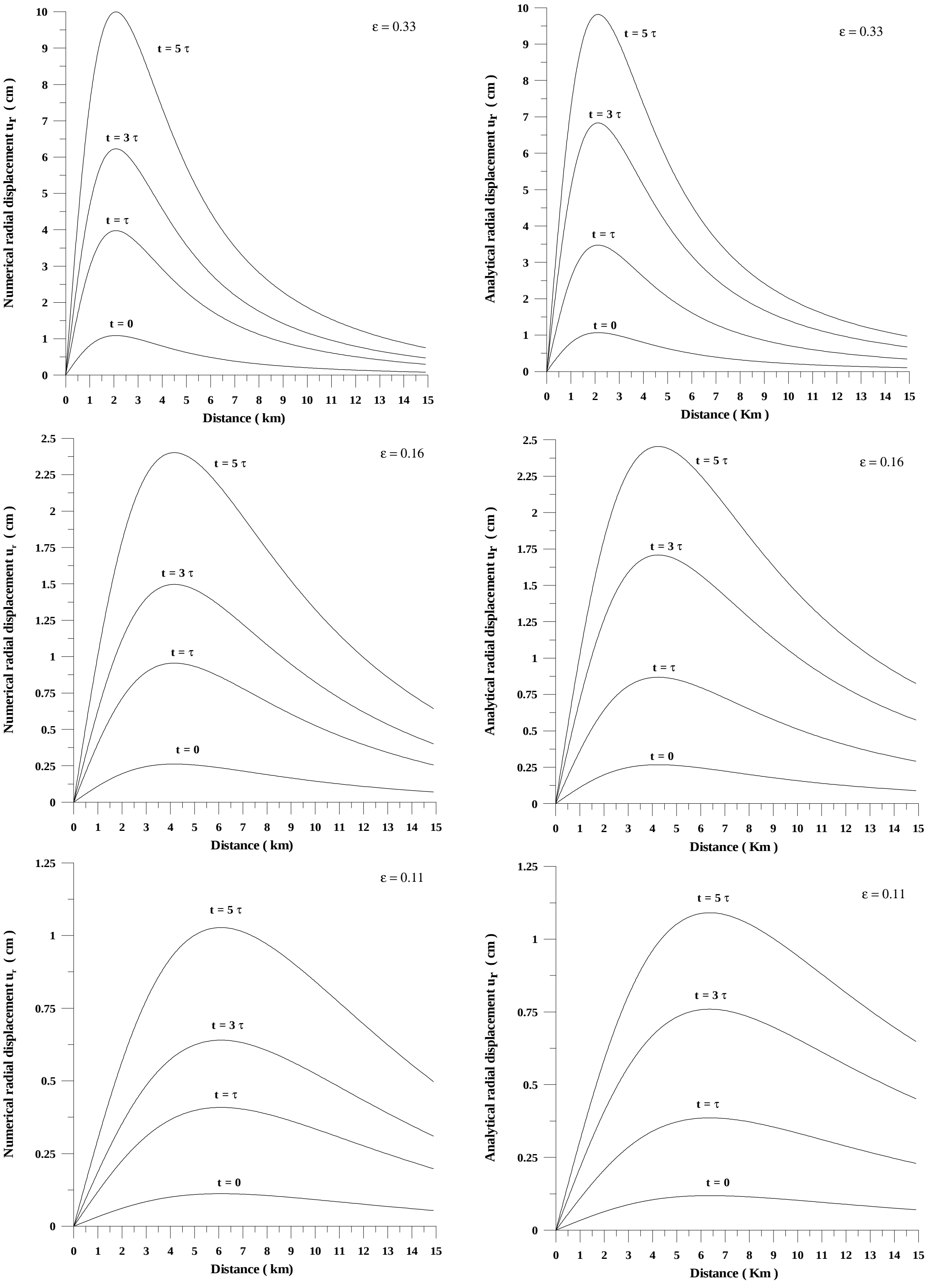

Figure 6.2.4. Comparison between numerical (extended source) and analytical (point source) radial displacements u_r plotted versus radial distance. Results for chambers with *a*=*b*=1Km and located at different depths of h_c=3, 6 and 9 Km from top to bottom respectively.

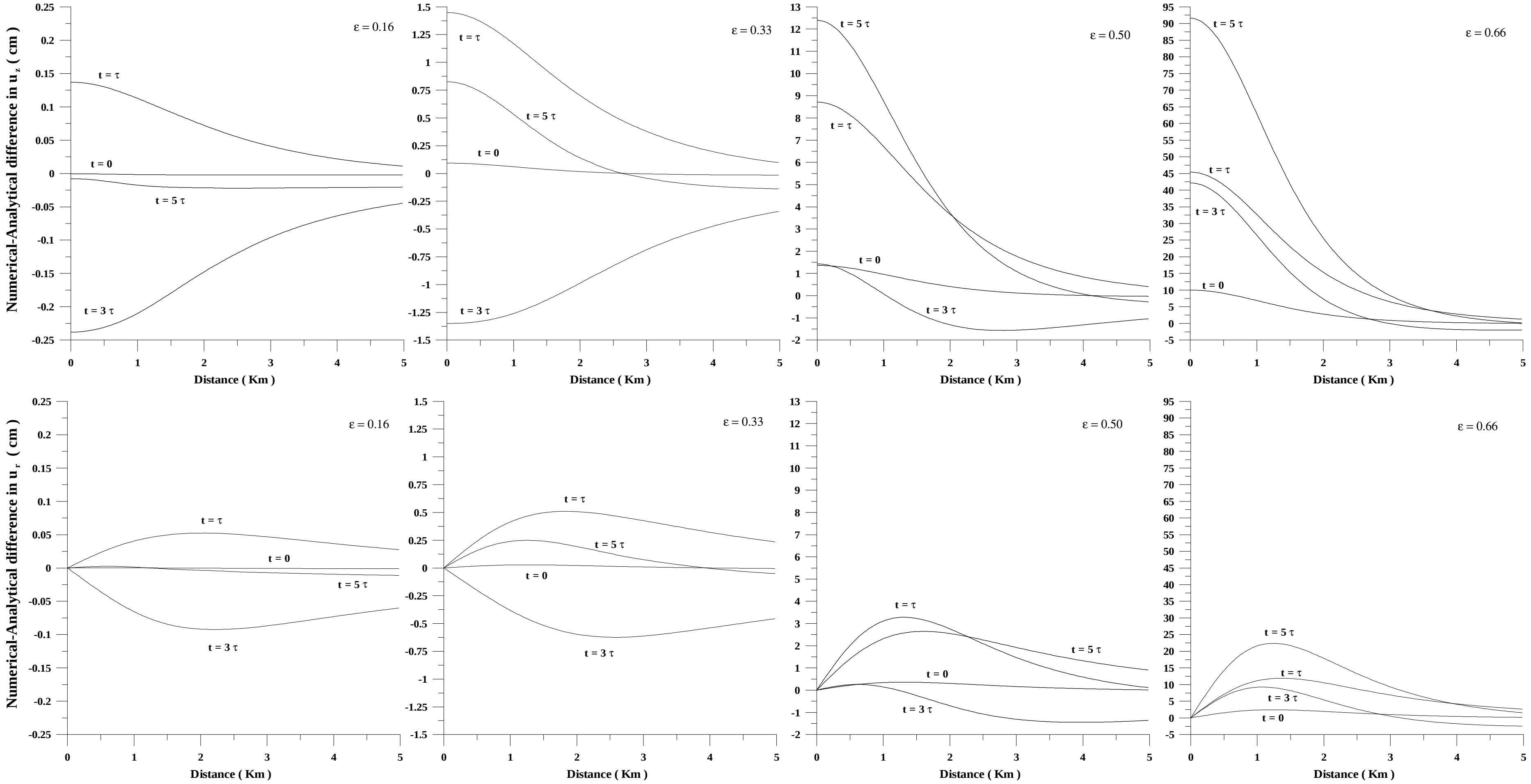

Figure 6.2.5. Top: numerical (extended source) minus analytical (point source) vertical displacements u_z plotted versus radial distance and for different characteristic times. Results for spherical chambers with h_c=3Km and different radius of 0.5, 1.0, 1.5 and 2.0 from left to right respectively. Bottom: the same for radial displacements u_r.

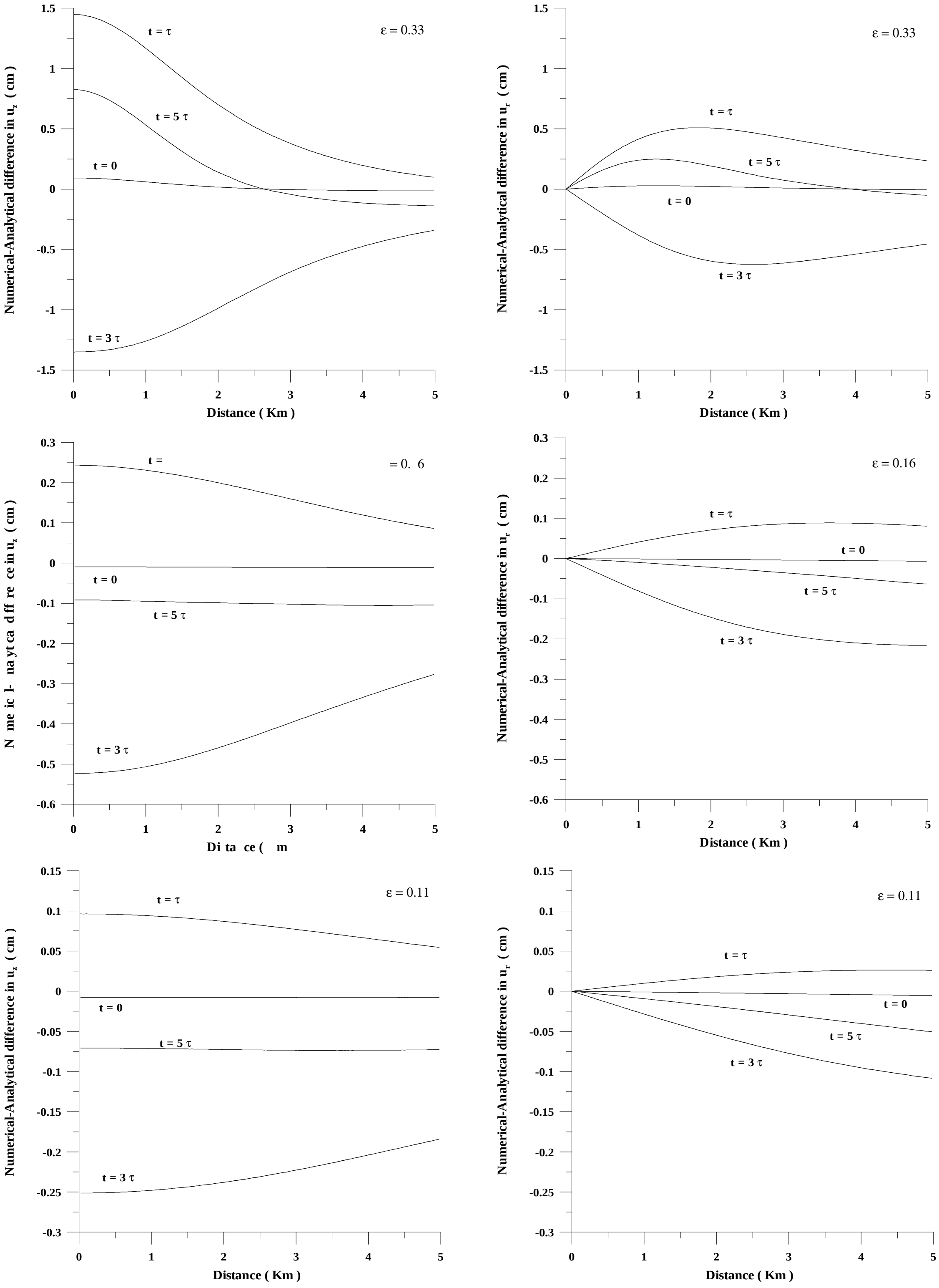

Figure 6.2.6. Left: numerical (extended source) minus analytical (point source) vertical displacements u_z plotted versus radial distance for different characteristic times. Results for spherical chambers with a=b=1Km placed at different depths of h_c=3, 6 and 9 Km from top to bottom respectively. Right: the same for radial displacements u_r.

6.2.2 Influence of the Topography

Next series of tests consider the effect of the topography. Obviously, topographic features are an exclusive characteristic of each particular volcanic complex but, as a first approximation, one can assume axisymmetrical volcanoes with different average slopes of the flanks. To date, analytical solutions are constrained to flat surfaces so that, in order to estimate the error produced when topography is neglected, numerical results should be compared with the case $a = 0^o$ (in this case, if ε is "sufficiently small", both solutions coincide). Figure 6.2.7 shows numerical vertical and radial displacements at surface considering different volcanic edifices with an average slope of 0° (flat surface), 10°, 20° and 30° (the heights of these volcanic edifices are, respectively, 0m, 1000m, 2000m and 3000m). In all cases, ε=0.33.

[*Cayol and Cornet*, 1998] have recently pointed out that, in the case of an elastic rheology, the interpretation of ground-surface displacements with half-space models (flat surface) can lead to erroneous estimations and that the steeper is the volcano, the flatter is the vertical displacement field. As observed from figure 6.2.7, these results are dramatically emphasised in the case of viscoelastic rheologies, where topography changes in a very important way both the magnitude and the pattern of the displacement field. Thus, neglecting the topographic effects may, in many cases, introduce an error greater than the one implicit in the point source hypothesis.

Observation The results shown in figure 6.2.7 are obtained using a constant value h_c=3Km, i.e. measuring the depth of the chamber from the "sea level". This is the standard procedure when topographic effects are considered. Another possibility could be to measure the depth of the chamber from the tip of the conical volcanic edifice, i.e. considering a constant value h_c+H_{con}=3Km (see figure 6.1.1). Despite being less common, this possibility has been also considered. Results are shown in figure 6.2.8.

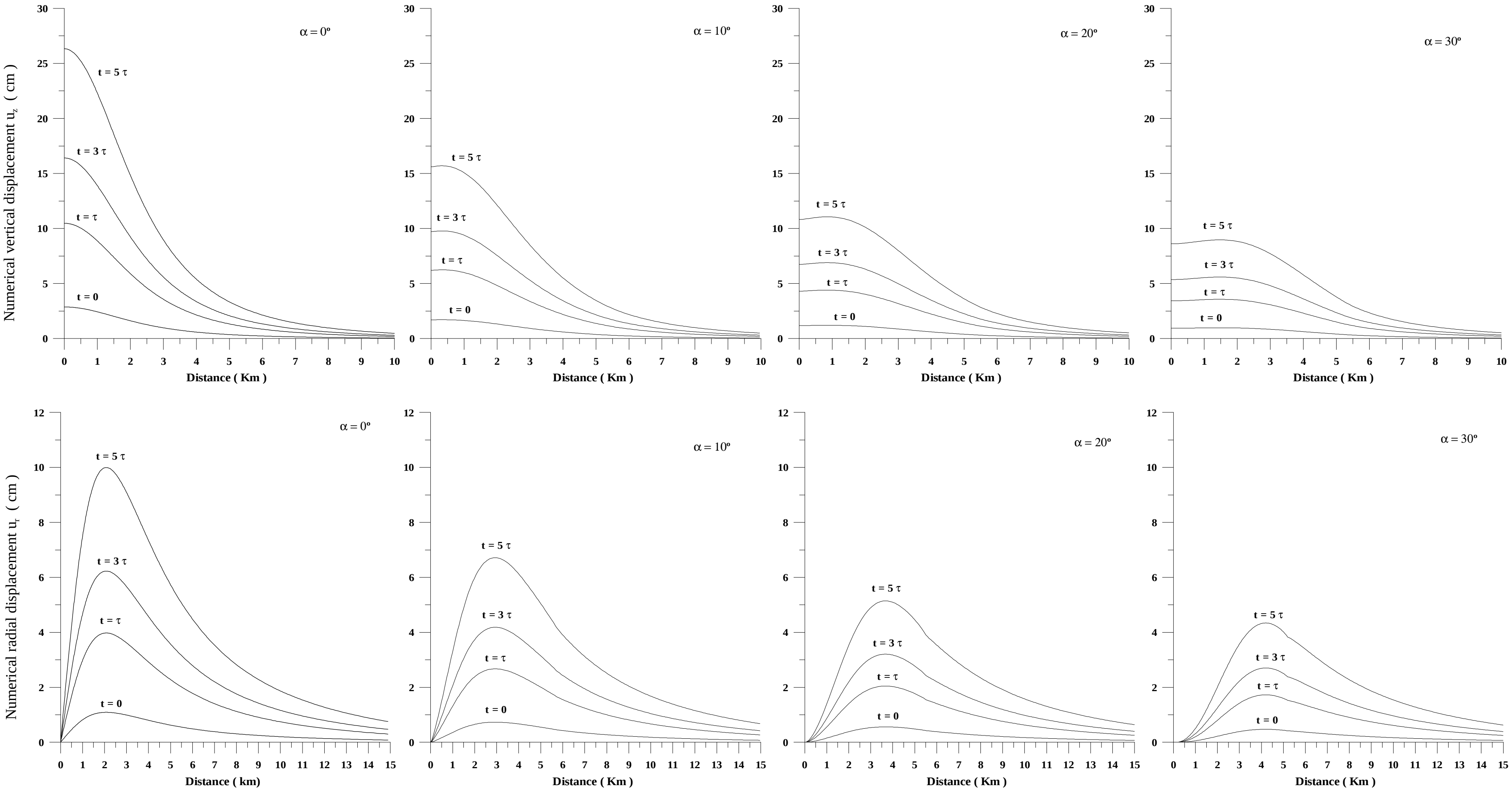

Figure 6.2.7. Numerical vertical displacements u_z (upper row) and radial displacements u_r (lower row) versus radial distance considering topographic effects. In all the cases, the chamber is spherical with a=1Km and h_c=3Km but considering a volcanic edifice with average slope of the flanks of 0º, 10º, 20º and 30º from left to right respectively.

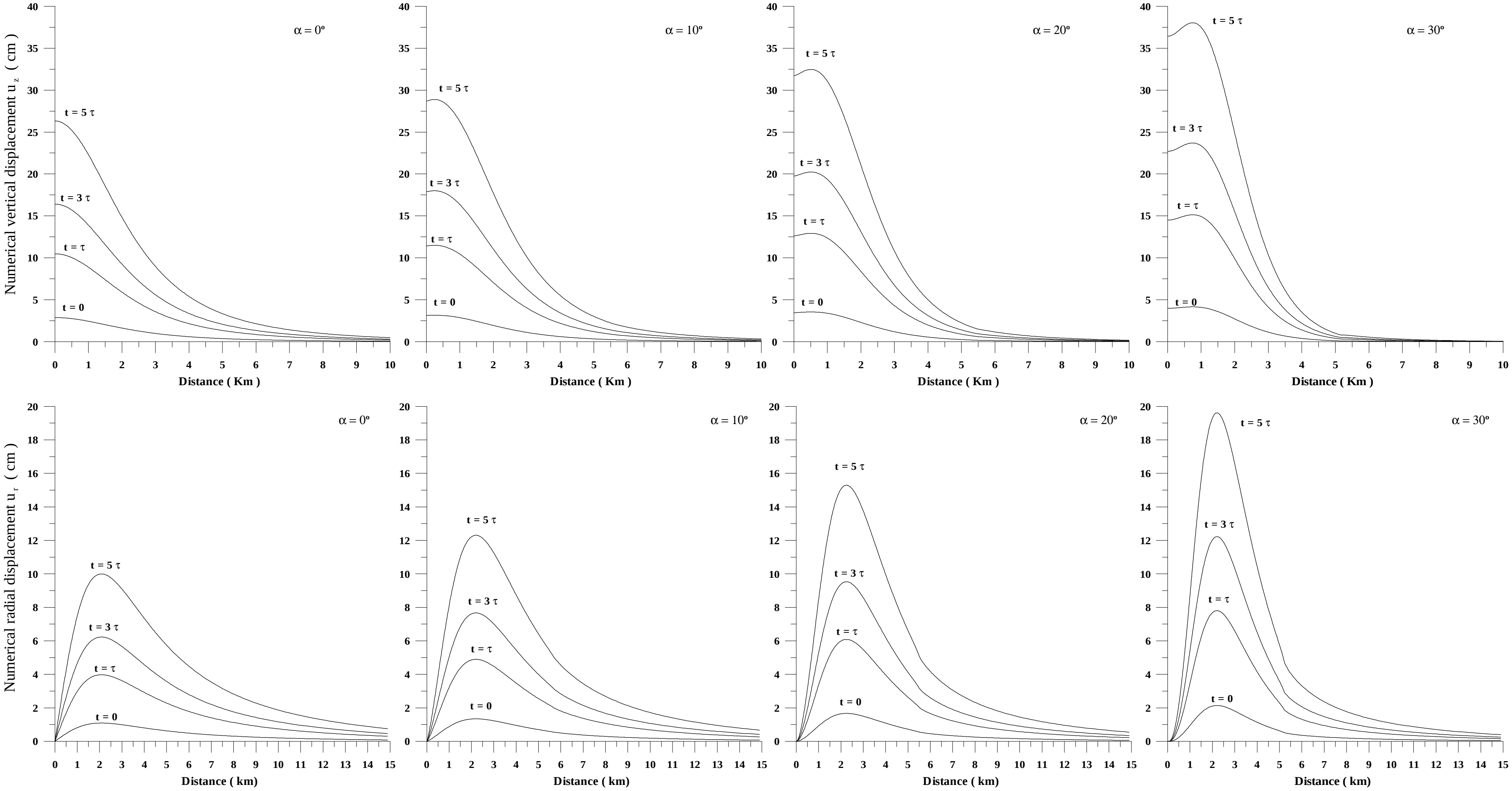

Figure 6.2.8. Numerical vertical displacements u_z (upper row) and radial displacements u_r (lower row) versus radial distance considering topographic effects. In all the cases, the chamber is spherical with a=1Km and h_c+H_{con}=3Km. Volcanic edifices with average slope of the flanks of 0º, 10º, 20º and 30º are considered.

6.2.3 Influence of the Chamber Shape

The last aspect tackled concerns the effect of chamber shape. In these series of tests, magma chambers are ellipsoidal, placed at 3Km depth and have a variable major axis *a* (the minor axis is always *b*=0.5Km). Note that, whichever the case, the value of ε is always the same (ε=0.16). Figures 6.2.9 and 6.2.10 show, respectively, vertical and radial displacements at surface for both numerical and analytical procedures and for chambers with major axis of 0.5, 1.0, 1.5 and 2Km (the corresponding eccentricities of the ellipsoids are 0, 0.86, 0.94 and 0.96). Finally, figure 6.2.11 reflects the differences between analytical and numerical results. In each case, analytical solutions have been obtained considering spherical sources with an equal volume (the equivalent radius are 0.5, 0.8, 1.04, and 1.26 respectively). For spherical chambers, analytical and numerical solutions give approximately the same result since ε is small. However, important discrepancies are observed when the eccentricity increases. As observed from the figures, differences higher than 100% can appear when the eccentricity of the chamber is neglected.

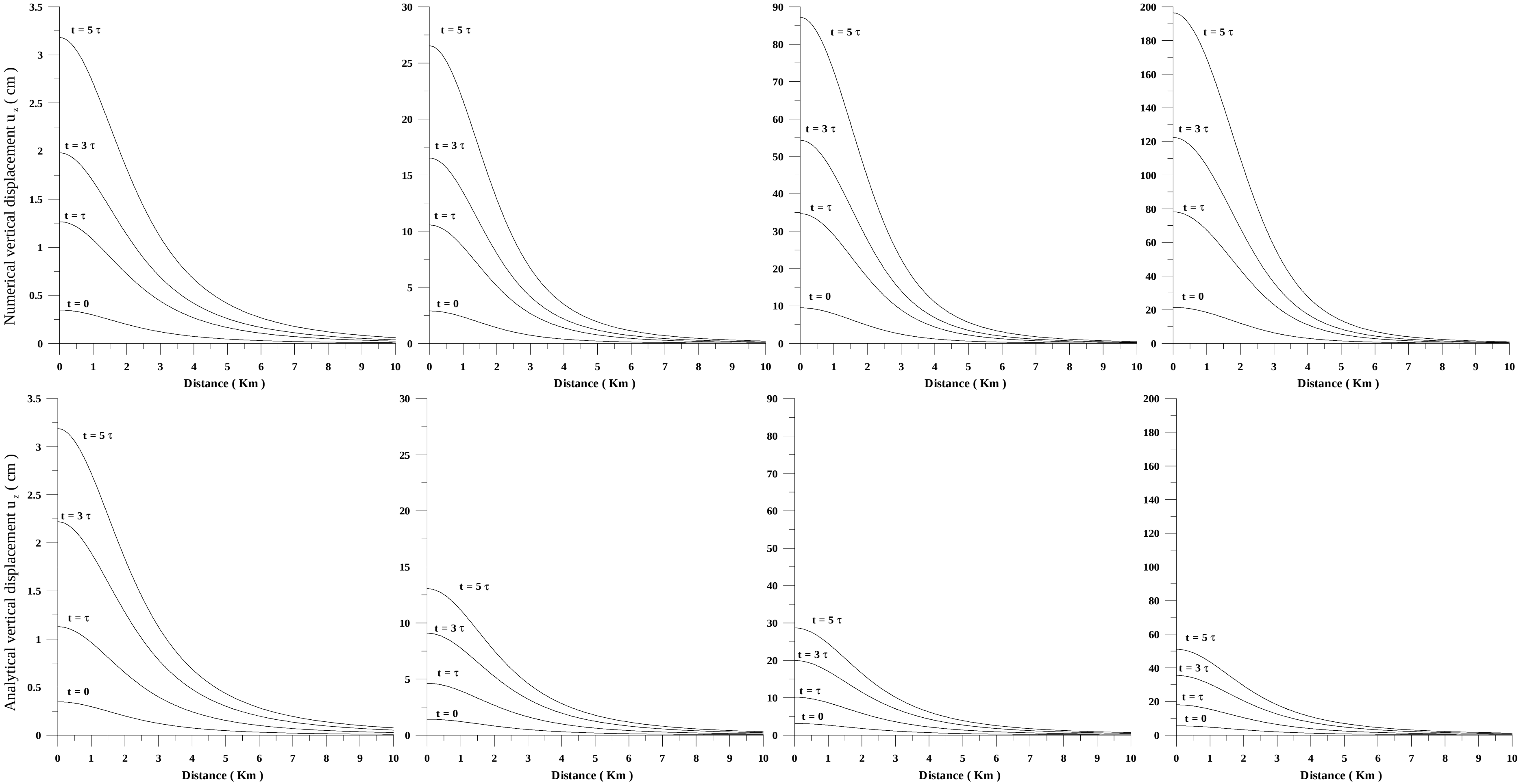

Figure 6.2.9. Top: numerical vertical displacement at surface plotted versus radial distance. Results for ellipsoidal chambers with h_c=3Km, minor axis b=0.5Km and different major axis a of 0.5, 1.0, 1.5 and 2.0 Km from left to right respectively. Bottom: same results using the analytical method but considering spherical sources with equal volume.

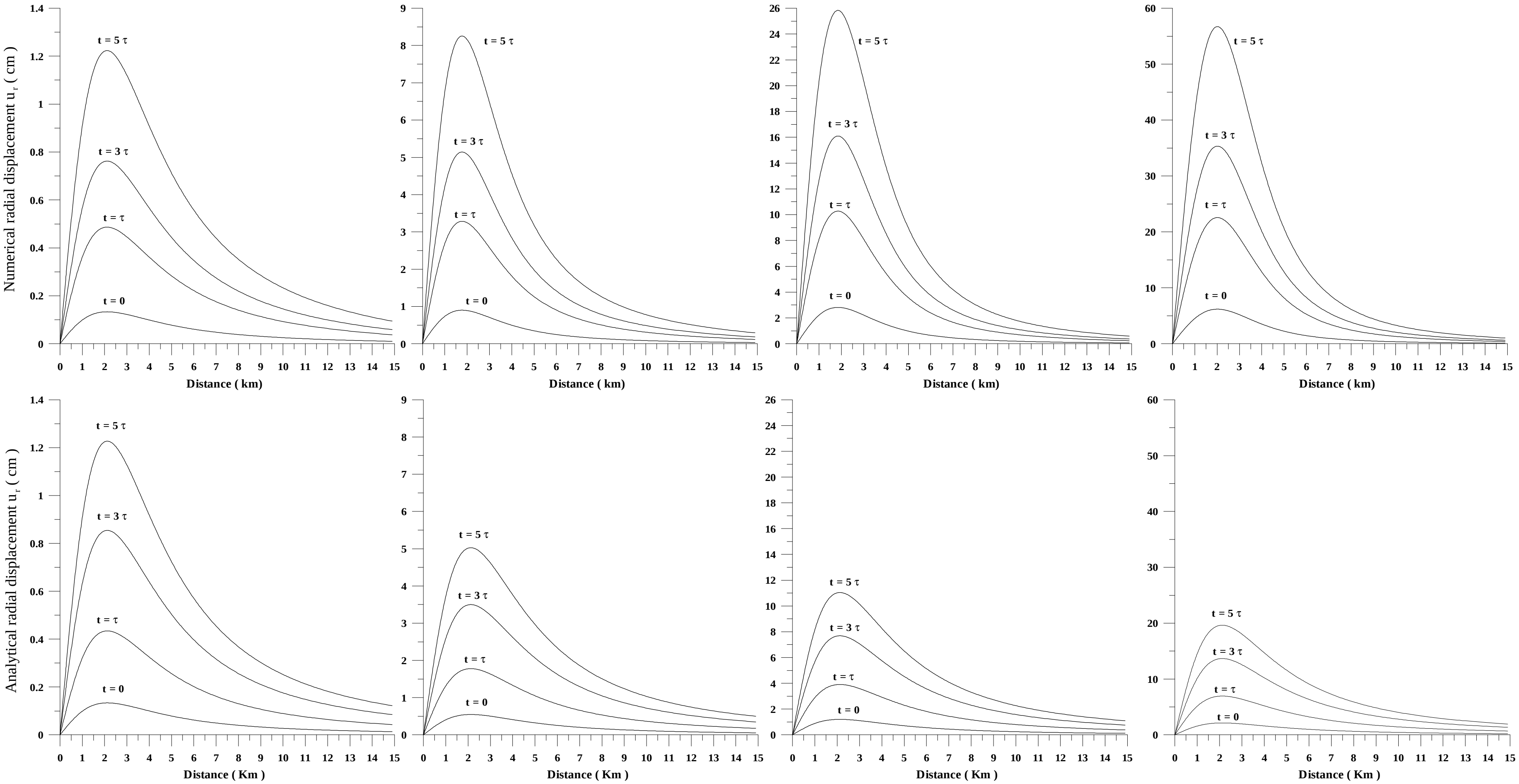

Figure 6.2.10. Top: numerical radial displacement at surface plotted versus radial distance. Results for ellipsoidal chambers with h_c=3Km, minor axis b=0.5Km and different major axis a of 0.5, 1.0, 1.5 and 2.0 Km from left to right respectively. Bottom: same results using the analytical method but considering spherical sources with equal volume.

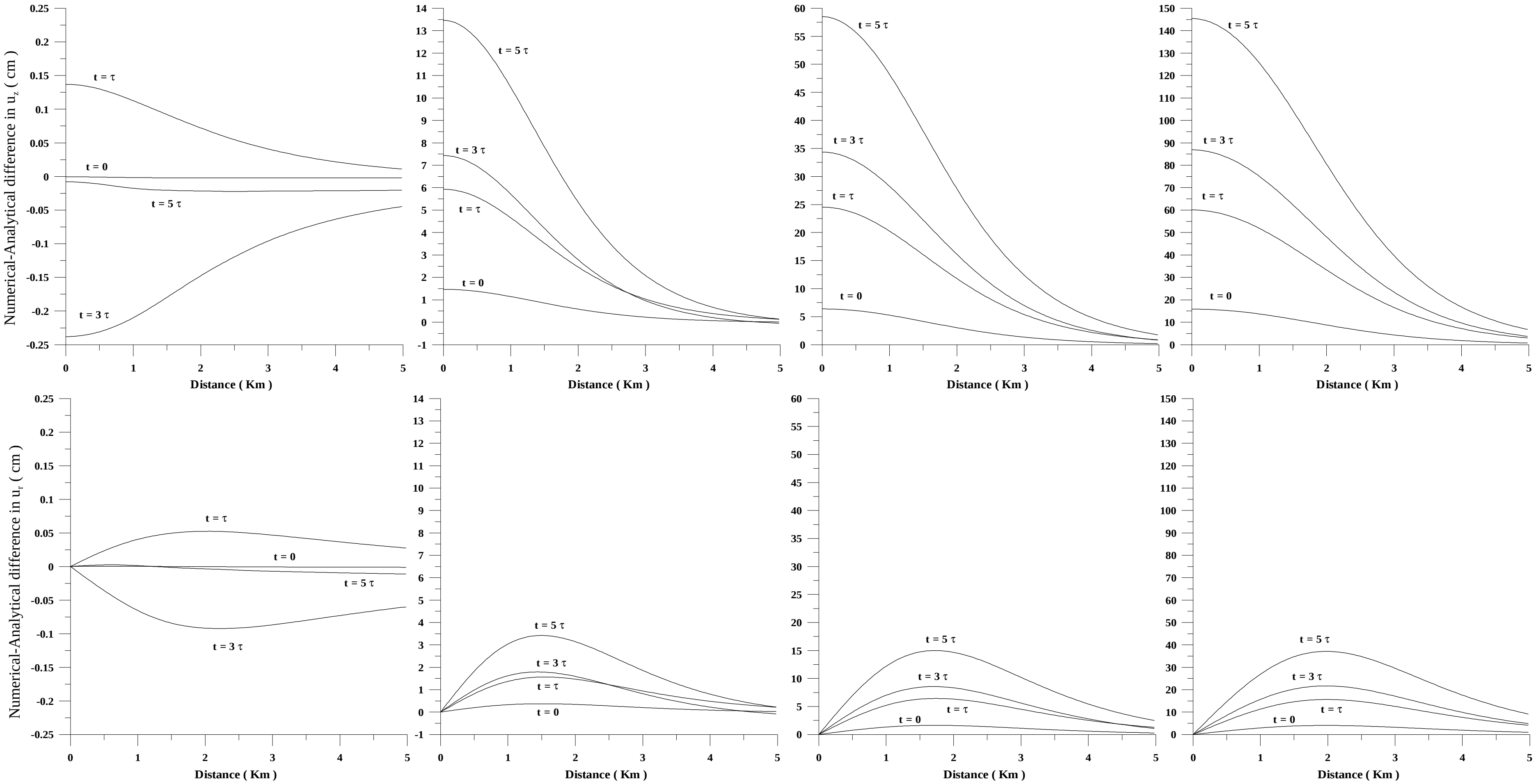

Figure 6.2.11. Top: numerical (extended source) minus analytical (point source) vertical displacements u_z plotted versus radial distance. Numerical results are for ellipsoidal chambers with h_c=3Km, minor axis b=0.5 and different major axis a of 0.5, 1.0, 1.5 and 2.0 from left to right respectively. For each case, analytical results assume spherical sources with and equal volume. Bottom: the same but for radial displacements u_r.

6.3 The 1982-1984 Campi Flegrei Uplift

The Campi Flegrei volcanic field is a roughly circular caldera complex of about 12 Km in diameter which is located near Naples, southern Italy. This caldera was formed about 35000 years ago after the Ignimbrite Campana eruption. Since then, the subsequent volcanic activity has been explosive and intracaldera, being the 1538 Monte Nuovo eruption the last eruptive event. Observations suggest that vertical ground movements have been operating at least during the last 2000 years [*Luongo et al.*, 1991]. During the period January 1982-September 1984 the area experimented a continuous uplift accompanied with seismic activity characterised by earthquakes of magnitudes up to 4.0. The average vertical growing rate during this period was 2 mm/day and the displacement reached a maximum value of 160 cm at the town of Pozzuoli, located at the centre of the caldera. The uplift profile decreased smoothly outwards from Pozzuoli and practically vanished at about 6 Km, at the edge of the caldera [*Berrino et al.*, 1984]. This dynamic evolution of the area was precisely monitored by a network of apparatus that measures ground deformations in Campi Flegrei since 1970 (see figure 6.3.1).

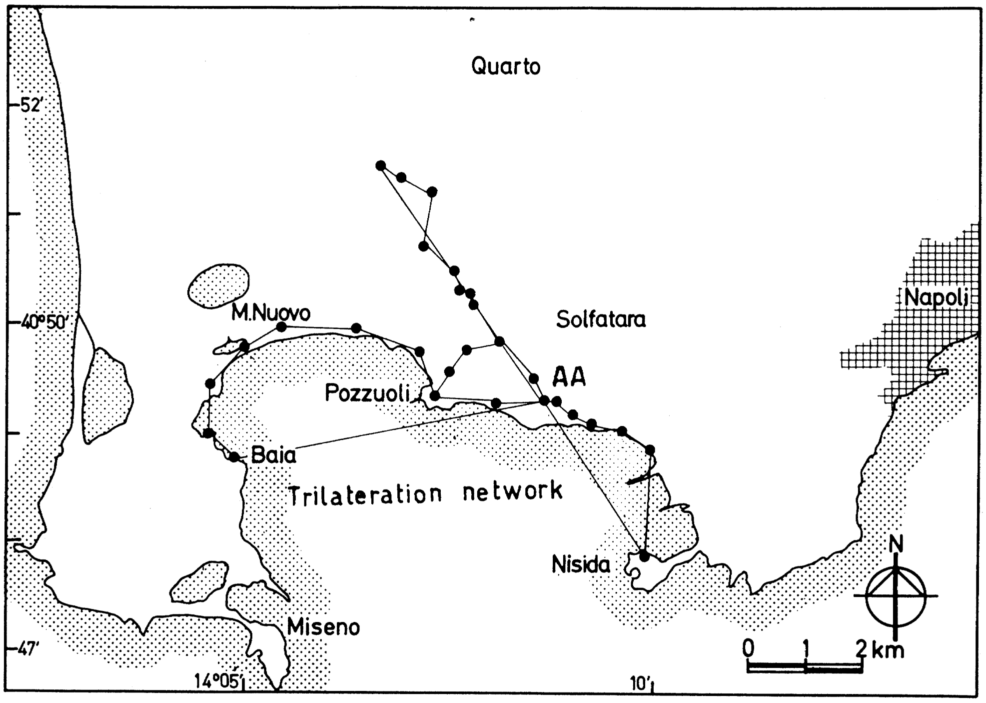

Figure 6.3.1. General view of the area of Campi Flegrei. The caldera is about 12 Km in diameter, nearly circular and with the centre located at the town of Pozzuoli. Dots indicate the monitoring system which measured the 1982-1984 ground uplift episode. Extracted from [*Berrino et al.*, 1984].

Figure 6.3.2 shows the measured vertical displacements versus distance during this uplift episode. This uplift episode pointed out that modelling of ground deformations considering elastic properties for the crust cannot always reproduce the observed uplifts unless unrealistic high pressures are assumed, and gave rise to a series of models with viscoelastic rheologies (see section 2.4.2 for major details).

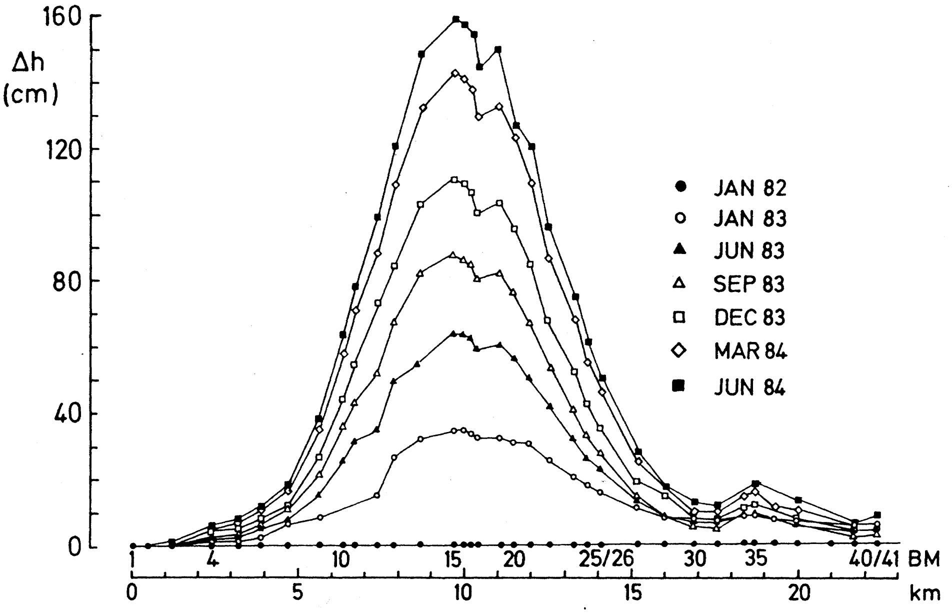

Figure 6.3.2. Measured vertical displacements (in cm) versus distance along the coastline (in Km) during the January 1982-June 1984 uplift episode. The reference level is January 1982. The point of maximum uplift centres on the town of Pozzuoli, and the uplift virtually vanishes at the edge of the caldera, about 6-7 Km away from its centre. Extracted from [*Berrino et al.*, 1984].

To illustrate the applicability of the model herein proposed with a real natural example, this section models the 1982-1984 uplift event following the original work of [*Bonafede et al.*, 1986; *Bonafede*, 1990]. It is important to keep in mind that, due to the assumptions and simplifications of the model (axial symmetry, depth independent properties, neglection of faults and discontinuities, etc.) one can expect only to reproduce the measured data qualitatively.

Geological evidence in the Campi Flegrei area suggests a very shallow, nearly spherical magma chamber having 1Km of radius and with its top located at 2Km depth beneath the town of Pozzuoli [*Bonafede et al.*, 1986]. Thus, the geometry has been discretised considering a mesh very similar to that shown on figure 6.1.2. On the other hand, drillings and a variety of geophysical investigations have provided information on the properties of rocks underneath the area to a depth of about 4Km [*Berrino et al.*, 1984]. These properties are summarised in table 6.3.1.

Parameter	Value
Lamé parameter λ (a)	7 GPa
Lamé parameter μ (a)	5 GPa
Poisson ratio ν (a)	0.3
Young modulus E (a)	12.9 GPa
Viscosity of the crust η (b)	10^{16} Pa.s
Characteristic time (c)	46 days

Table 6.3.1. Values used in the analysis. (a) Extracted from [*Berrino et al.*, 1984]. (b) Extracted from [*Bonafede et al.*, 1986]. (c) Estimated using equation (4.5.22).

Migration of magma from depth is believed to be the triggering mechanism of the Campi Flegrei inflation[1]. Following [*Bonafede et al.*, 1986] a pressure increase of 5MPa has been assumed here. In the model, this increase of pressure is assumed to be instantaneous and produced in January 1982. The best fit has been obtained considering a rheology with relaxation type 2 (the crust behaves as a Maxwell solid in both normal and deviatoric stresses). The characteristic time of the process has been estimated to be 46 days. Figure 6.3.3 shows the obtained vertical uplift versus distance for different time instants. Finally, table 6.3.2 compiles the differences between measured data and results of the model at the point of maximum uplift (Pozzuoli). These results reflect how, at least qualitatively, a viscoelastic response of the media can account for the 1982-1984 Campi Flegrei ground deformation event.

---

[1] In fact, there is an open debate on whether the source of pressure is an injection of magma or a refilling of the shallow hydrothermal system. However, this distinction is not important for our purposes because both effects produce a similar effect: an increase of pressure at certain depth.

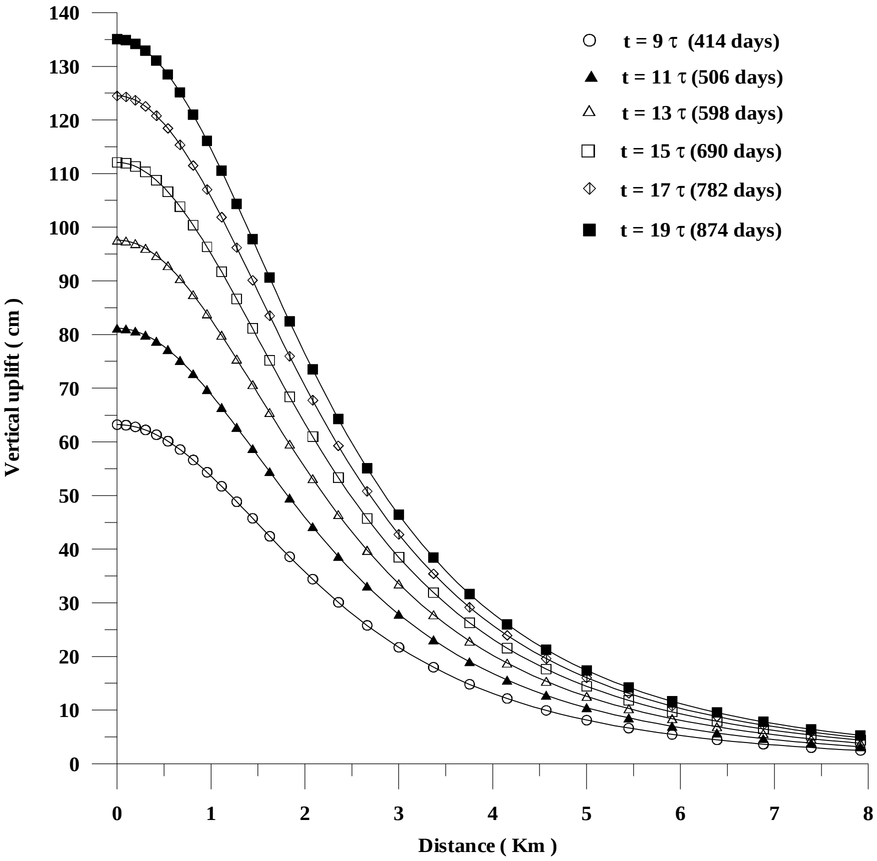

Figure 6.3.3. Numerical results considering a relaxation type 2. Vertical uplift at surface (in cm) versus distance to Pozzuoli (in Km) for different characteristic times τ. Temporal origin (i.e. t=0) is January 1982 and the estimated characteristic time is 46 days. Note how results reasonably agree with the measured data (see figure 6.3.2 for comparison).

Measured data				Model results	
Date	Days after January 82	Time after January 82	Maximum uplift (cm)	Time after t=0	Maximum uplift (cm)
January 83	365	7.9 τ	34.6	8 τ	54.0
June 83	515	11.1 τ	65.4	11 τ	81.1
September 83	605	13.1 τ	89.2	13 τ	97.6
December 83	695	15.1 τ	113.3	15 τ	112.0
March 84	785	17.0 τ	145.8	17 τ	124.5
June 84	875	19.0 τ	163.7	19 τ	135.0

Table 6.3.2. Comparison between measured data and predictions of the model at the surface point of maximum uplift (at *r*=0). Temporal reference is January 1982. The assumed characteristic time is τ=46 days. Measured data are obtained from [*Berrino et al.*, 1984].

6.4 A 3D Application to Tenerife Island

Tenerife is the largest island of the Canary archipelago, where volcanism has occurred over the last 20Ma. The island was originally constructed by fissure eruptions of basic magmas [*Fuster et al.*, 1968; *Ancochea et al.*, 1990] but the posterior development of shallower magma reservoirs led to eruptions of more evolved magmas and brought to the formation of a large central volcanic complex (Las Cañadas edifice). At present, the central part of the island is formed by a shield structure which culminates in a large depression[1], known as *Las Cañadas Caldera*, within which the most recent volcanic activity has built the Teide Pico-Viejo stratovolcanoes [*Martí et al.*, 1994]. The presence of a shallow magmatic system, including phonolitic chambers, is inferred from the products of the most recent eruptions in the Teide Pico-Viejo complex [*Ablay et al.*, 1995; *Ablay et al.*, 1998]. Figure 6.4.1 shows a location map for Tenerife together with some relevant morphological aspects of the island.

Nowadays, the Teide Pico-Viejo volcanic complex is at rest and the only surface manifestations of volcanic activity are fumaroles and thermal anomalies. The geodetic network currently operating in Las Cañadas during the last years has not recorded neither gravity nor deformation changes [*Fernández et al.*, 1999]. The objective of this section is to use the deformation model to estimate which deformation would undergo the island if an hypothetical overpressurisation of the shallow magmatic system beneath Teide would take place. This application may be interesting in terms of volcanic surveillance since can provide insights to improve the present geodetic monitoring system. However, predictions of the model should be considered only as a first approach to the real complex case because many of the parameters involved are approximated in the model by indirect measurements (e.g. chamber shape and depth, crustal rheology, etc.) or simply ignored (batimetry, presence of faults, etc.).

The media is assumed to be viscoelastic and to relax following relaxation type 2 (see section 4.5.2). An important aspect concerns to crustal properties. In the case of Tenerife, [*Bosshard and MacFarlane*, 1970] determined by means of seismic and gravity data that the central part of the island is made up with three layers overlaying the mantle. Following this idea and fitting the increasing amount of more modern data, [*Fernández et al.*, 1999] have recently obtained values for the elastic Lamé parameters and the thickness of the layers. A slight variation of this model, shown in figure 6.4.2, is used here for computations.

---

[1] There is still an open debate concerning the origin of this depression. The most widely accepted theory explains it as a consequence of a collapse caldera which partially destroyed the ancient volcanic edifice. However, some authors support an alternative version according to which the depression was originated by a series of huge landslides.

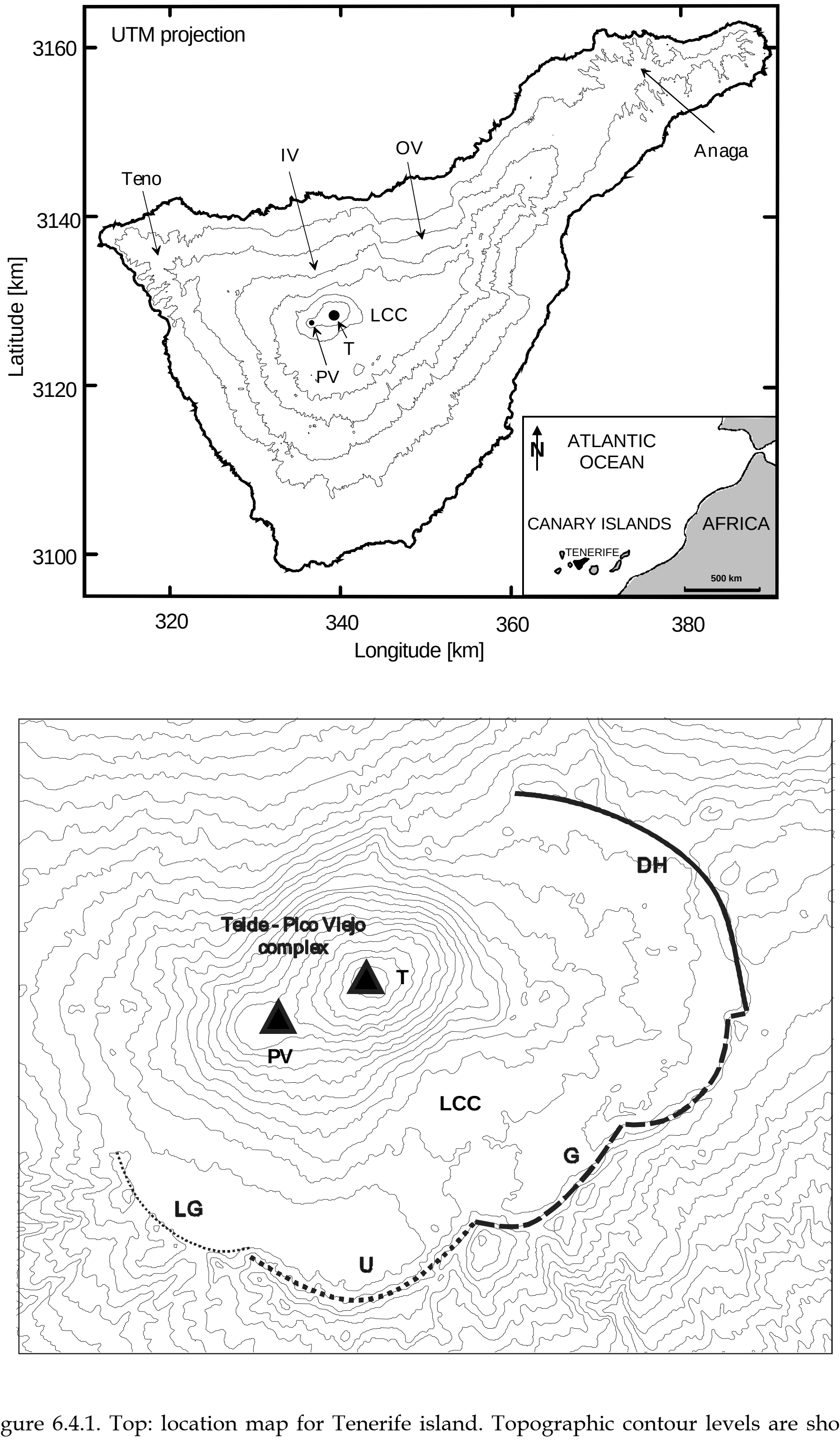

Figure 6.4.1. Top: location map for Tenerife island. Topographic contour levels are shown every 500 m starting from zero and both longitude and latitude are given in UTM coordinates. Bottom: zoom of the central part of the island (Cañadas Caldera). Some morphologic aspects of the island with specific names are also shown using abbreviations: *Icod Valley* (IV), *Orotava Valley* (OV), *Las Cañadas Caldera* (LCC), *Teide* (T) and *Pico-Viejo* (PV) volcanic shields, *Diego Hernández* (DH), *Guajara* (G), *Ucanca* (U) and the *Lower Group* (LG). DH, G, U and LG are different parts of the caldera(s) wall.

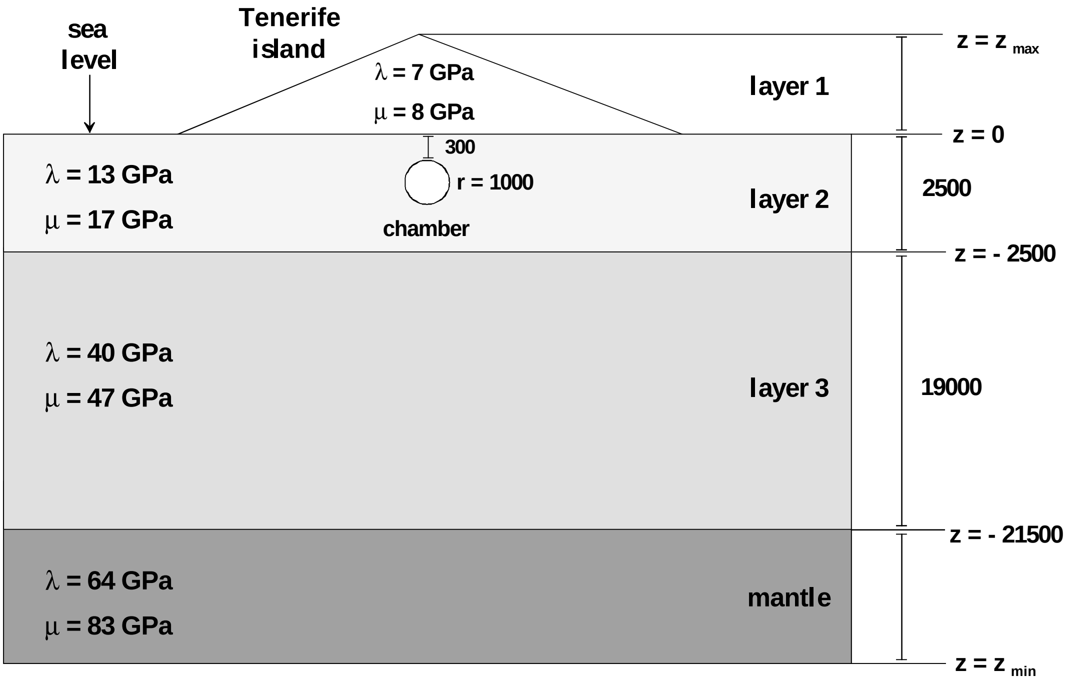

Figure 6.4.2. Schematic illustration (not on scale) of the crustal model used in computations. Four horizontal layers with different elastic Lamé parameters are assumed. The mantle is extended downwards to a distance z_{min}=-30Km, where no deformation is assumed to occur. All the distances are given in m.

The 3D computational domain is a brick with the x and y axis orientated along the WE and SN directions respectively. The z axis runs in the vertical direction (positive upwards) and the origin of coordinates has been placed at the sea level, just below the peak of the Teide. The 1/100.000 scale topography of the island has been added over the uppermost face of the brick. For simplicity, magma chamber is assumed to be a sphere with a radius of 1Km and with its top located at 4Km below the peak of the Teide (i.e. at approximately 300m below the sea level). The shape of the chamber is rather arbitrary, but its depth is deduced from petrological studies [*Wolf*, 1987; *Ablay et al.*, 1998]. Boundary conditions are imposed fixing to zero the displacement field at the bottom and at the lateral boundaries. In order to make negligible the contribution of these boundary conditions to the final solution, computational boundaries have been extended far enough from the pressure source. Thus, the domain has lengths of 70, 60 and 30 Km in the x, y and z directions respectively and almost the whole Tenerife island is covered. Figure 6.4.3 shows the topography of the area selected for computations. The uppermost part of the domain is considered as a free surface[1]. Finally, an overpressure of 10MPa is considered within the magma chamber.

---

[1] In fact, this face includes the island but also part of the sea. Since batimetry is not included, the sea is treated as a solid material. However, this approach is not so bad as could apparently seem since is done only at the most external parts of the domain, far away from the pressure source.

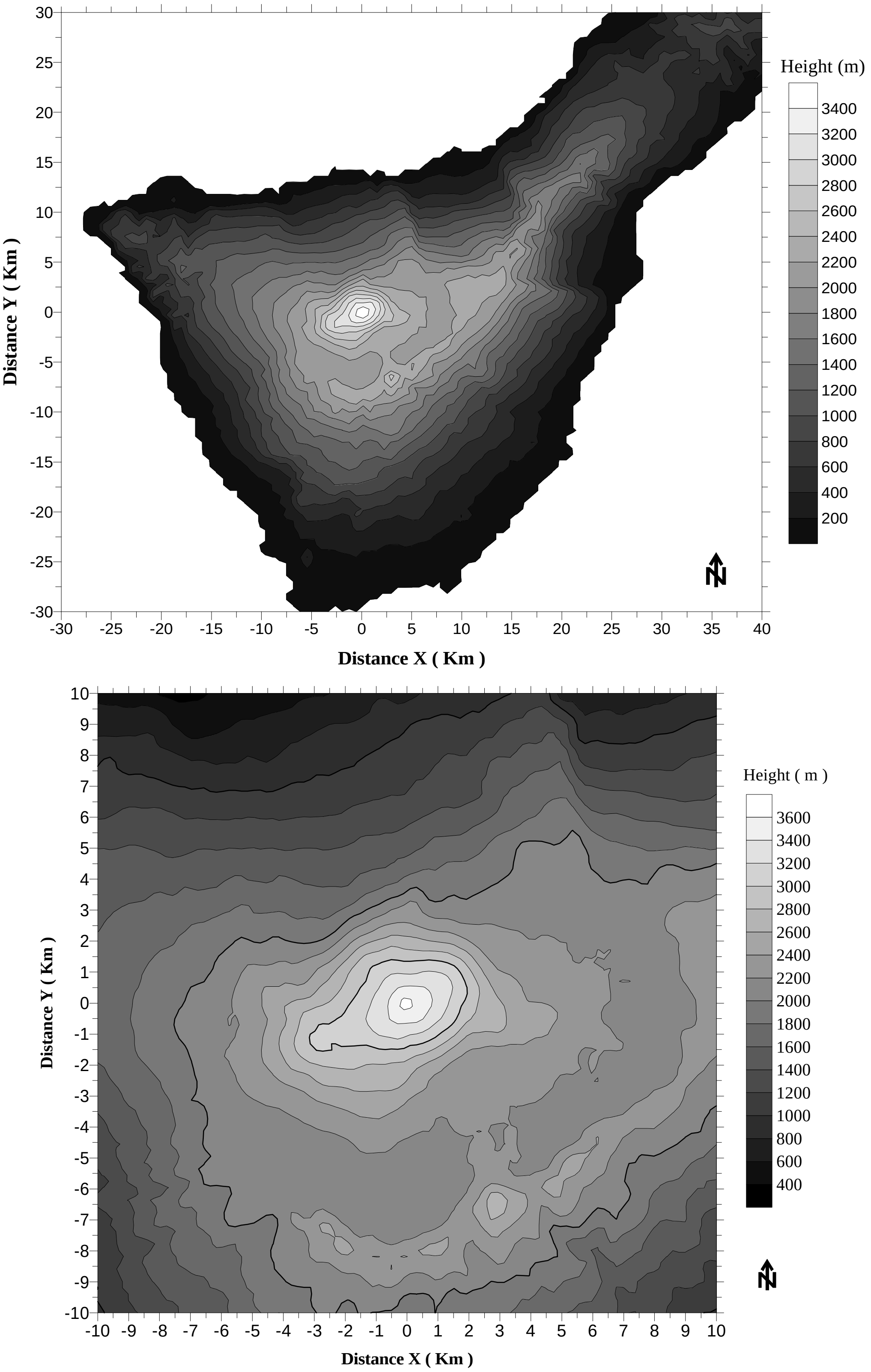

Figure 6.4.3. Top: map showing the topography (height in m) of the area selected for computations. Axis x and y are orientated WE and SN respectively, while axis z (not visible in the figure) runs vertically. The origin of coordinates is located just below the peak of the Teide, at the see level. Computational domain has a length of 70 Km in the x direction and 60 Km in the y direction so that almost the whole island is covered. Bottom: zoom of the topography in Las Cañadas caldera area.

Figures 6.4.4 to 6.4.7 show different views of the mesh. Some morphological features visible in these figures are indicated using the abbreviations defined in figure 6.4.1. This mesh is made up with 99699 tetrahedral elements, is locally refined through the vicinity of the chamber and near the Earth's surface and takes into account the most important morphologic features of the island.

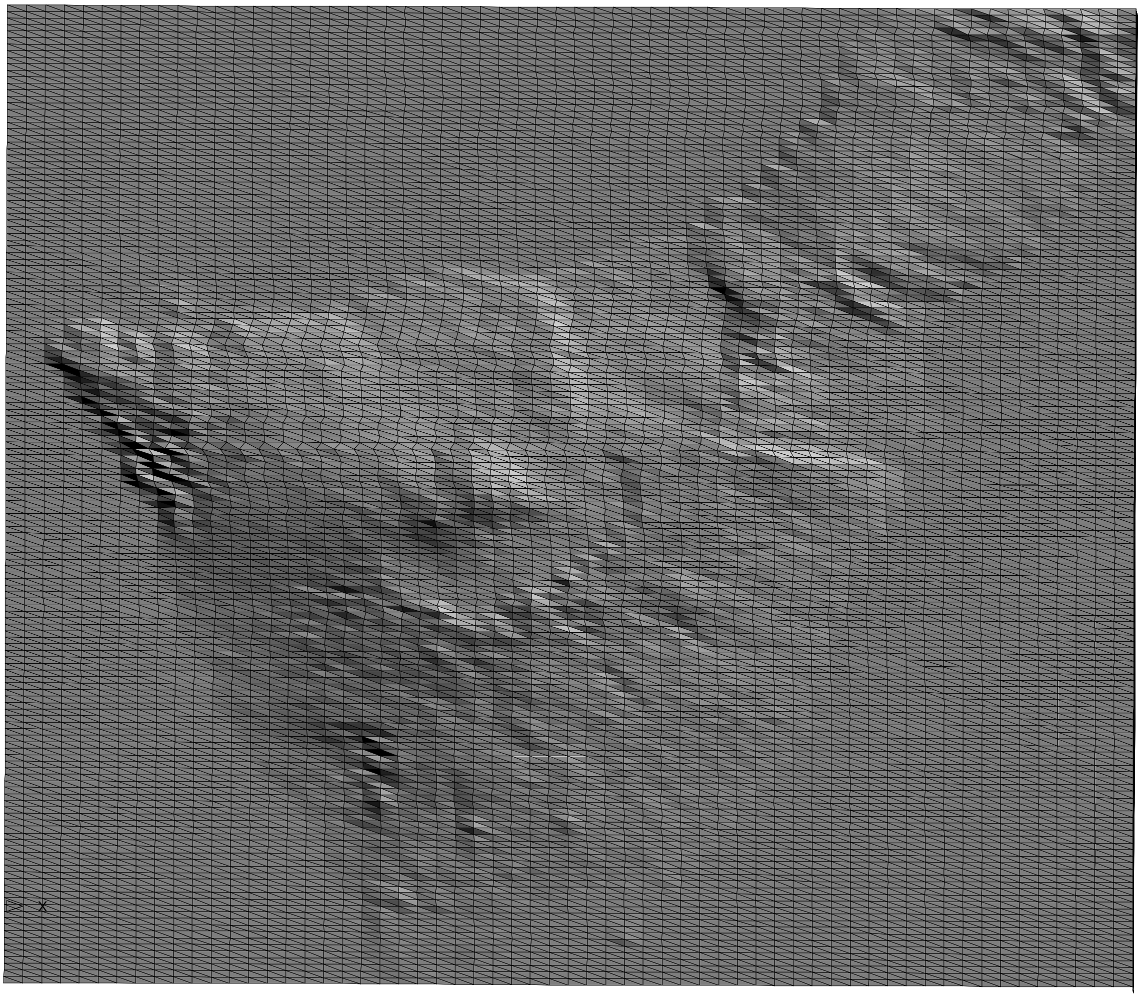

Figure 6.4.4. View of upper face of the mesh.

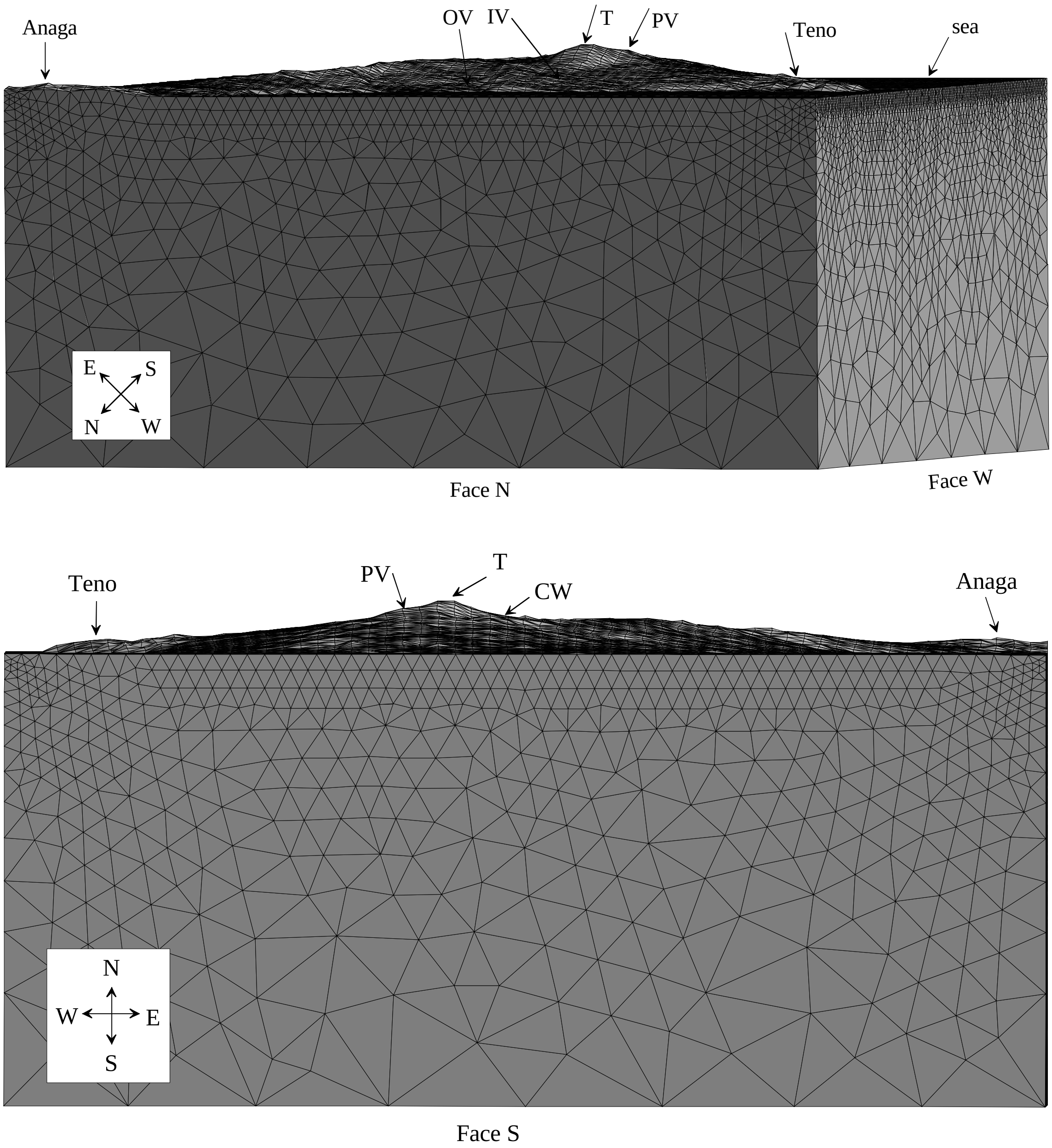

Figure 6.4.5. Lateral views of the mesh. Top: lateral view from the N-NW faces. Bottom: lateral view from the S face.

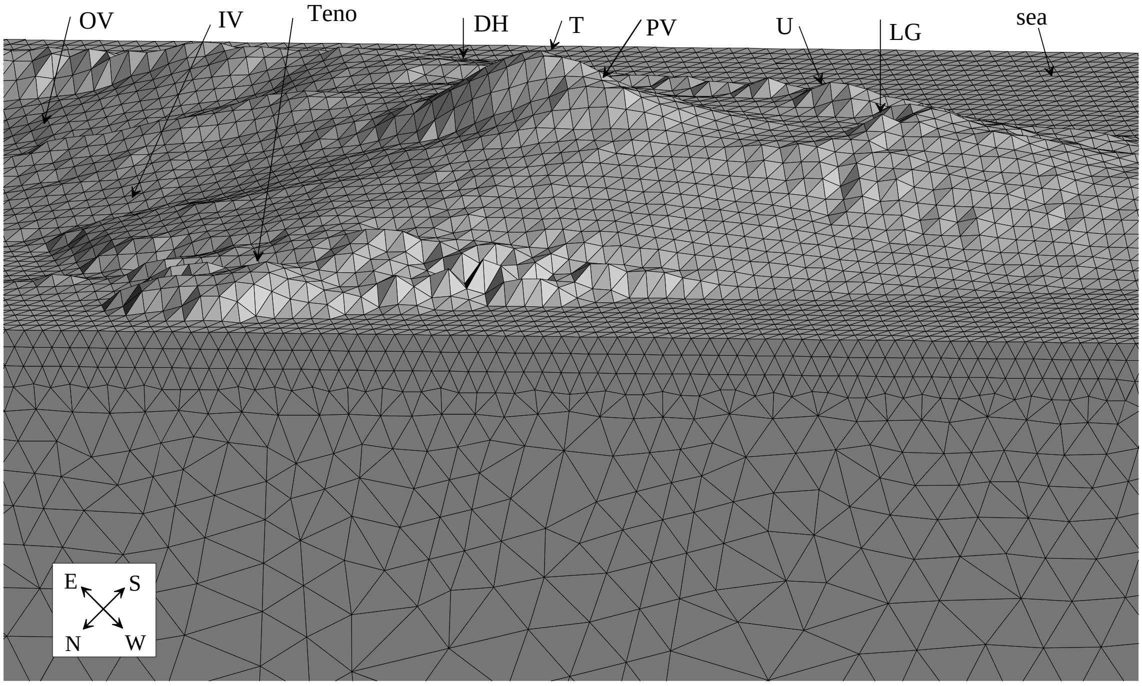

Face W

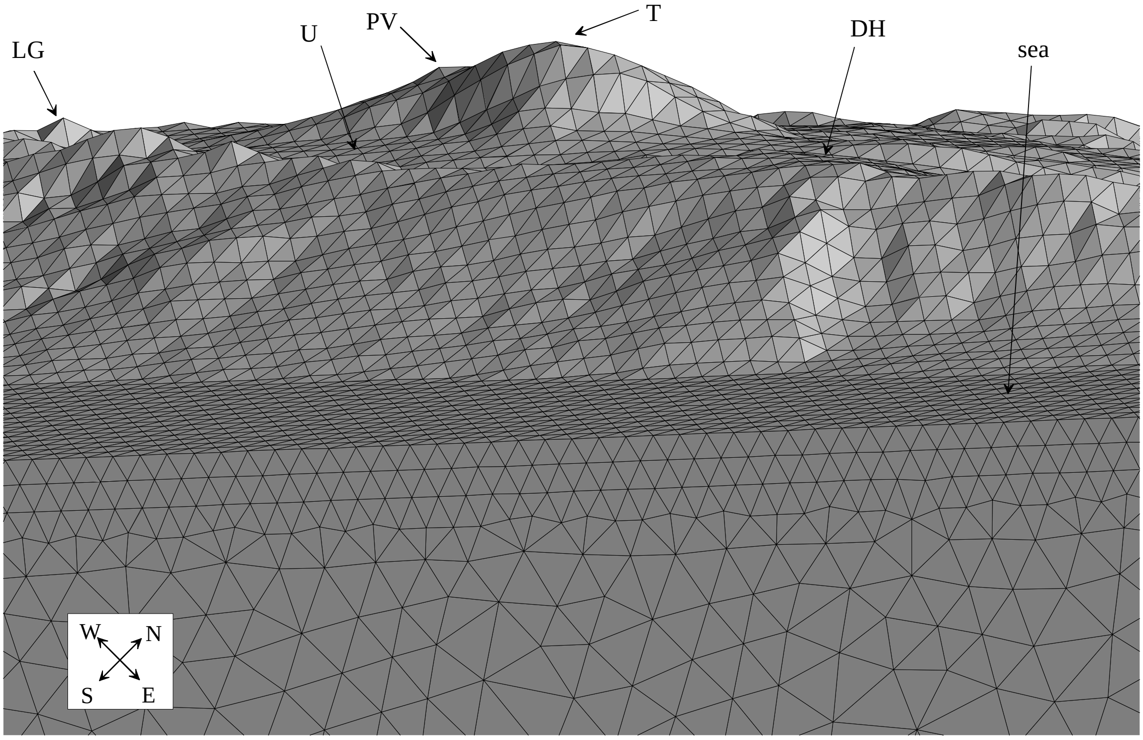

Face E

Figure 6.4.6. Close up views of the mesh around LCC area. Top: View from the W face. Different parts of the caldera wall as well as the Teide Pico-Viejo complex are appreciable. Bottom: View from the E face.

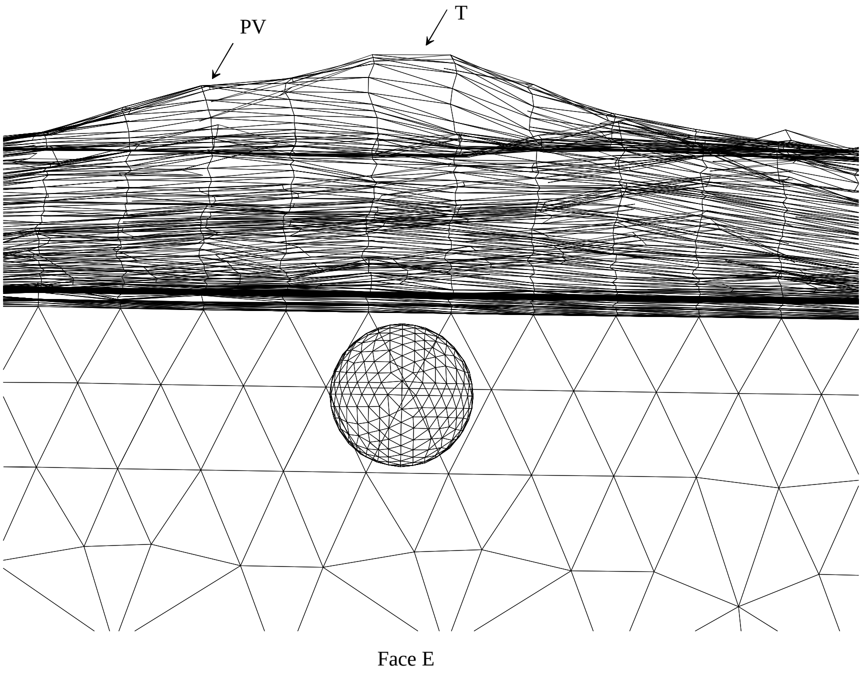

Figure 6.4.7. Close up view of the mesh from the E face around LCC area and without rendering in order to appreciate the magma chamber geometry. Magma chamber is assumed to be spherical (1Km radius) and located 4 Km depth just below the peak of the Teide (i.e. at approximately 300m below the sea level).

The program has been run using a SGI Origin 2000 (8 CPU R10000, 2 GB RAM). The mean required CPU time[1] is about 30-50 min. Part of the results are illustrated in figures 6.4.8 to 6.4.10 which show, respectively, the components of the displacement vector at surface for different characteristic times of $t = 0$, τ , 3τ and 5τ. As observed from these figures, most of the surface deformation is restricted to the vicinity of the Teide (little deformation occurs at distances greater than 5-7Km from the peak of the Teide), that is, the deformation field lies inside the caldera walls. The greater component of the displacement field is vertical (u_z) and has maximum values of about 3.75, 13.75, 21.5 and 34.5 cm for $t = 0$ (elastic displacement), τ, 3τ and 5τ respectively. This vertical deformation pattern is elongated through the NS direction and slightly shifted to the NW of the Teide's peak. In other words, the maximum vertical displacement is predicted to occur (at any time instant) at the NW flank of the volcano. It suggests this part of the volcano as the most suitable place to detect future possible vertical displacements. Another interesting result is the flattening of the vertical displacement field due to topographic effects. This is illustrated in figure 6.4.11.

---

[1] Obviously, this depends on the number of relaxation times considered. These values correspond to the standard case of 6+1 relaxation times, that is, includes the construction and solution of 7 elastic problems using a conjugate gradient solver and the subsequent Laplace inversion at each nodal point.

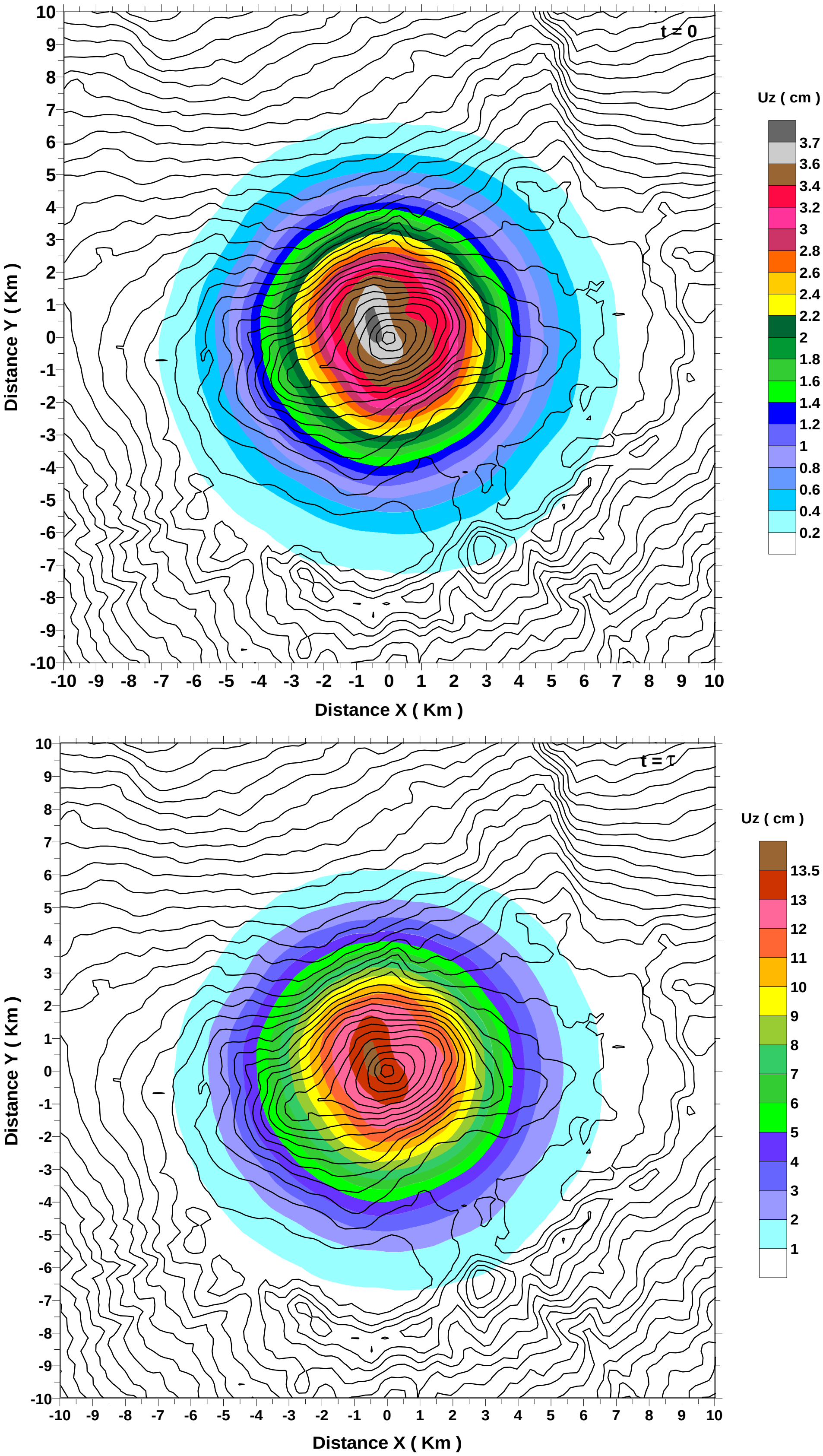

Figure 6.4.8. Vertical displacement u_z (cm) at surface for different time instants: $t = 0$ (elastic), $t = \tau$, $t = 3\tau$ and $t = 5\tau$.

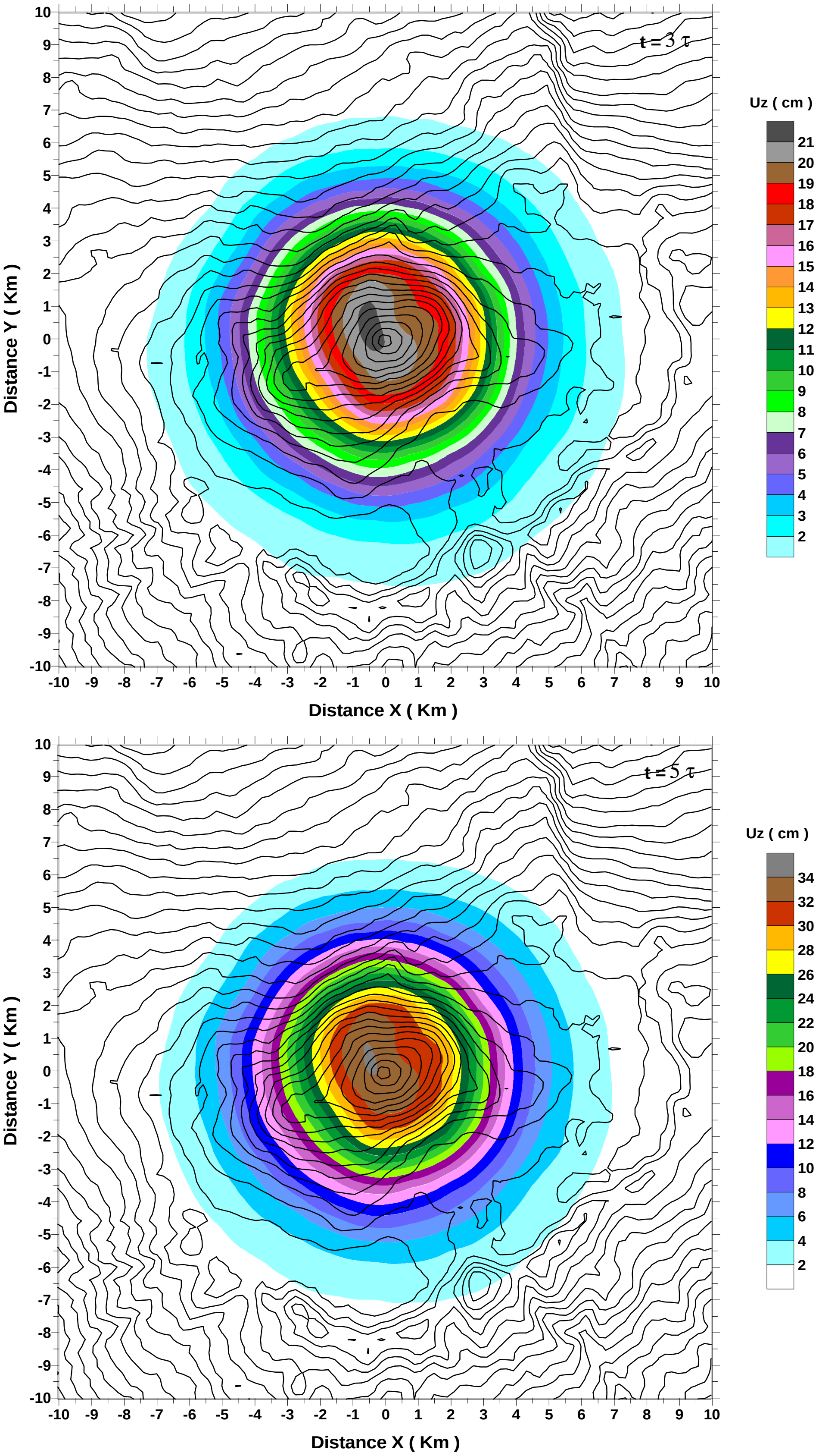

Figure 6.4.8. (cont.).

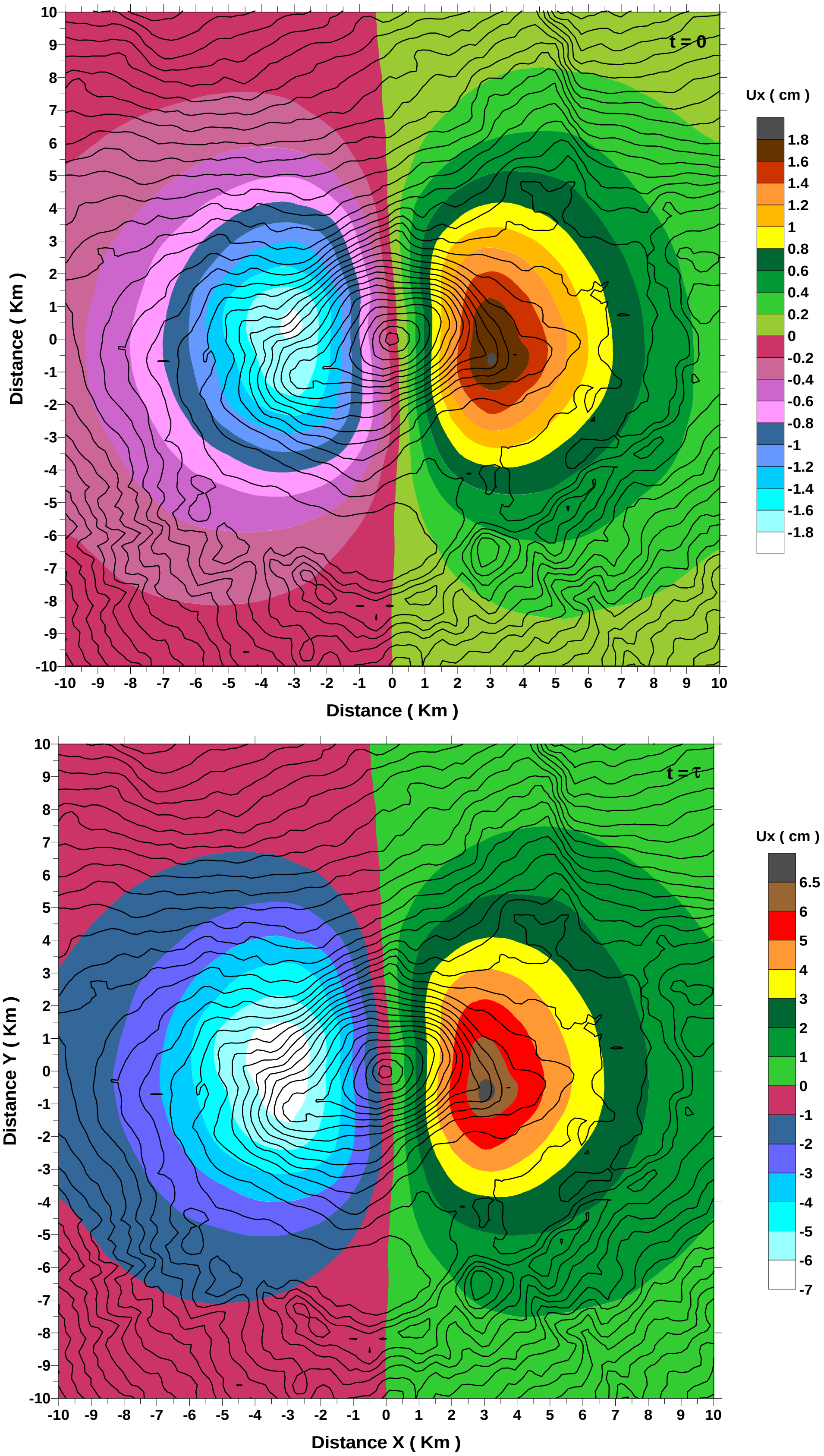

Figure 6.4.9. Horizontal displacement u_x (cm) at surface for different time instants: *t* = 0 (elastic), *t* = τ , *t* = 3τ and *t* = 5τ.

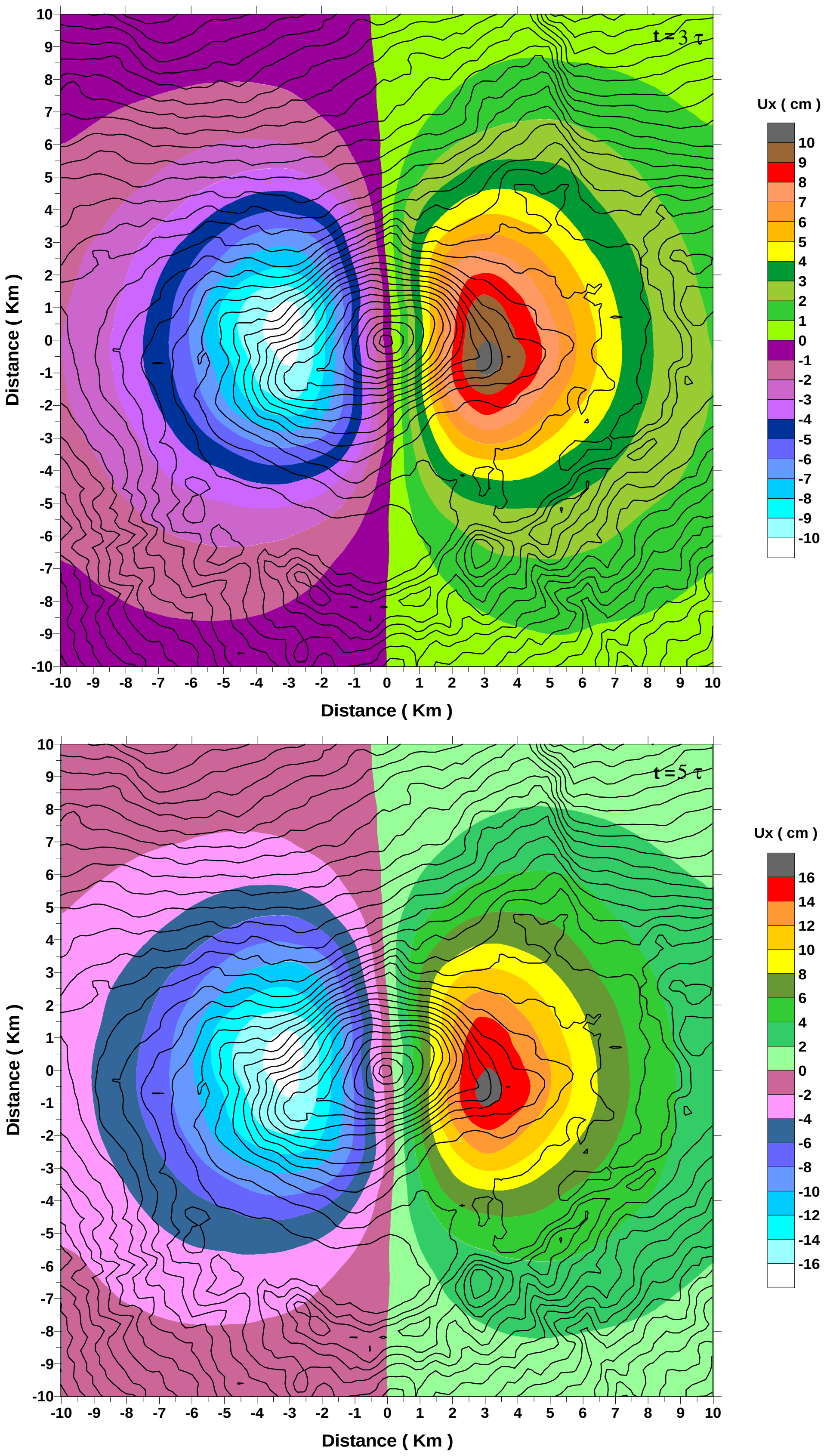

Figure 6.4.9. (cont.).

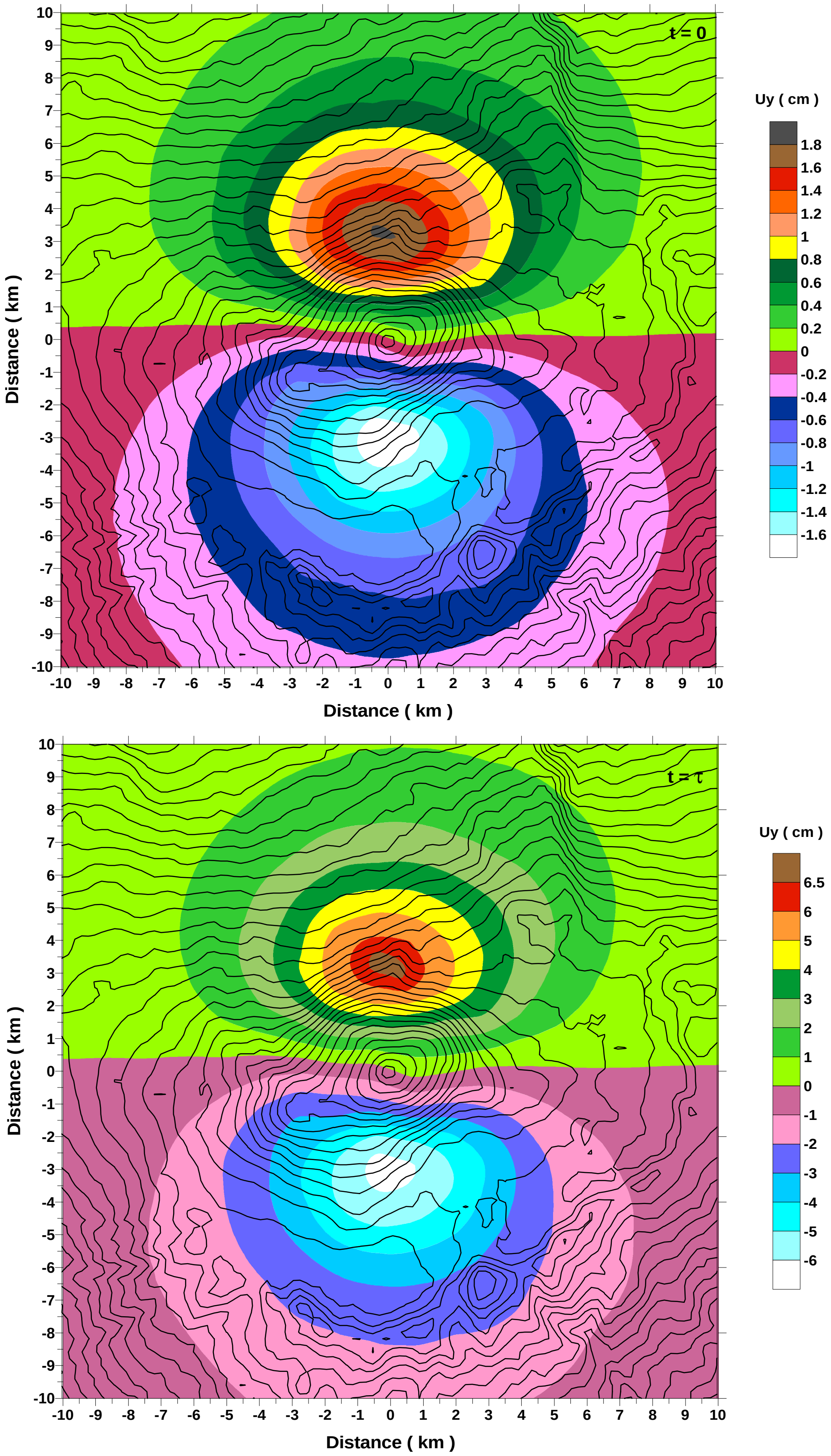

Figure 6.4.10. Horizontal displacement u_y (cm) at surface for different time instants: $t = 0$ (elastic), $t = \tau$, $t = 3\tau$ and $t = 5\tau$.

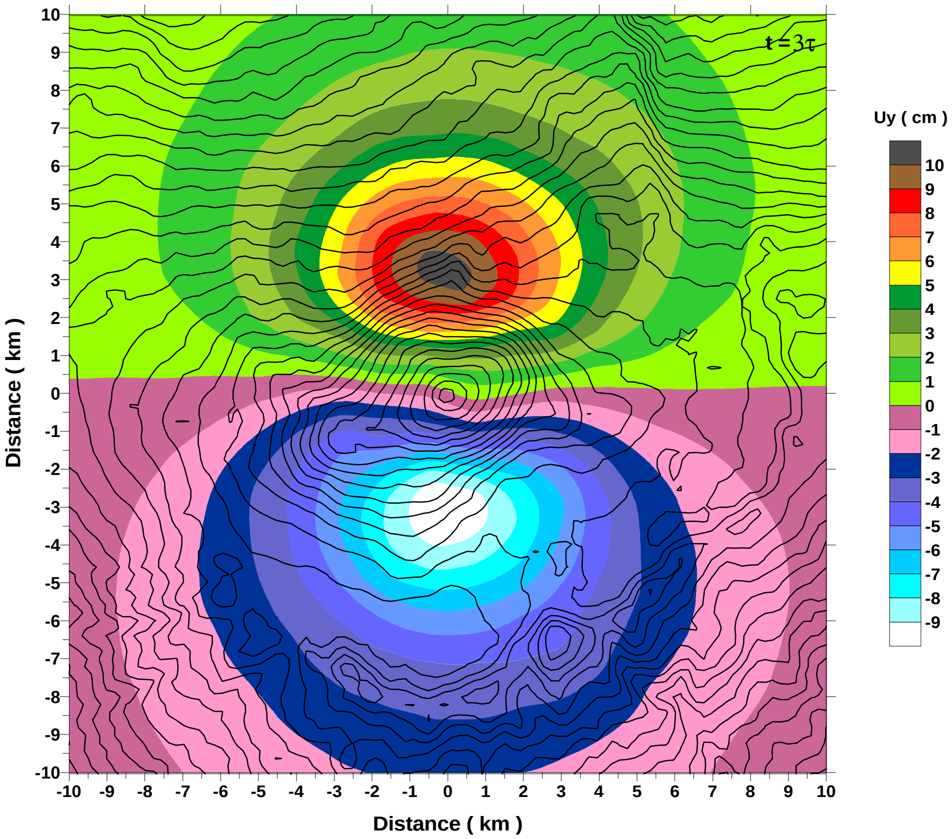

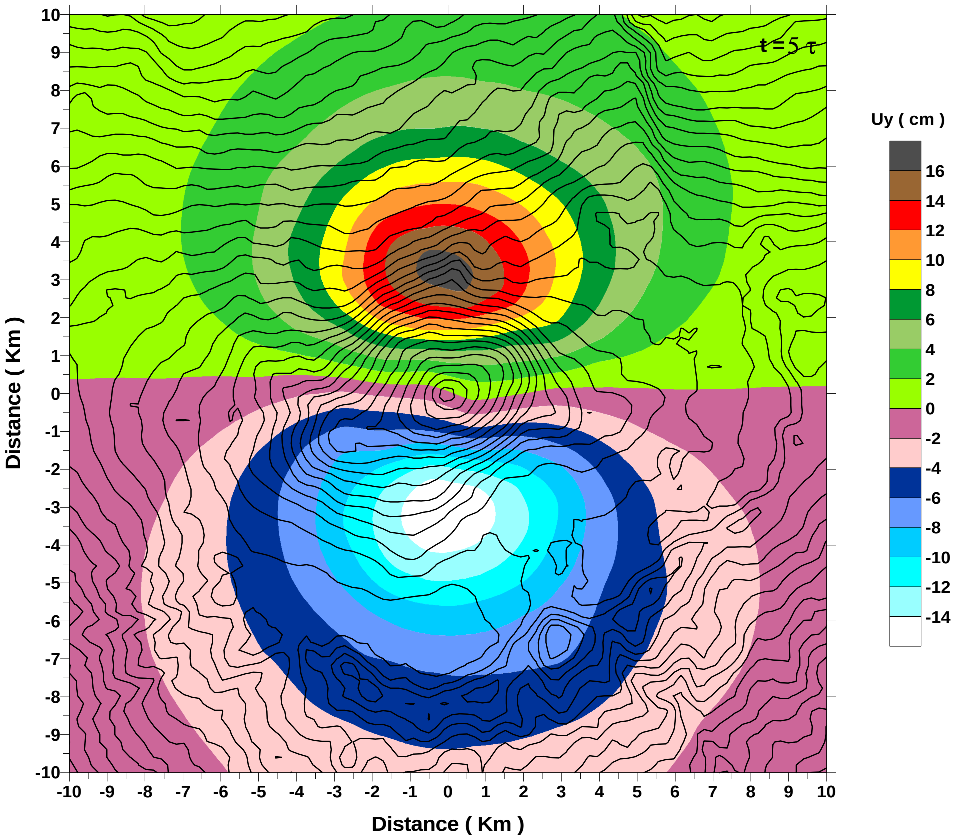

Figure 6.4.10. (cont.).

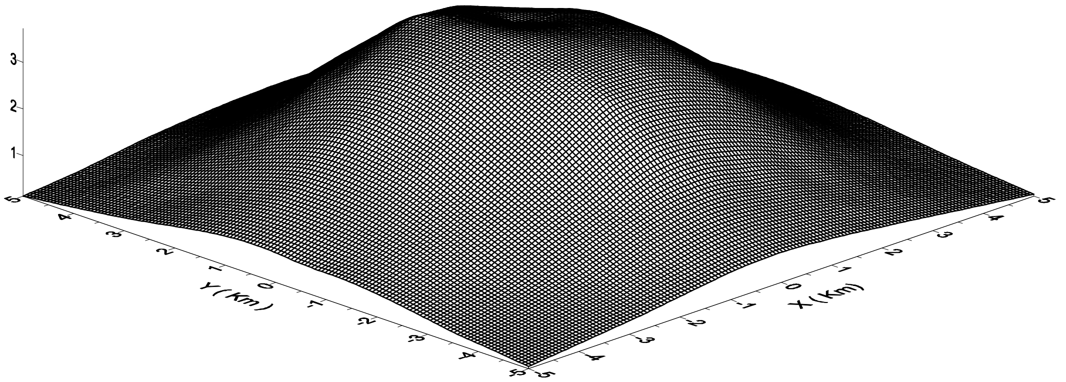

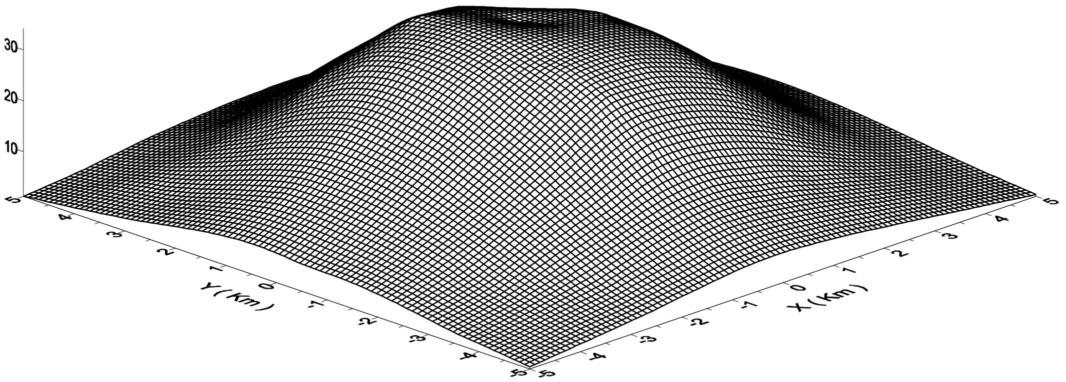

Figure 6.4.11. Tree dimensional representation of the surface vertical displacement (plotted in the vertical axis, in cm). Top: results at *t* = 0. Bottom: results at *t* = 5τ. Note the flattening of the deformation pattern due to topographic effects. Asymmetries of the results are not well appreciated from these figures.

It has been demonstrated previously (see section 6.2.2) how the neglection of topographic effects may, in some cases, induce to considerable errors on elastic/viscoelastic solutions. It means that topography is, generally speaking, a "first order" parameter like, for instance, the depth or the position of the pressure source. Nevertheless, in many cases, topographic effects can also be roughly taken into account by means of 2D models with axial symmetry, i.e. without need of solving 3D problems. Once the 3D case has been solved, one could ask himself *a posteriori* whether the approximate 2D solutions would give comparable results. Clearly, the answer to this question depends on each specific problem. It is also evident that, if one is interested not only in the values of uplift but also on the asymmetries of the deformation patterns, the 3D models must necessarily used. However, what about the qualitative and semi-quantitative results?. To answer this question (at least for this specific case), a 2D axisymmetrical problem with an approximate topography[1] has been also run. In this case, the mesh (not shown) is made up with 26394 triangular elements and 13971 nodal points. The obtained results are reflected in figure 6.4.12. The comparison between this figure and the 3D results (see figures 6.4.8 to 6.4.10) points out how both results are rather similar (relative differences are in the range, or lower than 10%), with the obvious difference that the 2D model predicts axisymmetrical deformation patterns. In consequence, the use of a "real" topography produces only "minor" changes on the solution and can be regarded as a second order effect. For practical applications, it might imply that the errors induced on the solutions due to the uncertainty in the "first order" parameters may well be greater than the minor corrections given by the use of a 3D model.

---

[1] In this case, the island is assumed to be cone with a height equal to that of the Teide and with an average slope of the flanks of 16.5°. The rest of the parameters involved (size of the computational domain, magma chamber, properties and thickness of the crustal layers, etc.) are exactly equal to those of the 3D case.

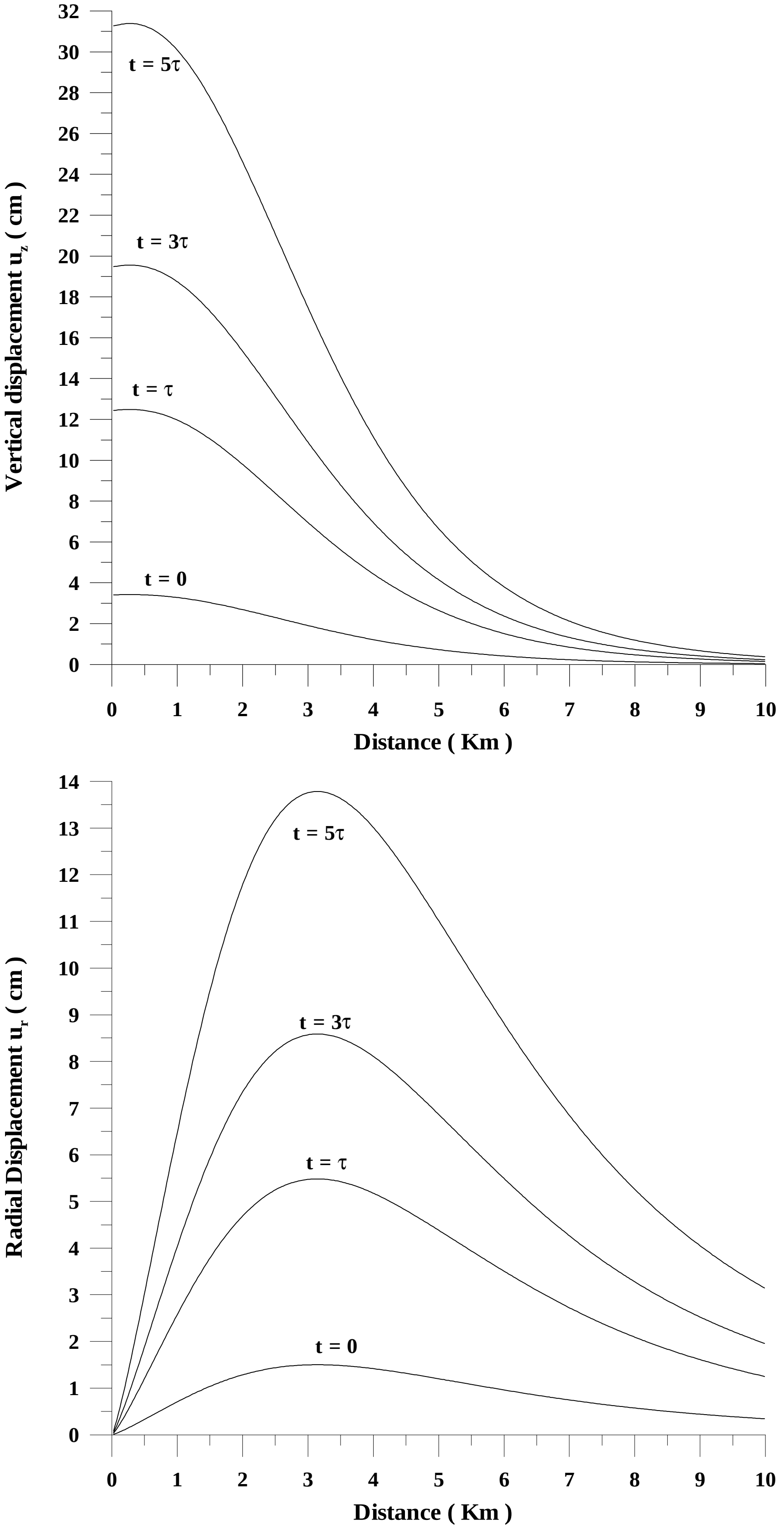

Figure 6.4.12. Results using the 2D axisymmetrical approximation. Top: vertical displacement u_z at surface (in cm) plotted versus radial distance at different time instants. Bottom: the same for radial displacement u_r.

6.5 References

Ablay, G., G. Ernst, J. Martí, and R.S.J. Sparks, The 2ka subplinian eruption of Montaña Blanca, Tenerife, *Bull. Volcanol.*, *57*, 337-355, 1995.

Ablay, G., M. R. Carroll, M. R. Palmer, J. Martí, and R. S. J. Sparks, Basanite-phonolite lineages of the Teide-Pico Viejo volcanic complex, Tenerife, Canary Islands, *J. Petrol.*, 39, 905-936, 1998.

Ancochea, E., J. M. Fuster, E. Ibarrola, A. Cendrero, J. Coello, F. Hernan, J. M. Cantagrel, and C. Jamond, Volcanic evolution of the island of Tenerife (Canary Islands) in the light of new K-Ar data, *J. Volcanol. Geotherm. Res.*, 44, 231-249, 1990.

Berrino, G., G. Corrado, G. Luongo, and B. Toro, Ground deformation and gravity changes accompanying the 1982 Pozzuoli uplift, *Bull. Volcanol.*, 44, 187-200, 1984.

Bonafede, M., M. Dragoni, and M. Quareni, Displacement and stress fields produced by a centre of dilation and by a pressure source in a viscoelastic half-space: application to the study of ground deformation and seismic activity at Campi Flegrei, Italy, *Geophys. J. Royal Astr. Soc.*, *87*, 455-485, 1986.

Bosshard, E., and D. J. MacFarlane, Crustal structure of the western Canary Island from seismic refraction and gravity data, *J. Geophys. Res.*, *75*, 4901-4918, 1970.

Bonafede, M., Axi-symmetric deformation of a thermo-poro-elestic half-space: inflation of a magma chamber, *Geophys. J. Int.*, 103, 289-299, 1990.

Cayol, V., and F. H. Cornet, Effects of topography on the interpretation of the deformation field of prominent volcanoes. Application to Etna, *Geophys. Res. Lett.*, *25*, 1979-1982, 1998.

Dieterich, J. H., and R. W. Decker, Finite element modelling of surface deformation associated with volcanism, *J. Geophys. Res.*, *80*, 4094-4102, 1975.

Fernández, J., and J. B. Rundle, Gravity changes and deformation due to a magmatic intrusion in a two-layered crustal model, *J. Geophys. Res.*, *99*, 2737-2746, 1994.

Fernández, J., J. B. Rundle, R. Granell, and T.-T. Yu, Programs to compute deformation due magma intrusion in a elastic-gravitational layered Earth model, *Computers & Geosciences*, *23*, 231-249, 1997.

Fernández, J., K. Tiampo, J. B. Rundle, T. T. Yu, A. Alonso-Medina, and J. Carrasco, Modelling deformation, potential and gravity changes caused by a magmatic intrusion, *Ann. Geophisicae*, *Supplement I, 16*, 1998.

Fernández, J., J. M. Carrasco, J. B. Rundle, and V. Araña, Geodetic methods for detecting volcanic unrest. A theoretical approach, *Bull. Volcanol.*, *60*, 534-544, 1999.

Folch, A., J. Fernández, J. B. Rundle, and J. Martí, Ground deformation in a viscoelastic medium composed of a layer overlaying a half-space. A comparison between point and extended sources, *Geophys. J. Int.*, *140*, 37-50, 2000.

Fuster, J. M., V. Araña, J. L. Brandle, J. M. Navarro, U. Alonso, and A. Aparicio, Geologia y volcanologia de las Islas Canarias, Tenerife, *Spec. Pub. Instituto Lucas Mallada, CSIC,* 218pp., 1968.

Luongo, G., E. Cubellis, F. Obrizzo, and S. M. Petrazzuoli, The mechanics of the Campi Flegrei resurgent caldera-a model, *J. Volcanol. Geotherm. Res.*, *45*, 161-172, 1991.

Martí, J., J. Mitjavila, and V. Araña, Stratigraphy, structure and geochronology of the Las Cañadas caldera (Tenerife, Canary Islands), *Geol. Mag.*, *6*, 715-727, 1994.

Rundle, J. B., Static elastic-gravitational deformation of a layered half space by point couple sources, *J. Geophys. Res.*, *85*, 5355-5363, 1980.

Rundle, J. B., Deformation, gravity, and potential changes due to volcanic loading of the crust, *J. Geophys. Res.*, *87*, 10729-10744, 1982.

Wolf, J. A., Crystallization of nepheline syenite in a subvolcanic magma chamber system: Tenerife, Canary islands, *Lithos*, *20*, 207-223, 1987.

Chapter 7

Conclusion

7.1 Summary and Conclusions

An algorithm to solve the Navier-Stokes equations considering mechanical coupling has been developed and implemented in the context of a Finite Element Method. Depending on several parameters, the convective term, the viscous term, and the whole energy equation can be discretised in time using implicit/explicit treatments up to second order of accuracy. The algorithm uses a *fractional step method*, that is, computes first the momentum equation without the implicit contribution of the gradient of pressure and adds this subtracted term later, once the continuity equation has been calculated. Depending on a numerical parameter g , the fractional step method can be a *total fractional step method* (the whole gradient of pressure is extracted from the momentum equation) or an *incremental fractional step method* (the explicit contribution of the pressure gradient remains in the momentum equation). The total fractional step method introduces always (at least in the viscous terms) an splitting error of order $O(\Delta t)$ when the implicit versions of the algorithm are considered, whereas the incremental fractional step method allows the possibility of implicit schemes with an error $O(\Delta t^2)$. However, the stability of the pressure field is, in this second case, extremely weak. To correct this drawback (i.e. to have a second order implicit scheme with more stability in the pressure filed) the *pressure gradient projection stabilisation technique* has been introduced. The idea, initially developed in the context of monolithic velocity-pressure formulations, is to add the difference between the Laplacian of pressure and the divergence of the projection of the pressure gradient onto the space of velocities to the continuity equation. It produces the required stabilising effect on the pressure field. The use of a fractional step method introduces a new unknown to the system (the fractional momentum) but, in contrast, allows to use the same interpolation spaces for all the unknowns and deals equally well with both compressible and incompressible flows. This last property is indispensable to simulate the flow dynamics inside magma chambers during the course of some particular volcanic eruptions and, in consequence, fully justifies the choice of this algorithm[1].

The Navier-Stokes equations are considered in the frame of an *Arbitrary Lagrangian-Eulerian* (ALE) formulation which is specially suitable to treat fluid-structure interaction problems. The goal of the ALE description in the treatment of fluids is to keep the advantages of the Eulerian formulation and, simultaneously, to provide accuracy in the description of the

---

[1] The state law proposed for the magmatic mixture presents two differentiated domains because the flow is incompressible when pressure is greater than the exsolution pressure and compressible (a gas-liquid compressible mixture) when pressure is lower than this critical value. This implies that, in those volcanic eruptions in which the magma chamber is partially vesiculated, one must deal with a flow that is incompressible in part of the domain and compressible at the rest of it.

moving boundaries. From a computational point of view, the only difference between the ALE Navier-Stokes equations and its "standard" Eulerian formulation is the introduction of a new convective-like term that accounts for the relative movement between the mesh and the spatial frame of reference[1]. Fluid-structure interaction problems are solved by means of a *staggered procedure* in which the fluid and the structural equations are alternatively integrated in time by using separate solvers. The interaction is taken into account by means of the boundary conditions. The main advantage of such a procedure is that it preserves software modularity and simplicity of the codes. Each time step of the staggered procedure is solved as follows. First, the structural equations are solved using the *constant average acceleration method*, which is the optimal case of a Newmark method[2]. The displacement of the boundary of the structure is then transmitted to the ALE mesh of the fluid imposing continuity of displacements at the fluid-structure interface. It allows to compute the nodal displacements of the ALE dynamic mesh in the whole domain by using the *quasi-Laplacian method*, a variation of the Laplacian smoothing technique that has little element distortion and keeps the quality of the mesh. Second, the ALE mesh velocity is determined. The best choice to minimise the time lag between geometry and nodal variables in the weak forms of the ALE Navier-Stokes equations is to use the second order implicit version of the algorithm and, simultaneously, evaluate the ALE mesh velocity at $t^{n+1/2}$. Note that, in fact, it implies that the weak form is imposed at the same time instant at which the continuous differential equations are verified when the time discretisation is performed[3]. On the other hand, the evaluation of the ALE mesh velocity at $t^{n+1/2}$ combined with the constant average acceleration method guarantees the continuity (at a discrete level) between the velocity of the mesh and that of the structure at the fluid-structure interface. Finally, the ALE Navier-Stokes equations are solved and the forces of the fluid over the structure are computed. An automatic remeshing strategy has been also incorporated to the code. Whenever the ALE mesh becomes unacceptably distortioned, the program automatically generates a new mesh and performs the interpolation of nodal variables onto the new mesh. This interpolation is performed with constrains that impose the conservation of global quantities such as mass, momentum or forces and allows a compromise between the continuity of a variable and the global information it carries.

---

[1] If the problem does not involve fluid-structure interaction this term vanishes and the Eulerian description is recovered.

[2] Only the simplest structural behaviour (rigid solid) is considered in the applications of this thesis. However, due to the staggered procedure, other structural rheologies can be easily incorporated in future applications by introducing minor modifications to the source code.

[3] There are other procedures without time lag between geometry and nodal variables. However, the evaluation of the ALE mesh velocity is, in these cases, more complex and computationally expensive if one wishes to verity the *Geometric Conservation Law*.

The validity of the algorithm as well as its implementation for both fluid and fluid-structure interaction problems has been widely tested in a series of classical benchmark problems. Clearly, an algorithm of such characteristics is interesting by itself because can be used to solve a huge variety of problems arising from several scientific disciplines.

Particular applications are addressed into a better knowledge of one of the problems of physical volcanology that has received less attention: the dynamics of magma withdrawal from crustal reservoirs. A physical model has been proposed. It includes some (necessary) assumptions and a state law for the magmatic mixture under the homogeneous approach (bubbly flow regime). Natural systems are extremely complex and involve many variables which are difficult to measure or that simply are not yet well constrained. It means that the predictions of the model should be taken with caution and should be regarded only as a tool to complement and suggest new possibilities to the traditional geological, geophysical and geochemical approaches. Nevertheless, the important point is that, at least as a first order approach, the combination "physical model developed + algorithm to solve it" allows to simulate "any kind" of volcanic eruption[1]. Different simulations that contemplate a wide spectrum of possibilities have been performed. The quantitative results obtained depend, obviously, on each particular case. Only those qualitative general behaviours for axisymmetrical solutions are stressed here. In fact, some of these results were already predicted by previous time-independent analytical approaches. However, numerical simulations recover all these previous results, allow to envisage new possibilities and, in addition, introduce a new key factor: time dependencies. Relevant general results are:

Eruptions from closed magma chambers

- The initial overpressure decreases exponentially with time until the magmastatic pressure profile is recovered. It produces a drop in the exsolution level (which decreases also exponentially) so that deeper parts of the chamber become progressively oversaturated in volatiles as the eruption proceeds.
- The eruption rate presents a peak of intensity and a posterior exponential decrease.
- The erupted mass fractions in such eruptions are, in general, only a small fraction of the initial mass of the chamber (typically 0.1%-1%).
- Chamber/conduit geometries and volatile content have a major influence on the eruption rate, position of the exsolution level and erupted mass. Being the rest of parameters equal, flattened

---

[1] Volcanic eruptions have been classified in three groups according to its triggering mechanism: eruptions from closed systems (driven by oversaturation of volatiles), eruptions from open systems (driven by injection of fresh, more primitive, magma into the chamber) and, finally, caldera-forming eruptions.

(sill-like) chambers and chambers with greater volatile content erupt more mass because have a greater fraction of oversaturated compressible magma.

Eruptions from open magma chambers

- The initial overpressure descends very rapidly until it becomes stabilised to a steady value (the confining pressure) which depends of the inflow rate. Obviously the position of the exsolution level reflects this fact and also becomes stabilised at a depth which depends on the inflow rate. Once the injection is switched off, the system evolves as in the closed case.
- The eruption rate presents a peak of intensity, an exponential decrease, a plateau and, finally, another exponential decrease once the injection is switched off. This behaviour is, in fact, in good agreement with field observations of many explosive eruptions and might suggest that, as it occurs in the case of primitive magmas, magmatic injection is a common triggering mechanism. However, this suggestion should be taken with caution because this observed behaviour could be also reproduced in closed systems if some effects neglected by the model (chamber deflation, conduit erosion, etc.) were considered.
- Simulations of withdrawal from chemically heterogeneous chambers (with an initial horizontal stratification) suggest that the compositional interface(s) shifts initially upwards until some critical depth is achieved. At this point, the interface tilts and different magmas are erupted simultaneously. From a geochemical point of view, it implies an initial phase in which the evolved (lighter) magma is erupted, a mingling phase and, finally, if the injection is still maintained, a phase in which the injected primitive (denser) magma is extruded. Numerical simulations predict critical depths in good agreement with some previous experimental results and, in addition, point out the possibility of distinguishing between different initial chemical distributions by an accurate sampling of the final volcanic deposits.

Caldera-forming eruptions

- The velocity of the subsiding block increases rapidly to a nearly steady "terminal value" which strongly depends on magma viscosity.
- The eruption rate presents a rapid increase, a plateau phase (corresponding to the steady fall velocity) and, finally a sudden decrease.
- Once initiated, the process of collapse stops when most of the chamber has been destroyed.
- Depending on magma viscosity, a big vortex can be eventually developed at the most external parts of the chambers, below the ring fault. Again, this phenomena is susceptible to generate mingling of magmas initially placed at different depth.
- The exsolution level deepens (shifts downwards) with a velocity similar to that of the subsiding block. However, the exsolution surface is not horizontal at all because the movement of the block causes a lateral gradient of pressure. Most of the exsolution takes place below the

ring fault. It suggests that exsolution of volatiles is an efficient mechanism to sustain such kind of eruptions.

A second objective has been to develop an algorithm which is the "numerical version" of some analytical procedures widely used to compute ground deformations in volcanic areas considering some simple viscoelastic rheologies for the crust[1]. The algorithm has been also implemented in the context of a Finite Element Method and is based on the *correspondence principle* combined with the Laplace transform inversion by means of the *Prony series method*. One of its characteristics is that it is extremely cost-effective because (approximate) viscoelastic solutions can be computed at any time instant with the only computational cost of solving few (normally 7) standard linear elastic problems. Another interesting property is that it generalises the present analytical solutions in the sense that can contemplate a wider spectrum of possibilities such as, for instance, extended sources, topographic effects or any kind of crust's anisotropies. Particular applications and relevant results have been:

- Quantification of the validity of the point source hypothesis by comparing analytical and numerical solutions. In general, for small values of e ($e \leq 0.25$) the differences between the viscoelastic displacements obtained by both procedures are in the millimetric range, for medium values of e ($0.25 \leq e \leq 0.5$) are in the centimetric range and, finally, for large values of e ($e \geq 0.5$) are greater than 30% and can have, in some cases, an absolute value in the metric range.
- Quantification of the topographic effects. It has been found that, for the most common situations (a volcanic shield above the overpressurized chamber), topography is a first order effect. Its neglection can, in many cases, induce an error greater than the one implicit in the source point hypothesis.
- Modelling the 1982-1984 Campi Flegrei uplift. As suggested by previous authors, and despite the simplicity of the model, a viscoelastic response can, at least qualitatively, account for the measured deformation pattern.
- Determination of the effect of a hypothetical pressurisation of the shallow magmatic system beneath Teide volcano. Using a horizontally layered crustal model and assuming relaxation 2, numerical results predict a surface deformation pattern elongated through the NS direction and slightly shifted to the NW of the peak of the Teide. It suggests this part of the volcano as the most suitable place to detect future possible vertical displacements.

---

[1] These rheological models, basically generalisations of the 1D Maxwell solid, have been named relaxation 1, relaxation 2 and relaxation 3.

A summary of the most relevant contributions of this thesis includes:

❶ A numerical procedure to solve the Navier-Stokes equations using a stabilised fractional step method.

❷ The use of the quasi-Laplacian method to compute the ALE mesh displacements (i.e. the ALE mesh velocity) in fluid-structure interaction problems.

❸ The introduction of a conservative interpolation strategy to deal properly the remeshings in fluid-structure interaction problems.

❹ A physical model for the dynamics of magma withdrawal from crustal reservoirs during the course of the most common kinds of (explosive) volcanic eruptions. It includes the development of a state law for the magmatic mixture under the homogeneous approach.

❺ A qualitative characterisation of relevant physical parameters during the course of eruptive events.

❻ A numerical procedure that, using the correspondence principle combined with the Laplace transform inversion by means of the Prony series method, allows to compute viscoelastic displacements in a cost-effective manner.

7.2 Future Lines of Research

Generally speaking and, from a numerical point of view, future lines of research should include mainly the following points:

❶ Improve the implementation of the algorithm introducing parallelism and a better optimisation of the source code. The improving of the efficiency is a question of crucial importance in the case of simulations of volcanic eruptions, specially if one aims to model 3D real cases. In this case, moreover, future lines of research should address the developing of a better temporal integrator for the magmatic state law in order to increase the time step sizes without problems of stability.

❷ Generalisation of the fluid-structure interaction problems that can be solved. It includes the implementation of other different structural rheological behaviours as well as the inclusion of rotational degrees of freedom.

On the other hand, there is no doubt that the fast development of physical volcanology during the last decades has allowed to answer many fundamental questions and has lead to a better global understanding of the volcanic phenomena. However, many important questions still remain open. Its major limitations come not only from the intrinsic complexity and variety of the volcanic phenomena but also from the difficulties of the *in situ* measurements which partially impede the accuracy and refinement of the physical models. Obviously, the feasibility of numerical simulations within this field present serious drawbacks that, in fact, reflect the limitations of the physical knowledge. Nowadays, numerical simulations in volcanology are constrained to simulate specific parts of a global phenomena. In the concrete case of the eruptive process, it is clear that future lines of research should address two main directions:

❸ The consideration of a global volcanic simulation in which the whole volcanic system (chamber, conduit and Earth's surface) is modelled. This juxtaposition of domains is important because the processes that occur in each region affect the dynamics of the others and would overcome the imposition of approximated boundary conditions.

❹ The coupling with the structural behaviour of the host rock. It is also a key issue to determine not only the formation, the propagation and the closure of fractures (i.e. the beginning/ending of an eruption or its possible evolution into a caldera-forming eruption) but also the responses and influences of the environment to the pressure changes during the eruptive process.

Another important question remains, which is the testing of the physical volcanological models or, equivalently, the answer to the following difficult general question: "*how do numerical simulations fit with reality?*". Clearly, their degree of accuracy is strongly dependent on the physical knowledge of the problem and, in consequence, their degree of success is partially conditioned by future development in other scientific disciplines. In particular, some crucial points are a better estimation of the rheologies (for both magmas and crust) and a better knowledge of the pre-eruptive "ambient" conditions (e.g. chamber geometries, characteristics of the environment, properties and composition of the magmas inside the chamber, etc.). In consequence, future lines necessarily imply a parallel advance, an interaction and a mutual benefit among different scientific fields. By now, numerical simulations within this field should be regarded only as a first approach which is, by far, much better than nothing.